UNIVERSITY OF CALIFORNIA
SANTA CRUZ

A TALE OF TWO GALAXIES: STELLAR DISK KINEMATICS AS A FUNCTION OF AGE IN THE ANDROMEDA AND TRIANGULUM GALAXIES

A dissertation submitted in partial satisfaction of the
requirements for the degree of

Doctor of Philosophy

in

ASTRONOMY AND ASTROPHYSICS

by

Amanda C. N. Quirk

June 2022

The Dissertation of Amanda C. N. Quirk is approved:

Puragra Guha Thakurta, Chair

Karoline M. Gilbert

Graeme H. Smith

Kyle B. Westfall

Peter Biehl
Vice Provost and Dean of Graduate Studies

Table of Contents

List of Figures

List of Tables

Abstract

A Tale of Two Galaxies: Stellar Disk Kinematics as a Function of Age in the Andromeda and Triangulum Galaxies

by

Amanda C. N. Quirk

The majority of stars in the universe reside in the stellar disks of galaxies. These disks are fragile but are known to undergo dynamical heating events that increase their scale height and velocity dispersion. Particularly, mergers are a critical part of a galaxy's mass assembly. Thus, understanding how disks are affected by and how they can survive being heated is an important part of understanding how our universe evolves. In this thesis, I study the present day kinematics of disk stars in two nearby spiral galaxies, Andromeda and Triangulum, to comment on their potential dynamical heating history. Studying nearby galaxies allows us to resolve individual stars while making measurements across an entire disk, which gives us a detailed global view of a galaxy's dynamics.

First, I describe a way of calculating asymmetric drift that does not rely on models of a galaxy's potential. I show that asymmetric drift, especially as a function of stellar age, is a tracer of dynamical heating. When compared to simulated galaxy analogs, observed asymmetric drift measurements can be used to constrain a galaxy's merger history. Using this technique, I find that the Andromeda galaxy likely had a major merger in the past 4 Gigayears, which helps shed light on the ongoing debate

about Andromeda's recent merger history.

I then go on to describe the largest stellar spectroscopic survey in the Triangulum galaxy, which is Andromeda's largest satellite galaxy. I discuss initial results from this survey, including a lack of a trend between asymmetric drift/velocity dispersion and stellar age, which is unexpected because of what we see in other nearby galaxies and in our own. I show there are many questions still left to be answered about this galaxy and discuss how answering them will help us understand the pasts and futures of Triangulum and Andromeda.

Acknowledgments

Sappy Stuff

There are many people I feel grateful to have in my life and who have supported me throughout my education. I am sure I will not do everyone justice with the brief text below.

First, I want to thank the friends that I have made here at UC Santa Cruz, who have made these past five years as fun and as stress-free as graduate school can be. I am very grateful for the graduate community at UC Santa Cruz. #protograds2017, I am so happy that this cohort was not competitive and instead took time to help and teach each other. I have no doubt that I would have not passed classes or have settled in as easily as I did without ya'll.

Specifically, Tiffany Hsyu, thank you for teaching me how to be a graduate student. I learned how to navigate the department and how to have a life outside of it from you. Thanks to Evan for always listening and for always being up for an adventure. Kevin, thank you for always being so kind and so supportive. I know I could always rely on you to cheer me on, listen to me complain, and to celebrate whenever one of us needed it. A Bruno, gracias mucho por todo. Ayudó con mucho, cosas faciles y cosas más difíciles, en mi vida y en mi trabajo. Con tú, puedo estar mi misa completamenta. Te quiero para siempre. Erica, we knew we were going to be life-long friends the night I helped you break into your own apartment. You are a ride or die friend. <3 I know that I will never be judged by you. I will always appreciate our spontaneous outings and our chill lazy nights. Thank you for your wisdom, thank you for your friendship, and thank

you for you accepting me exactly how I am. Astro Zack, I feel like you get me. I never have to put on a happy face in front of you and can just be genuine. Thank you for being a true kindred spirit, for always being honest with me, and for being my friend. Thank you for also using your tallness to help decorate and your wild brain to answer my TV questions. Enia, I knew we were going to be close friends from the moment I met you. I remember telling someone from college, "There's this woman named Enia, and I am going to be friends with her." I'm very pleased to say I was right. Thank you for the incredible amount of love, support, and care you've given me over these years. Thank you for encouraging me to take care of myself; you've been a great example of that. It has also been lovely to have had someone willing to drive over the hill just to get noodles. Callie, thank you for being an amazing roommate, and more than that, thank you for being an incredible friend. You so patiently listen to every thought I have throughout a day and graciously validate them all. It has brought me such joy and such peace to have you in my life. You have given me so much reassurance and fun memories over the years. It has been an honor to have built a home with you. While it is sad that I won't be living within walking distance of you all, I know these friendships are for life, so this is not goodbye.

I also need to thank the friendships that are not new. I am so grateful to have friends who have been loving and supporting me since grade school. Caroline and Selin, ya'll are my longest and most beautiful friendships. I really think we are soulmates. Thank you for sticking with me throughout all of these years. I am forever shocked but eternally grateful for the fact that we continued to get closer after high school. It has

been an honor watching ya'll thrive and getting to be a part of it. Thank you for letting me visit and for the effort you've put into staying in touch. I appreciate every message, phone call, and videochat. I love you both and look forward to what we do next and how we continue to be there for each other. Maya, you know I have trouble putting into words how much I love you and how much you have shaped me, for the better, into the person I am today. You were so brave that day you talked to me on the subway, and I don't either of us could have predicted just how drastically our lives would change from that interaction. Thank you, to Maya and to Jenny, for teaching me about boundaries, self love, and healthy relationships. Even though you've been rooting for me to drop out and come back to NYC for the past 5 years, I have appreciated how much you've celebrated my wins and have always made me feel like the best person on Earth. I'm five years delayed, but I am coming back to ya'll finally.

I would also like to thank my family for their support and love. My parents, Anne and Stephen, thank you for letting me focus on grad school and enjoy the downtime with the incredibly generous support you gave me. I grew up wanting to be a scientist because ya'll raised me to never doubt my ability to pursue my dreams. I am grateful for the work and effort you put into making that possible. You both have been incredible examples of how to create thriving careers and how to enjoy them. Thank you for letting me move home at the beginning of the pandemic and for the help you gave me during those surgeries, and the ones that came before. I love you both. Thank you to my Grandmom for introducing me to NYC and for being a fan of me for all of my life journeys. Thank you Gramps and Sharon for your love and support always. I am

excited to once again be just a train ride away. Thank you Trish for all of the happy memories I have growing up with you and for continuing to check in on me. And of course, I have to thank my twin, Zack, for being my best friend when we were kids. You've always supported me, even when I was taking the role of younger sister too seriously or getting all of the attention. It's been so comforting to have taken so many life steps at the same time as you. I love you forever and am excited to see how our life journeys continue.

Raja, I am choosing to put my blurb about you under "Sappy Stuff" instead of "Scientific Acknowledgements" because the support you've given me has gone beyond scientific advice. I truly believe that the best professional decision I have ever made has been to work with you. You have let me choose what to prioritize my entire graduate career, whether it was a certain research project, outreach, teaching, or my physical health. I am so impressed by how easily you create new networks for your outreach initiatives and am grateful that you have connected me to them. For these past five years, I feel like you have been fully invested in me as a person, not just me as a graduate student. Thank you for the time you have given me. (I know how precious your time is.) Thank you, to you and to Mila, for welcoming me into your family. I am so pleased that I get to continue to work with you and am excited for what we continue to create together.

Scientific Acknowledgements

My goal for graduate school was to join a team of friendly people doing cool science. This was mostly inspired by working with Greg Snyder one summer, who

showed me it is possible to do interesting work with kind and supportive people. I feel like I more than accomplished this by choosing to come to UC Santa Cruz and consider my collaborators and many of my colleagues friends. Thank you to everyone for making my graduate school research successful and (mostly) fun. I am so appreciative that Julianne Dalcanton organized a meeting at the Ringberg Castle in 2018, which lead to so many of the collaborations and projects in this thesis.

I would like to give a special shout-out to Bruno Villasenor, without whom, I would be on year 4 out of 7 waiting for my slow code to finish. Thank you, Kevin McKinnon, for patiently teaching me the small amount of statistics I couldn't manage to avoid. I am grateful for Emily Cunningham, who taught me almost everything I know about observing with DEIMOS and for Evan Kirby for being much too kind with all of my questions about data reduction. Karrie Gilbert acted like a coadvisor to me, and I am grateful for all she taught me and the support she gave me. Thank you to Carlos Alvarez, who spent so much time and effort teaching me about Keck during observing runs and who also became a friend. Raja, thank you for being my advisor.

I would lastly like to thank my thesis committee for being infinitely supportive in the decisions I made. I appreciate all of the ideas and advice you have given to me over the years.

Published Material

The text of this dissertation includes reprints of the following previously published material, led by Amanda Quirk, with the permission of the listed coauthors.

Chapter 3 was published in the literature as Quirk et al. (2019). I was re-

sponsible for comparing the previously observed stellar data with published gas data. Thank you to my coauthors Raja Guhathakurta, Laurent Chemin, Claire Dorman, Karrie Gilbert, Anil Seth, Ben Williams, and Julianne Dalcanton for their generous support in helping me learn how to conduct research and communicate science.

Chapter 4 was published in the literature as Quirk & Patel (2020). I led the analysis of the individual simulated analogs. Thank you Ekta Patel for starting this fun collaboration, and thank you for being an amazing role model for the type of collaborator I strive to be.

Chapter 5 was published in the literature as Quirk et al. (2022). For this work, I played a large role in the observations, organization of the survey, and initial stellar kinematics analysis. Thank you to my coauthors Raja GuhaThakurta, Karrie Gilbert, Laurent Chemin, Julianne Dalcanton, Ben Williams, Anil Seth, Ekta Patel, Justin Fung, Pujita Tangirala, and Ibrahim Yusufali for the invaluable feedback that helped make the referee process for this paper so easy.

My work was supported by an NSFGRFP grant DGE-1842400 and an NSF grant AST-1909759, which allowed for several observing trips, in addition to letting me live comfortably as a graduate student. I am grateful for that luxury, as there are too many graduate students who cannot say the same about the compensation they get for their important work.

Land Acknowledgements

The land on which this thesis was written and where I attended class and lived is the unceded territory of the Awaswas-speaking Uypi Tribe. The Amah Mutsun

Tribal Band, comprised of the descendants of indigenous people taken to missions Santa Cruz and San Juan Bautista during Spanish colonization of the Central Coast, is today working hard to restore traditional stewardship practices on these lands and heal from historical trauma.

The majority of stellar data in this thesis, including all of the observations I have done, were taken using a telescope on the summit of Maunakea. Maunakea has always been and remains a sacred sight for the Indigenous Hawaiian community. The manner in which the Keck telescopes were built on the summit harmed the land, the Hawaiian Indigenous community, and the trust the community had with astronomers. I am incredibly fortunate to observe from Maunkea and acknowledge that I have benefited from the harm the telescope has caused.

For my new hips

Chapter 1

Introduction

1.1 Stellar Disks

The majority of stars in the universe are located in stellar disks (Driver et al. 2007). Additionally, the majority of galactic evolutionary processes occur in disks (van der Kruit & Freeman 2011). This makes galactic disks critical sites for understanding how the universe evolved over time. Stellar disks are dominated by ordered differential rotation, resulting in a fairly thin spatial structure. Optical views of stellar disks can be dominated by spiral arms, where the majority of a galaxy's star formation takes place. As a result, stellar disks are some of the most photogenic objects in the universe. Star formation in disks is fueled by large reservoirs of gas, since there is usually a corresponding gas disk of neutral hydrogen. As this thesis focuses on the kinematics of stars in stellar disks, this introduction covers how disks form and evolve, and how these processes affect the movements of stars.

1.2 Stellar Disk Dynamics

The motions of galactic disks are dominated by stars, since gas tends to make up $\sim$ 10% of the mass of a disk like the Milky Way's (Sellwood 2014). Combining the kinematics of individual stars with the spatial distribution of stars gives the overall dynamics of the disk (van der Kruit & Freeman 2011). The orbits of most stars can be described by the epicyclic approximation in a smooth axisymmetric potential. While the largest component of a star's velocity is in the azimuthal direction, stars do oscillate above and below the disk mid-plane and also migrate in the radial direction (Sellwood 2014). Orbital velocities can be described by three components: azimuthal (φ), radial (R), and vertical (Z), and a population of orbits can be described using these components as inputs to a velocity ellipsoid (Equation 1.1) and Jean's equation (Equation 1.2, Binney & Tremaine 2008). The velocity ellipsoid (Equation 1.1) depends on the inclination (i) and position angle (φ) of the stars and the various components of the velocity dispersion (σ). Jean's approximation (Equation 1.2) is dependent on some modeling of the galactic potential so requires the circular velocity of the disk (v_c) and the difference between a star's orbital velocity and that circular velocity (v_a). It also relies on the galactic radius (R), the disk scale length (R_d). In the equation, k is either 1 or 2 on depending if σ_R is constant or declining, respectively.

$$\sigma_{\mathrm{LOS}} = ((\sigma_R^2 \sin\varphi^2) + \sigma_\varphi^2 \cos\varphi^2) \sin i^2 + (\sigma_z \cos i)^2)^{1/2} \tag{1.1}$$

$$v_a^2 - 2v_c v_a = -\sigma_R^2 \left[\frac{\sigma_\varphi^2}{\sigma_R^2} - 1.5 + \frac{kR}{R_d} + \frac{\sigma_Z^2}{2\sigma_R^2} \right] \tag{1.2}$$

Studying the ratio of the components of the velocity ellipsoid (or the anisotropy) can help determine the origin of a population of stars (Cunningham et al. 2019b). The present-day kinematics of stars, and the overall dynamics of the stellar disk, are influenced both by birth conditions and by heating. In Section 1.3, I discuss what can set the birth kinematics of a stellar disk, and in Section 1.4 and 1.5, I discuss the ways disks can be permanently changed by dynamical heating.

1.3 Stellar Disk Formation

Most disks form around $z \sim 2.5$ (van der Kruit & Freeman 2011). While it is not always clear in a given galaxy if the stellar disk has a distinct thick and thin part (Bovy et al. 2012), it is known that galaxies can have separate thin and thick disks and that thick disks are common (Yoachim & Dalcanton 2008). Sometimes these disks are distinct with different populations, and other times, there is a more gradual change between the properties of the disk components. In extreme cases, thick disks have been seen to counter-rotate compared to the thin disk (Yoachim & Dalcanton 2008). Either way, these disks must form, and there are several leading theories of mechanisms for how it happens.

First, disks can form from thin or thick gas clouds, resulting in a present-day thin and/or thick disk, respectively. This theory emphasizes the importance of birth

conditions over heating or relaxation conditions (Brook et al. 2004).

In another scenario, an initially thick gas cloud with clumps can continue to collapse over time, leading to an older thick disk and a younger thin disk (Bournaud et al. 2009; Bird et al. 2013, 2021). In this sense, disks form "upside down" and "inside out" (Bird et al. 2013). This results in thick disks containing older and more metal poor, but more alpha-enhanced, stars, with the thin disks consisting of younger and more metal rich stars (Fuhrmann 2004; Chiba & Beers 2000).

Alternatively, an initially thin disk can be heated over time to create a present-day thick disk (e.g. Quinn et al. 1993; Velazquez & White 1999; Purcell et al. 2010; Tissera et al. 2013; Abadi et al. 2003; Ida et al. 1993; Maxwell et al. 2012). This process can be slow or fast, depending on the heating mechanism, and can result in a distinct thin and thick disk, where the thin disk is dominated by rotation and the thick disk has some random motion. Alternatively, it can result in a disk that has less clearly distinct components. I discuss possible ways this phenomenon can occur in the next section.

1.4 Stellar Disk Evolution

Stellar disks can experience dynamical heating throughout their formation and evolution. Stellar disks are fragile (but perhaps this thesis suggests otherwise), and stars are collisionless (Toth & Ostriker 1992), so the effects of heating are long-lasting and significant. In this section, I discuss three different kinds of heating a stellar disk can experience.

1.4.1 Secular Internal Heating

Secular evolution consists of slow changes from long-term interactions between a stellar disk and a perturber. As galaxies evolve, they are able to reach a lower energy state by redistributing angular momentum outwards (Sellwood 2014). Angular momentum can be transported to the disk through the density waves of spiral arms and through a galactic bar (Saha & Elmegreen 2018), as the pattern speed of the bar slows due to dynamical friction (Binney & Tremaine 2008; Sellwood & Binney 2002). Secular evolution can change an individual star's or gas cloud's angular momentum without changing the population's distribution of angular momentum and therefore does not always increase random motions (Binney & Tremaine 2008). However, scattering via giant molecular clouds (GMCs) can increase vertical random motions, while scattering via spiral arms increases random motions in the plane of the disk (Ting & Rix 2019). It is believed that spiral arms are the most impactful source of a galaxy's evolution (Sellwood 2014).

1.4.2 Non-Secular Internal Heating

Stellar disks are also affected by violent, short-term processes, like some forms of heating from GMCs (Ting & Rix 2019), star formation (El-Badry et al. 2016), and feedback from supernovae (El-Badry et al. 2016) and active galactic nuclei (Dashyan et al. 2019). These processes are especially important for low mass galaxies with shallower potentials (El-Badry et al. 2016). Violent bursts can both trigger star formation and quench galaxies, as they deposit energy to the gas clouds around them, causing

them to collapse or to be stripped (El-Badry et al. 2016). The dominant star formation mode in low mass galaxies is a series of bursts (Oñorbe et al. 2015; Guo et al. 2016), leading to gas outflows and inflows driven by stellar feedback. Stars form in the this gas, inheriting its motions. The outflowing and infalling gas also drives fluctuations in the global potential, resulting in a transfer of energy to stars (El-Badry et al. 2016). The resulting effect is more energetic stellar orbits and outward radial migration (Stinson et al. 2009; Maxwell et al. 2012; El-Badry et al. 2016).

1.4.3 External Heating

Galactic disks are also affected by galaxy mergers and flybys. While they have a bigger impact on a galaxy's halo, the disk is not immune to the effects of a merger. These mergers can completely tear apart smaller galaxies, leaving tidal streams in the halo, and sometimes depositing stars in a galaxy's disk (Ida et al. 1993). Merging satellites can also trigger star formation or quench a galaxy (e.g., Martig et al. 2009; Gabor et al. 2010; Pontzen et al. 2016). Galaxy mergers are critical for the mass assembly of galaxies and integral to the theory of ΛCDM. While it had previously been believed that disk galaxies could not survive recent major mergers (Toth & Ostriker 1992), new simulated and observational evidence suggest that massive disks can in fact survive mergers with a low mass ratio (Hammer et al. 2018; D'Souza & Bell 2018). Low mass disk galaxies are less likely to survive with their disks intact and are more susceptible to being gravitationally perturbed by flybys and near galaxy interactions. As galaxies become more isolated from past mergers and with the expanding universe, external heating is no longer the dominant driver of galaxy evolution (Binney & Tremaine 2008).

1.5 Effects of Stellar Disk Heating

Stellar disks are fragile so can be permanently altered by heating processes (Westfall et al. 2014; Kregel & van der Kruit 2005). Secular evolution can create pseudobulges (Binney & Tremaine 2008; Yu et al. 2022) and can pull stars off their orbits in a process called radial migration (Daniel & Wyse 2015; Daniel et al. 2019). Additionally, disk heating can lead to a puffed out or kicked up disk, in which the disk stellar kinematics more resemble that of a halo component than a dynamically cold disk (Dorman et al. 2012, 2013). They can also increase stellar velocity dispersion in the disk (Leaman et al. 2017). Because stars are collisional, they retain the effects of heating over long timescales.

Each of the processes described in the previous sections leaves unique signatures in the distribution of metallicities and velocities of a stellar disk. For example, we find velocity dispersion to increase with stellar age (Dorman et al. 2015), as older stars tend to have experienced more heating than younger stars. When stellar velocity and metallicity are combined, we can trace the likely origin of a population of stars, i.e., were the stars born in-situ or ex-situ of where they are observed present day (Cunningham et al. 2019a,b).

1.6 The Power of Resolved Stellar Spectroscopy

In order to perform these types of studies to determine the origin of a stellar population, we need spectroscopy of individually resolved stars. Without measurements of individual stars, we cannot definitively study trends as function of stellar age, which

is critical for disentangling present day kinematics and birth kinematics. This information is especially powerful when paired with gas kinematics, as it allows us to make local measurements across a disk without relying on models of a galaxy's potential. These present day observables can provide the tools to understand the kinematical and chemical evolution of a galactic disk. This becomes especially important for interpreting unresolved spectroscopy for higher redshift galaxies, where it is not possible to resolve individual stars.

1.7 The Local Group

Taking resolved spectroscopy of individually resolved stars is only possible in the Local Group (LG). The LG consists of ~ 30 galaxies, with the Milky Way (MW) and the Andromeda galaxy (M31) being the most massive members. Within our own MW galaxy, we are confined to spectroscopy of the Local Solar Neighborhood. This limits surveys of galaxy dynamics to a small portion of the disk. *Gaia* continues to expand the view of our galaxy (e.g., Antoja et al. 2018), but it is still limited in the radial velocities available. More will come with DR3. Close MW satellites, like the Large and Small Magellanic Clouds (LMC and SMC, respectively), take up a large angular portion of the sky, so they require significant telescope time to get spectroscopy across their entire disks.

Thus, arguably the best targets for resolved stellar spectroscopy are M31 and its smaller neighbor, the Triangulum galaxy (M33). M31 is a nearly edge-on spiral galaxy with a virial mass of $M_{\rm vir} \approx 10^{12}\ M_{\odot}$ and is at a distance of 785 Mpc (Mc-

Connachie et al. 2005). It has a classical bulge, a thin bar extending to 4 kpc, and a kicked up disk (Dorman et al. 2012, 2013). M31 is a green valley galaxy, as it is in between a star forming and quenched galaxy (Mutch et al. 2011). There is a ring of star formation across the disk at $r \sim 10$kpc (Lewis et al. 2015). The outskirts of M31 show remnants of mergers, suggesting it has had frequent and ongoing mergers throughout its history (Ibata et al. 2013). The remnants in M31's halo can be explained by a series of minor mergers (Fardal et al. 2007; Ibata et al. 2001; Hernquist & Quinn 1988, 1989; Tanaka et al. 2009) or by a more recent major merger (Hammer et al. 2018; D'Souza & Bell 2018). Whatever the exact merger scenario, it is evident that M31 has had many mergers in its lifetime (McConnachie et al. 2018; Mackey et al. 2019; Escala et al. 2019). Similar evidence for a violent merger history is not seen in the MW despite its disk being a similar mass to M31 (Belokurov et al. 2006; Ferguson & Mackey 2016).

M33 is a satellite galaxy of M31, with a significantly lower stellar mass of $M_* \approx 2.9 \times 10^9$ (McConnachie et al. 2009) and is currently ~ 230 kpc away from M31. While most dwarf galaxies are believed to be dominated by a single component, M33, is proving to be quite complex, with a newly discovered centrally located halo (Gilbert et al. 2022) and bar (Williams et al. 2021) and warps in the extended neutral Hydrogen and stellar disk (Putman et al. 2009; McConnachie et al. 2009; Braun & Thilker 2004). It is one of the only dwarf spiral galaxies in the LG and has maintained its spiral structure more than the LMC. Unlike M31, M33 has a pseudobulge and is a nearly face-on galaxy. It is actively forming stars at a high rate (>10× Andromeda's SFR, Blitz & Rosolowsky 2006), making it resemble later-type spiral galaxies. It is assumed M33 has had many

minor mergers in the far past (Helmi et al. 2012). Despite its relatively pristine spiral structure, there are large S-shaped warps in the stellar and gas disks. These warps are indications of the disk being disturbed in some way, but their cause is unknown.

The interaction history of M33 and M31 is also unknown. Figure 1.1 shows the angular separation of M31 and M33. A close interaction between M31 and M33 could explain the extended gas and stellar structures in M33 and a burst of star formation $\sim 2-4$ Gyr ago in both M31 and M33 (e.g. Putman et al. 2009; McConnachie et al. 2009; McConnachie et al. 2010; Lewis et al. 2013; Ferguson & Mackey 2016; Semczuk et al. 2018). However, modelling using proper motions of M31 suggest M33 is on its first infall (Patel et al. 2017; Patel et al. 2017; van der Marel et al. 2019). If M33 evolved in isolation and is on its first infall, a close interaction(s) with a member(s) of M33's satellite population could have induced the stellar and gas disturbances observed in the outskirts of M33's disk (Patel et al. 2018). Despite its proximity, M33's stellar populations have been relatively under-studied. Thus, there is still much be learn about M31 and M33.

Figure 1.1: Image of M31 and M33 taken from California by Yifei Luo.

1.8 This Thesis

The goal of this thesis is to utilize resolved stellar spectroscopy coupled with photometry and gas spectroscopy to reveal the present day stellar kinematics and the dynamical heating history of M31 and M33. These galaxies give us an external and global view of spiral galaxies like our own MW, so studying them can give us insight into our own galactic home. I use cosmological simulations and past kinematic studies of LG members to contextualize my results.

This thesis is organized as follows: Chapter 3 compares the stellar disk kinematics of M31 to the kinematics of surrounding gas. Chapter 4 compares these observational results to the kinematics of simulated analogs in a large-scale cosmological simulation. Chapter 5 presents the largest stellar spectroscopic survey of M33 and initial results of the survey. It also compares the stellar kinematics of the three most massive members of the LG. Chapter 6 presents a summary of this thesis and avenues for future work.

Chapter 2

Example Stellar Spectroscopy

In this chapter, I show example stellar spectra from the SPLASH (M31) and TREX (M33) survey. Each plot shows a stellar type: main sequence (MS), asymptotic giant branch (AGB), red giant branch (RGB), red helium burning (RHeB), blue helium burning (BHeB), weak CN, and carbon stars. The telluric features at 7600 and 6900 Å have been removed in all of the below spectra, but the chip gap has not been removed. There of course is variation in the spectral features, signal to noise, and wavelength coverage across the full range of spectra, which is not represented in these examples. All of the below spectra were taken with DEIMOS. The details of each survey and their respective observation plans can be found in chapters 3 and 5.

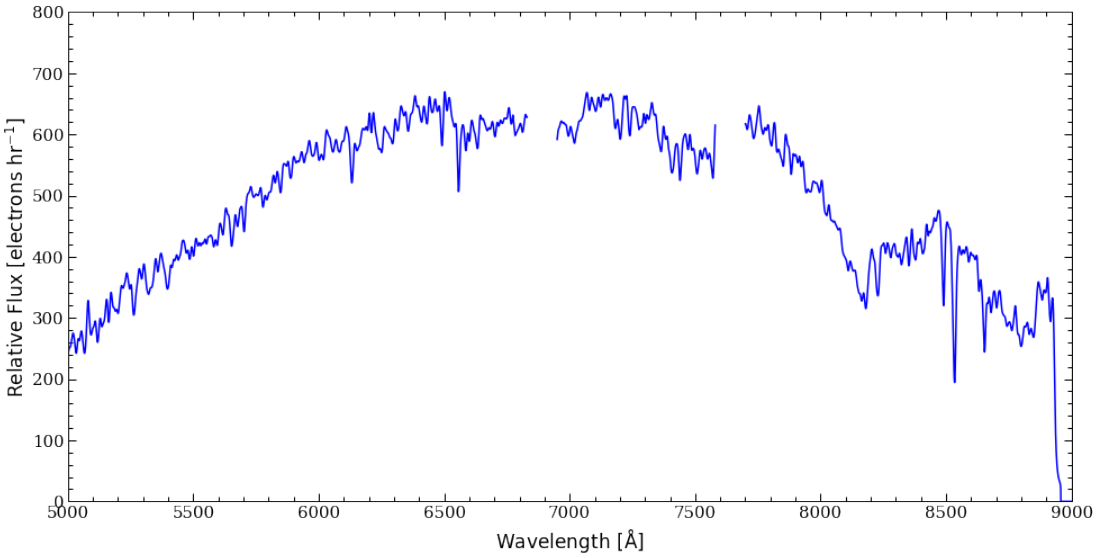

Figure 2.1: Example spectrum for a MS star from the SPLASH survey.

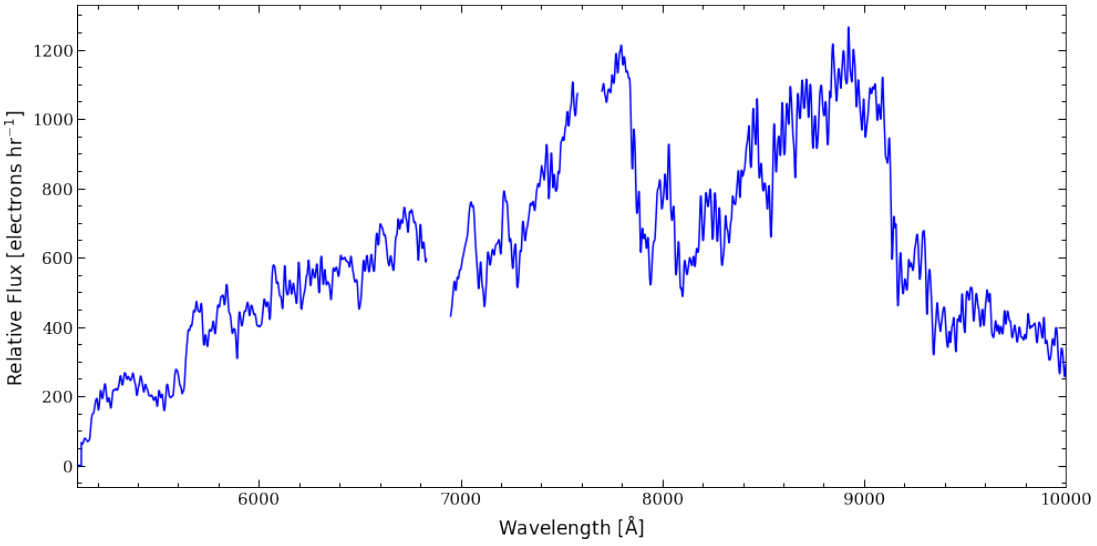

Figure 2.2: Example spectrum for a AGB star from the SPLASH survey.

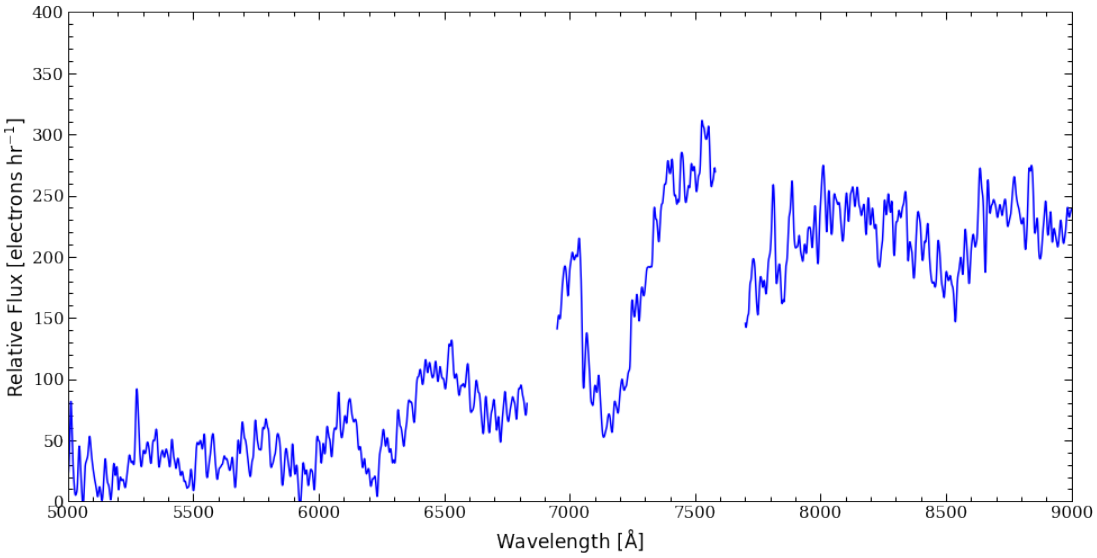

Figure 2.3: Example spectrum for a RGB star from the SPLASH survey.

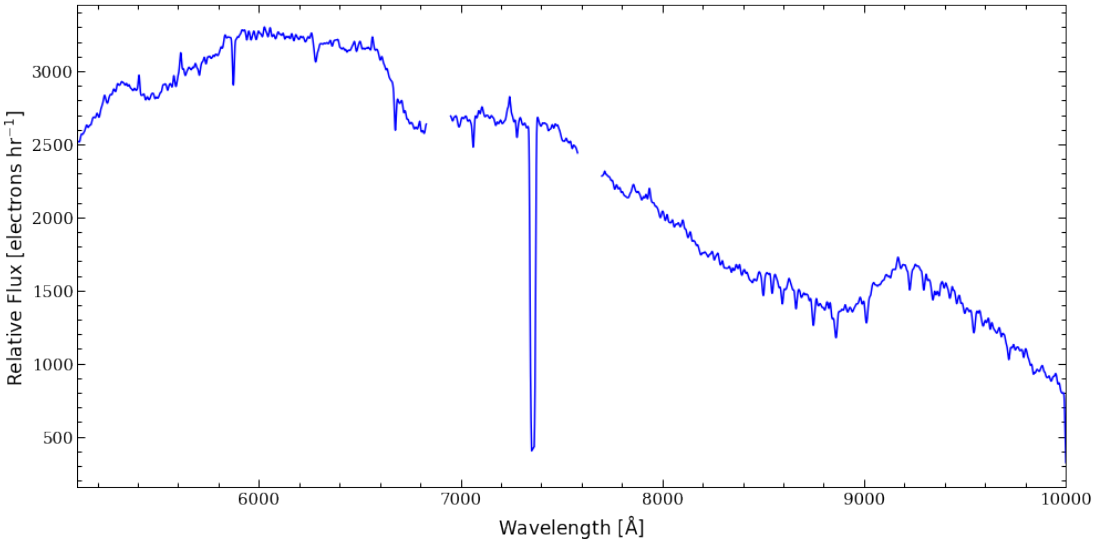

Figure 2.4: Example spectrum for a MS star from the TREX survey.

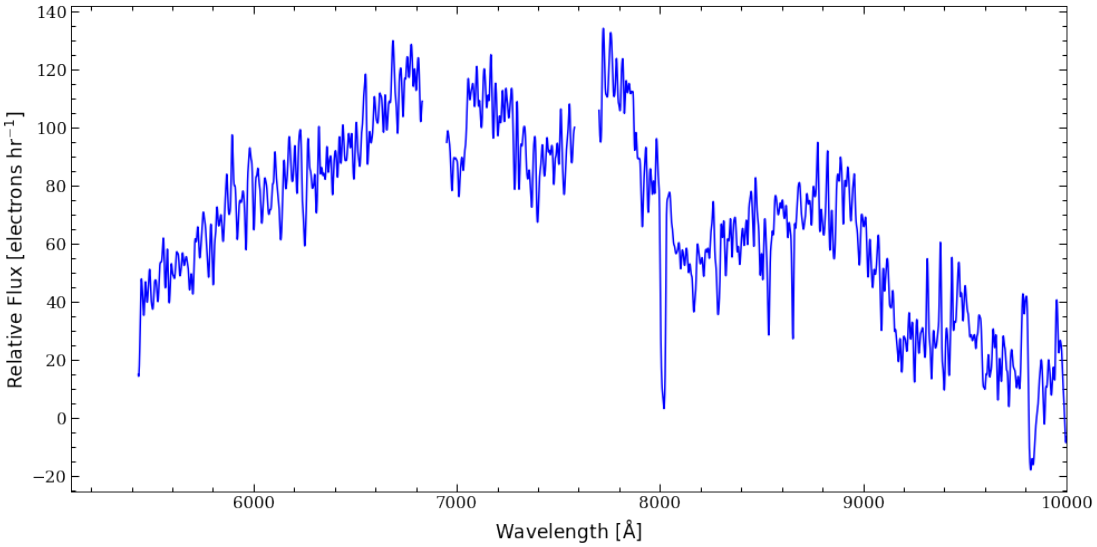

Figure 2.5: Example spectrum for a AGB star from the TREX survey.

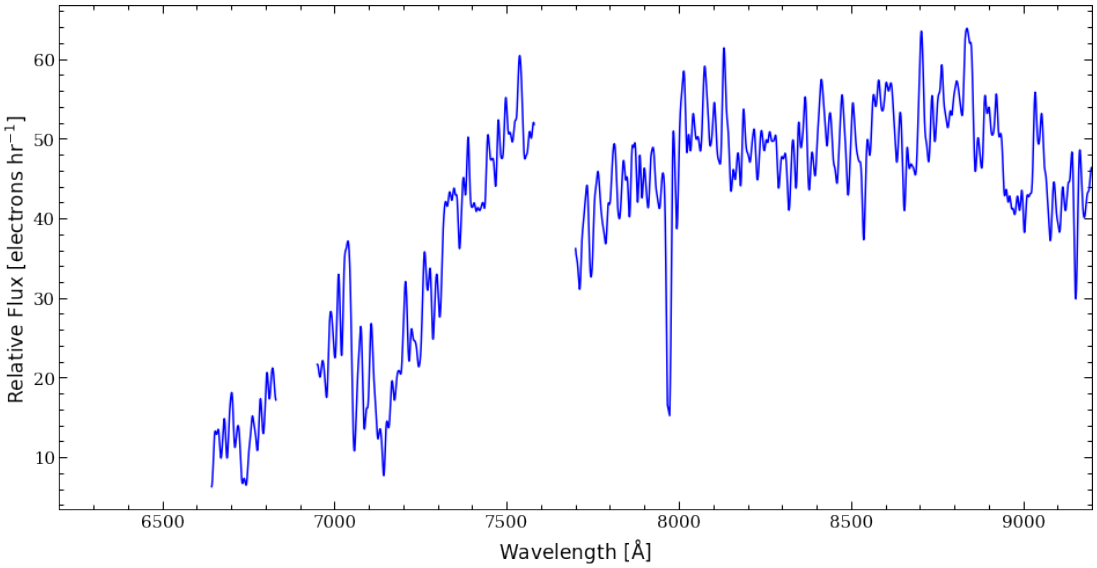

Figure 2.6: Example spectrum for a RGB star from the TREX survey.

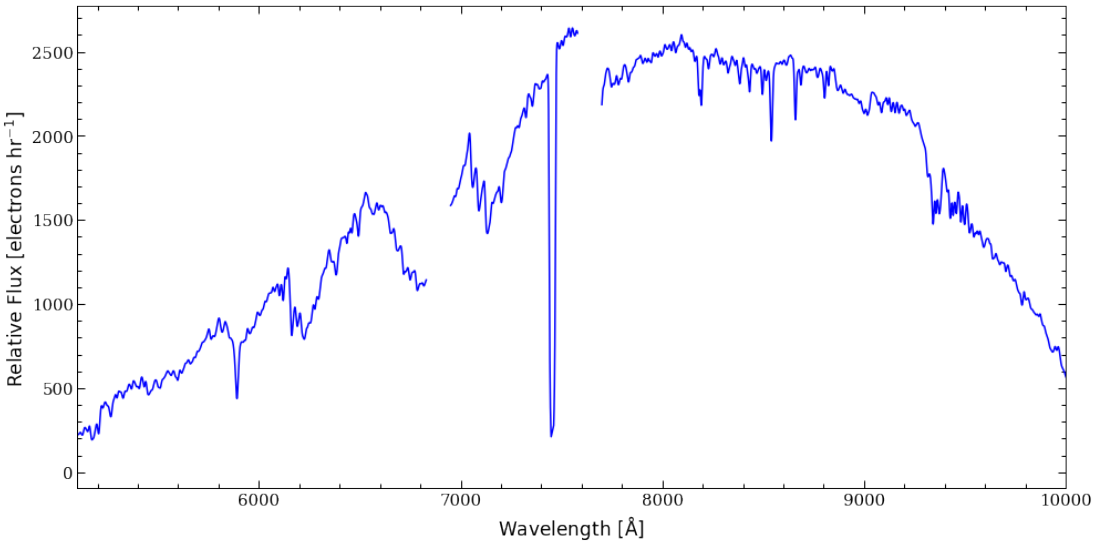

Figure 2.7: Example spectrum for a RHeB star from the TREX survey.

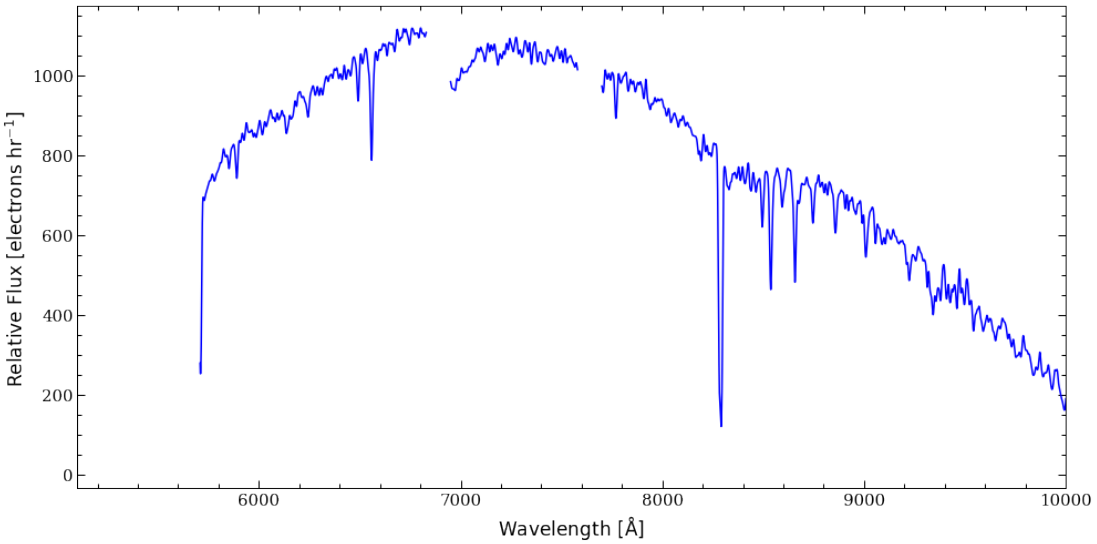

Figure 2.8: Example spectrum for a BHeB star from the TREX survey.

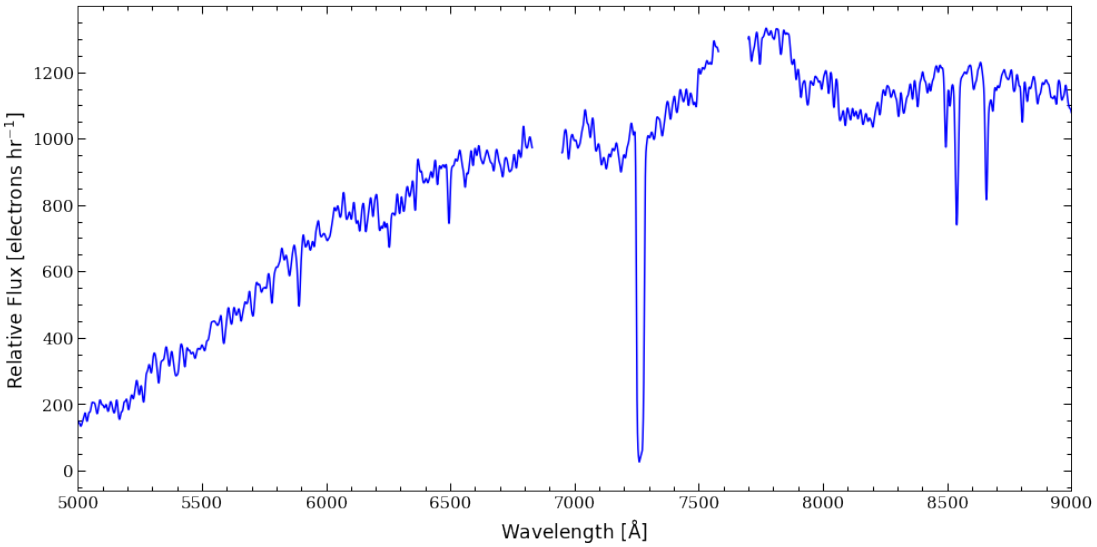

Figure 2.9: Example spectrum for a weak CN star from the TREX survey.

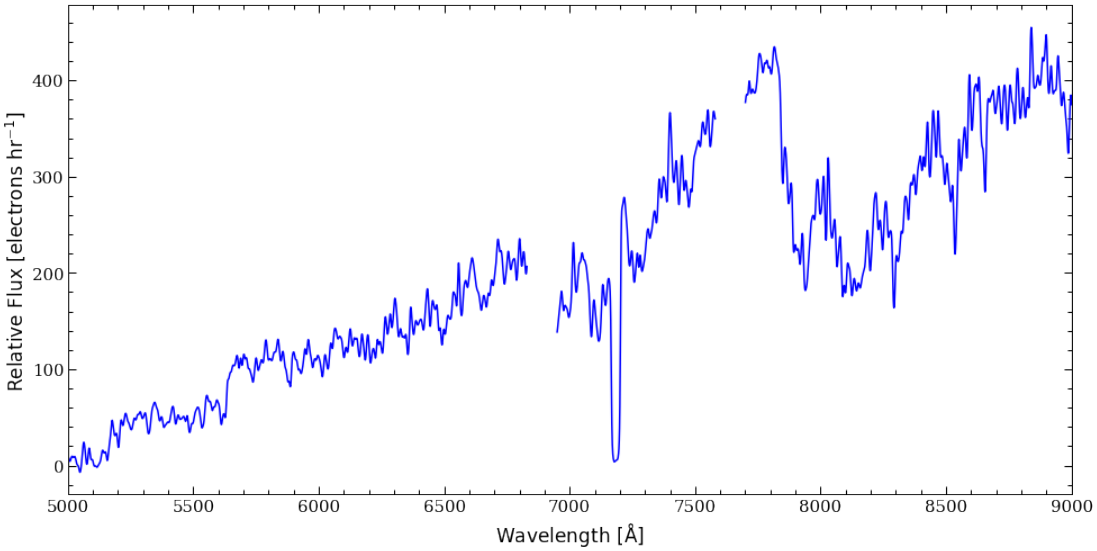

Figure 2.10: Example spectrum for a carbon star from the TREX survey.

Chapter 3

Asymmetric Drift in the Andromeda Galaxy (M31) as a Function of Stellar Age

3.1 Introduction

The kinematics of stars are shaped by a galaxy's heating history. The properties of present day galaxies cannot be explained without dynamical heating events (Seth et al. 2005; Walker et al. 1996). Spiral waves in the disks of galaxies have long been suspected as a source of heating, but in practice cause few changes in the amount of random stellar motions in a galaxy (Sellwood & Binney 2002; Sellwood 2014). Instead, mergers of satellite galaxies are needed to explain the stellar vertical velocity dispersions seen in the spiral galaxies of the Local Group (Leaman et al. 2017), as the mergers can

stir up the disk and perturb the orbits of stars (Quinn & Goodman 1986).

The dynamical effects of these events remain long after the event itself and result in greater velocity dispersion and thicker disks. Dynamical heating permanently disrupts the orbital paths of stars (Leaman et al. 2017) because stars are collisionless and are heated. Dynamical heating events cause stars to be displaced to greater radii, and conservation of angular momentum dictates that their orbital velocity decreases during this migration: $L = mvr$ (Binney & Tremaine 2008). Sellwood & Binney (2002) find that changes in the angular momentum distribution always increase random motion in stellar populations, which results in stars having greater velocity dispersion than gas. Gas is collisional and therefore can maintain more uniform circular orbits (Sellwood & Moore 1998). Thus, while stars have greater velocity dispersion than the surrounding gas, they tend to have lower circular velocities because the circular velocity is a smaller component of their total velocity.

The difference between the gas rotation velocity and the stellar rotation velocity at a certain radii is called asymmetric drift (v_a, lag, or AD) (Strömberg 1946). AD is a proxy for heating events because it suggests stars are on perturbed non-circular orbits. In addition to reflecting the accretion history of a galaxy, AD is also an important tool for learning about the current state of a galaxy. Specifically, it reflects the dynamics of the galactic disk and can be used to measure stability criterion (Westfall et al. 2007). Additionally, lag is a proxy for interactions with a bar (Dehnen 1998) and for velocity dispersion. Dorman et al. (2015) shows velocity dispersion increases with stellar age, for stars that are longer lived have experienced more dynamical heating. Since lag is a

proxy for velocity dispersion, we expect it to similarly increase with stellar age (Walker et al. 1996; Dehnen 1998; Dehnen & Binney 1998). This lag will be preserved in older populations because these populations are dynamically relaxed.

Making AD calculations requires measurements of a galaxy's stellar and gas motions. Integral-field-unit (IFU) spectroscopy allows astronomers to study the kinematics of galaxies by obtaining spectra along two dimensions (Martinsson et al. 2013) and are powerful enough to make AD measurements for even distant galaxies (Bershady et al. 2010). Martinsson et al. (2013) use IFUs from SparsePak (Bershady et al. 2004, 2005) to measure the AD of stars compared to ionized gas (OIII) in face on spirals and find that stars lagged behind the gas on average by 11 ± 8 %. This value is similar to other studies of lag in local galaxies (Ciardullo et al. 2004; Herrmann & Ciardullo 2009; Westfall et al. 2007, 2011) and in the Milky Way (MW) (Ratnatunga & Upgren 1997; Olling & Dehnen 2003). The Mapping Nearby Galaxies at Apache Point Observatory survey (MaNGA) will extend the sample of galaxies for which we have AD measurements (Bundy et al. 2015). IFU spectroscopy, however, cannot resolve individual stars in distant galaxies. In our own galaxy, on the other hand, we can measure the velocities of individual stars, which has allowed studies to account for AD when constructing rotation curves (RCs) of the MW (Golubov 2014; Huang et al. 2016). Lag has also been used to determine the local standard of rest and to identify warps in the MW, which could possibly be explained by dynamical interactions with the Galactic bar (Dehnen 1998).

Studies of AD in the MW are difficult and incomplete though, as we are limited

to the Solar neighborhood (Dehnen 1998). Examining the Andromeda galaxy or Messier 31 (M31) can give us a more complete idea of AD in a spiral galaxy because at a distance of 785 Mpc (McConnachie et al. 2005), we can measure velocities of individual stars and thus the stellar rotation and velocity dispersion. The main objective of this article is to compare the rotation velocity of four populations of stars in M31 to that of the gas, which is assumed to trace more circular motions. This gives us the opportunity to measure AD as function of stellar age and to verify the extent to which AD is a proxy for velocity dispersion (Bershady et al. 2010).

M31 is an interesting candidate for an AD study because it has experienced heating events throughout its lifetime. The outer halo of M31 shows tidal streams, which are believed to be relics of minor mergers (Hernquist & Quinn 1988, 1989). The mass of the stellar halo, on the other hand, can more easily be explained by a major merger (Bell et al. 2017; D'Souza & Bell 2018; Hammer et al. 2018). A major merger could also trigger the burst of star formation that occurred ∼2 Gyr ago (Williams et al. 2017, 2018; D'Souza & Bell 2018). The most recent major event, which created the Giant Stellar Stream (GSS), is believed to have occurred ∼1 Gyr ago and enriched the galaxy's inner halo (Ibata et al. 2001, 2005; Ferguson et al. 2002). These accretion events have affected the dynamics of M31 and have left it with a higher local velocity dispersion and a wider distribution of dispersion across the disk than that in the MW (Sysoliatina, K. et al. 2018; Budanova et al. 2017). This suggests M31 has had a more violent history or a prolonged period of accretion than the MW (Ferguson & Mackey 2016).

This paper is organized as follows: in Section 3.2, we describe the four datasets we use in this analysis. In Section 3.3, we explain how our stellar sample is divided into four age groups and the analysis of the dynamics and AD of each age bin. In Section 3.4, we analyze possible causes for additional structure seen in the RCs. The sources of substructure we examine include geometrical effects from the tilted ring model (Section 3.4.2) and the multiplicity in the HI (Section 3.4.3). Other possible sources are included in the Appendix. In Section 3.5, we summarize our results.

3.2 Data

This study uses four datasets from various surveys of M31: (1) spectroscopy from the Keck II telescope and DEep Imaging Multi-Object Spectrograph (DEIMOS) obtained as part of the Spectroscopic and Photometric Landscape of Andromeda's Stellar Halo (SPLASH) survey (Guhathakurta et al. 2005, 2006; Dorman et al. 2015), (2) photometry from Hubble Space Telescope (HST) and Advanced Camera for Surveys (ACS) and Wide Field Camera 3 (WFC3) imagers as part of the Panchromatic Hubble Andromeda Treasury (PHAT) survey (Dalcanton et al. 2012; Williams et al. 2014), (3) HI 21-cm data obtained at the Dominion Radio Astrophysical Observatory (Chemin et al. 2009), and (4) CO J $= 1 \rightarrow 0$ emission obtained by the IRAM telescope (Nieten et al. 2006). The HI data covers the full area of the HI disk, which includes all of the bright stellar disk. Of the four surveys, the CO data covers the smallest area, and the spatial coverage of the SPLASH survey in M31's disk is somewhat larger than that of the PHAT survey. Figure 3.1 compares the area coverage of the PHAT and SPLASH

surveys to the CO coverage. Each dataset is briefly described in the following subsections. For more details about the target selection, observations, and data collection, see the papers cited for each survey.

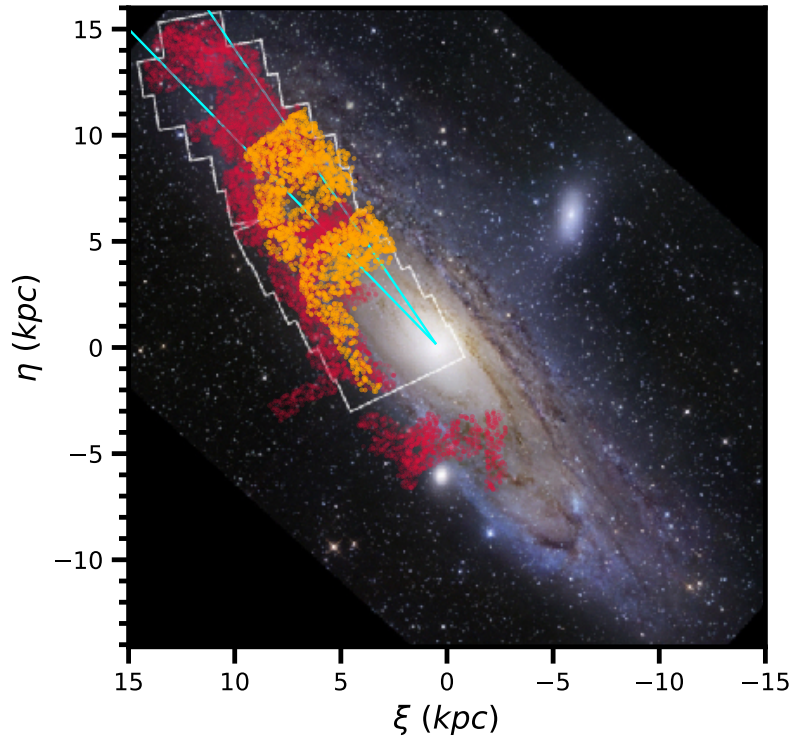

Figure 3.1: Map of survey coverage for the four datasets. The white outline represents the PHAT survey, the orange the CO coverage, and the red points show the SPLASH survey area. The HI survey covers the area shown in the image and extends beyond it. The aqua lines denote the wedge in which the tilted ring deprojection factor is small. This is further discussed in Section 3.4.2. The image of M31 was taken by Robert Gendler.

3.2.1 Keck DEIMOS Spectra

This paper is based on the portion of the SPLASH survey that targeted the disk of M31: Keck II/DEIMOS line-of-sight velocity measurements of $\sim 10,000$ stars

(Dorman et al. 2012, 2013, 2015). The 600 lines mm^{-1} grating was used for Fall 2012 observations, and the 1200 lines mm^{-1} grating for the rest of the (earlier) observations. Not all stars observed in the SPLASH survey had HST photometry; some were selected from ground based imaging. The stars chosen for this study overlapped with those observed by HST in the PHAT survey and were targeted to encompass a range of stellar evolutionary points: young hot massive stars on the main sequence (MS), intermediate mass asymptotic giant branch (AGB) stars, and low mass red giant branch (RGB) stars. Milky Way Foreground (MWFG) stars dominate the region where $1 < B - I < 2$, so we avoid selecting stars from this region (see Section 3.1.1 in Dorman et al. (2015) and Figure 3.2 for more details). A typical velocity error for stars in this dataset is on the order of 20 km s^{-1}. The target selection and data reduction process are described in Dorman et al. (2012, 2013, 2015).

3.2.2 HST PHAT Photometry

The PHAT survey is comprised of 117 million stars in M31 that have been observed with HST/ACS and WFC3. We use optical photometry of 6,000 stars that were bright enough for ground based spectroscopy and separated enough from nearby stars to be resolved and to avoid slit collision (Williams et al. 2014). Each star was observed in six filters, from the ultraviolet to the infrared: F275W, F336W, F475W, F814W, F110W, and F160W. The HST filter F275W corresponds to vacuum ultraviolet so does not have an equivalent ground based filter, but the remaining filters roughly correspond to the U, B, I, J, and H filter, respectively. We make use of the F475W and F814W filters when separating stars into age bins (Section 3.3.1) and F110W and

F160W when examining possible effects of reddening (Appendix 3.6.3).

3.2.3 DRAO HI Data

Chemin et al. (2009) collected HI 21-cm line data of M31 using the Synthesis Telescope with the 26-m antenna at the Dominion Radio Astrophysical Observatory. The telescope has the capability of resolving features down to $58'' \times 58''/\sin(\delta)$ in area. We use a subset of this catalog and only include data that correspond with the sightlines of the stellar data. As we explain in Section 3.4.3 in more detail, the HI spectrum can have multiple components with various possible origins (e.g. unresolved distinct HI disk structures within the synthesized beam, extraplanar components, expanding clouds, and/pr the warping of HI disk). Chemin et al. (2009) choose to use the velocity that is the largest offset relative to M31's systematic velocity, and we make the same choice for this analysis. We experiment with the effect of this choice in Section 3.4.3.

3.2.4 IRAM CO Data

Nieten et al. (2006) observed the molecular CO transition of $J = 1 \rightarrow 0$ emission from November 1995 and August 2001 with the IRAM 30-m telescope. The observations were obtained in *On-the-Fly* mode to obtain a total of 12 fields. The first set of fields was taken parallel to M31's minor axis. The field size was approximately $18' \times 18'$. The second fields were smaller in area, $9' \times 9'$, and were parallel to the major axis. The telescope scanned at a speed of $4'' \; s^{-1}$. Because of the duration of the survey, the telescope was regularly moved to nearby targets to verify its pointing. See Nieten et al. (2006) Section 2 for more details about the focusing, observation plan, and

data reduction. The CO emission is less likely to contain foreground contamination so is included in this analysis as a comparison to results relative to the HI. However, as seen in Figure 3.1, the CO does not extend the full stellar or HI coverage so cannot be used as a comparison in the outer regions.

3.3 Asymmetric Drift as a Function of Stellar Age

3.3.1 Age Groups

The stellar sample is divided into four age bins, from shortest lived to longest lived: massive MS stars, intermediate mass young AGB stars, intermediate mass older AGB stars, and low mass RGB stars. The divisions are based on the star's location in color magnitude space, as seen in Figure 3.2. The CMD uses filters F475W and F814W from HST (roughly B and I equivalent). We adopt the average age of each subpopulation from Dorman et al. (2015), who estimates the ages based on a simulated color-magnitude diagram with an age-metallicity relation derived from the RGB color distribution and assuming a constant star formation history. Since M31 has had multiple accretion events, it is unlikely to have had a constant star formation rate. However, a modeled CMD with a constant star formation history is valid in this analysis because we only want to place stars into broad age bins instead of identify their precise ages. This process yields average ages of 30 Myr for MS stars, 0.4 Gyr for the young AGB stars, 2 Gyr for the older AGB stars, and 4 Gyr for RGB stars.

When shown in $U - B$ color magnitude space, the MS star group shows three distinct populations that all have been categorized generally as MS: MS stars, blue loop

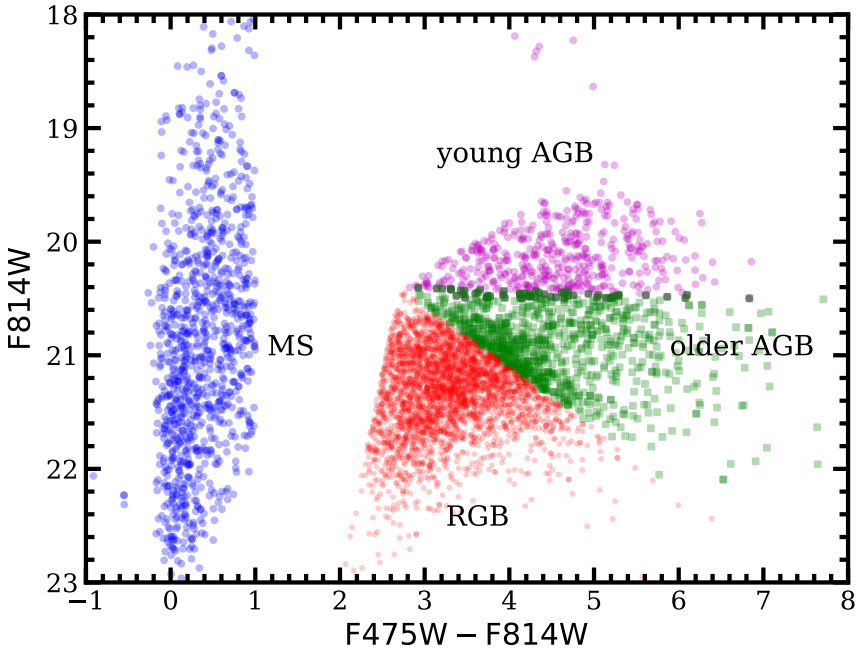

Figure 3.2: CMD for the stellar sample used in this analysis using filters F475W and F814W from HST (roughly B and I equivalent). The age bin divisions are shown in the different colors. Blue points represent MS stars, purple points young AGB stars, green squares older AGB stars, and red points RGB stars. The average ages are 30 Myr for MS stars, 0.4 Gyr for the young AGB stars, 2 Gyr for the older AGB stars, and 4 Gyr for RGB stars. MWFG stars dominate the color space $1 < \mathrm{F475W} - \mathrm{F814W} < 2$, so we avoid this region (see Section 3.1.1 in Dorman et al. (2015) for more details).

stars, and yellow supergiants. Although these are three separate populations, all are young ($\ll 1$ Gyr). RCs for each group do not show noticeable differences between the rotation velocities of the three subpopulations, so the MS group is kept as one age bin to avoid smaller sample sizes.

3.3.2 Line of Sight Kinematics

We examine the kinematics of each age group using the line-of-sight velocity obtained from the spectroscopy. The process of extracting velocities from the spectra

is described in Dorman et al. (2015). Figure 3.3 presents the position and individual line-of-sight velocity, average line-of-sight velocity, and velocity dispersion of each star for the four age bins. To average the velocities and calculate dispersion, we use a circle of 200″ for MS and RGB and 275″ for the less populated AGB bins. Each circle is centered on a star as in Dorman et al. (2015). Only data from circles containing at least 15 stars are kept. In Figure 3.3 there is a clear increase in local velocity dispersion and a decrease in the overall range of line-of-sight velocity from the younger to the older stellar populations (Dorman et al. 2015). The increase in random motions with stellar age suggests that M31 has been dynamically heated in the past and that this heating perturbed stars in the disk. Continuous heating can explain the gradual monotonic increase across age with all four age bins. In the next subsection we further analyze the differences in the kinematics of each age bin.

The smoothing circle technique creates a dataset in which points are not independent of one another because the circles overlap. To test the effect of this, we perform velocity averaging in a different way to create a dataset of *independent* mean velocities as a function of sky position. Instead of using smoothing circles centered on each star, we place a rectangular grid on top of the individual velocity maps and derive a local average velocity and velocity dispersion from the stars within each grid cell. In this method, each resulting averaged velocity is independent of the other averaged values. To maximize the number of resulting data points while maintaining enough stars in each cell for proper statistics, a different grid size is used for each age bin: 150″, 216″, 198″, and 100″ for MS, young AGB, older AGB, and RGB, respectively. A grid cell

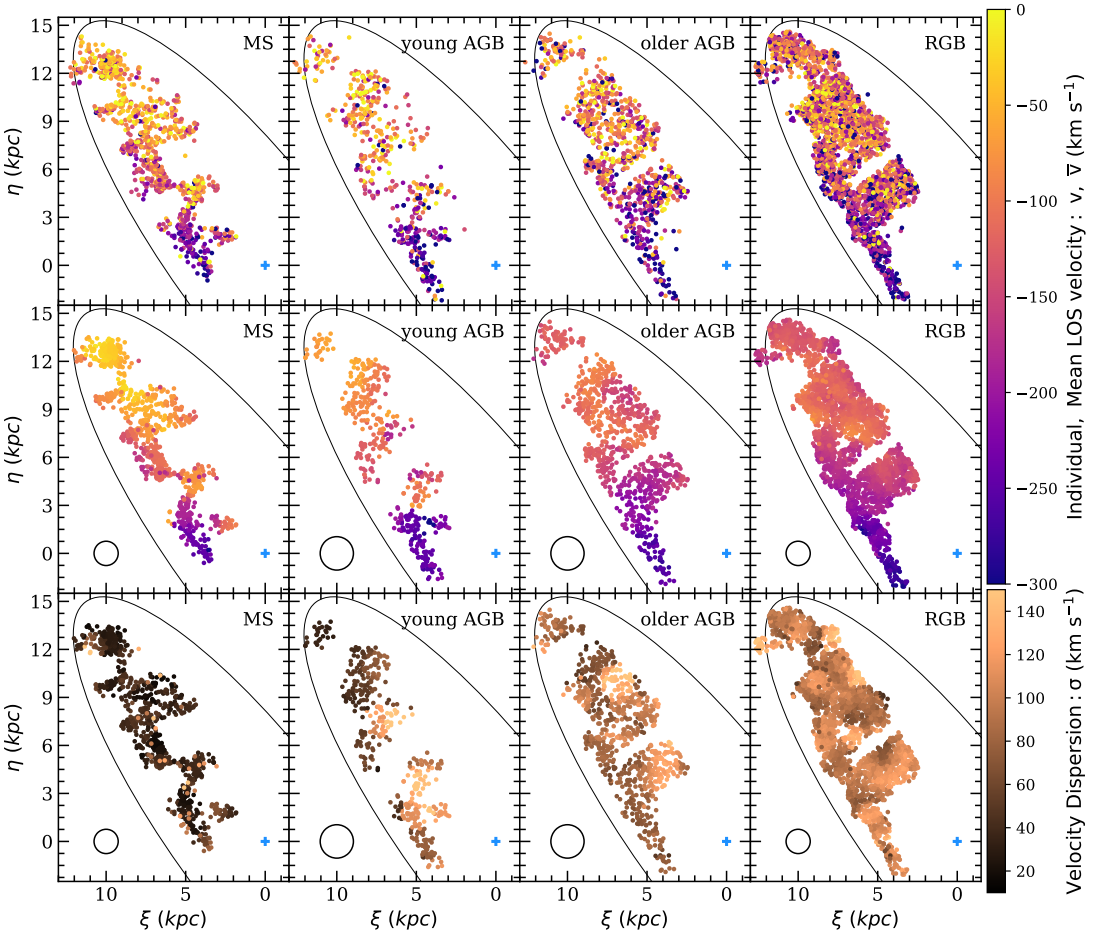

Figure 3.3: Individual line-of-sight velocity (top row), locally averaged line-of-sight velocity (middle row), and local velocity dispersion (bottom row) as a function of location and stellar age. From left to right: massive MS stars, young AGB stars, older AGB stars, and RGB stars. Smoothing circles are used to calculate the weighted mean of the velocity and the weighted root mean square error of the velocity (velocity dispersion). For AGB stars, a size of 275″ is used and a size of 200″ for MS and RGB stars is used. The circles in each panel of the bottom two rows show the respective sizes of the smoothing circles. The blue cross marks the center of M31. The ellipse is for visual reference of the disk. Local velocity dispersion increases with stellar age while the overall range of LOS velocities decrease, as found in Dorman et al. (2015).

is required to contain a minimum number of stars in order to contribute to the map. This minimum number is four for MS, young AGB, and older AGB and ten for the more populated RGB group. The resulting velocity maps and RCs do not differ significantly from the ones derived with the smoothing circles. Naturally, the map based on the non-overlapping rectangular grid method is much sparser than the map based on the overlapping circles method. Thus, we choose to use the averaging within overlapping circles analysis without the removal of outliers (with respect to the stars in each smoothing circle) for the rest of this paper so as to have the largest dataset possible.

3.3.3 Rotation Curves

Along with line-of-sight velocity, we compare the deprojected rotation velocities ($v_{\rm rot}$) of the stellar and gas populations. To deproject the averaged line-of-sight velocity into a rotation velocity, Equation 3.1 is used, where $v_{\rm sys}$ is the systematic velocity of M31 (-300 km s^{-1}), $v_\star$ is the averaged line-of-sight velocity of the star or gas at the same line of sight, and $PA_\star$ is the position angle of the star or gas at the same line of sight based on its location in the disk.

$$v_{\rm rot} = \pm \frac{v_\star - v_{\rm sys}}{\sin(i_{\rm TR})} \sqrt{1 + \frac{\tan^2(PA_\star - PA_{\rm TR})}{\cos^2(i_{\rm TR})}} \tag{3.1}$$

We use the tilted ring model from Chemin et al. (2009) to assign each star and gas line of sight a position angle ($\rm PA_{TR}$) and inclination angle ($i_{\rm TR}$). This model is used to account for the warps in the HI disk. The tilted ring model consists of dividing the disk into different annuli, each with a corresponding PA and i. The rings have a

Table 3.1: Chemin et al. (2009) Tilted Ring Model

Radius (kpc)	adopted PA (°)	adopted i (°)
4.95	33.6	63.7
5.33	33.9	65.9
5.71	35.4	68.1
6.09	36.4	69.7
6.47	36.6	72.0
6.85	36.5	73.5
7.23	36.4	74.3
7.61	36.8	74.6
7.99	37.3	74.5
8.37	37.7	74.3
8.75	38.0	74.3
9.13	38.3	74.4
9.51	38.7	74.8
9.90	39.0	75.2
10.28	39.1	75.6
10.66	39.0	76.1
11.04	38.8	76.3

width of 0.38 kpc, and the PA and i for each ring used in this study can be seen in Table 3.1. Chemin et al. (2009) extend the model to $r = 0.38$ kpc in the inner region and to $r = 130$ kpc in the outer region, but that is beyond the extent of the data used in this analysis. We use this model to place each star or gas sightline into a ring based on the deprojected distance from M31's center. We then assign a $\mathrm{PA_{TR}}$ and a i_{TR} to the star or gas line of sight based on which ring it lies in.

Table 3.1 (cont'd): Chemin et al. (2009) Tilted Ring Model

Radius (kpc)	adopted PA (°)	adopted i (°)
11.42	38.6	76.4
11.80	38.3	76.3
12.18	37.7	76.0
12.56	37.0	75.6
12.94	36.4	75.1
13.32	36.1	74.8
13.70	35.9	74.5
14.08	36.1	74.3
14.46	36.6	74.1
14.84	37.1	73.7
15.23	37.3	73.7
15.61	37.2	74.1
15.99	37.1	74.7
16.37	37.3	75.4
16.75	37.7	75.5
17.13	37.7	75.1
17.51	37.5	74.3

Table 3.1 (cont'd): Chemin et al. (2009) Tilted Ring Model

Radius (kpc)	adopted PA (°)	adopted i (°)
17.89	37.5	73.8
18.27	37.5	73.4
18.65	37.4	73.4
19.03	37.5	73.6
19.41	37.7	73.4
19.79	38.3	73.2
20.18	38.6	73.0

The averaged line-of-sight velocity is used to create the RCs in Figure 3.4, which show the deprojected rotation velocity against the deprojected radial distance from the center of M31. Each star is paired with a HI and CO velocity measurement that is closest in right ascension and declination to the star's position. The older populations show a decrease in the overall range of line-of-sight velocity compared to that of the younger populations (Figure 3.3) and also show a clear transition to lower rotation velocities, as shown by the color points in Figure 3.4. The RC for the HI along the stellar line of sight is represented by the grey points in the left panel of Figure 3.4, and the CO along the stellar line of sight RC is represented by the dark teal points in the right panel of Figure 3.4. The gas RCs are similar along all sightlines and do not vary regardless of whether the area of the disk is dominated by old or young stars. The extent of the CO data is smaller than the HI so does not extend to the outermost radii of the HI and stellar data. The young stellar age groups with higher rotation speeds more closely resemble the gas. Since the gas is collisional, it can be assumed to have a roughly circular orbital path. Interactions with the bar or with the spiral arms can perturb the gas, so this assumption is not necessarily correct in all circumstances

but is adequate for measuring AD. The younger stars with lower dispersion match the rotation velocity of the gas more than the older stars do. When orbits are disturbed, the circular component of the orbital velocity becomes a smaller component of a star's overall motion. Thus, a lower rotation velocity can be an indicator of noncircular orbits. The gap between the gas RC and the stellar RC is a visual representation of AD: the stars lag behind the gas. For the RCs in Figure 3.4, the strongest component of the HI is used if the HI spectrum has multiple peaks. In Section 3.4.3 we discuss additional AD analysis with different choices of HI component.

There is also scatter and substructure in the RC for each age bin for both gas components. When performing the velocity smoothing in Figure 3.3, outliers within each smoothing circle are not removed. As an experiment, the analysis is repeated, this time we remove the outliers to examine how the RCs change: for each smoothing circle, stars with line-of-sight velocities that are different than the median of all the line-of-sight velocities within the circle by three times the width of the distribution are removed. Only centers that retain at least 15 stars in the smoothing circle are kept. Removing outliers eliminates some scatter in the RCs but preserves a majority of the substructure. We explore other possible sources of the scatter and substructure in Section 3.4.

3.3.4 Asymmetric Drift

The RCs in Figure 3.4 show that there is an offset between the HI/CO and the stellar rotation velocity. We analyze this difference, the AD. AD is defined in Equation 3.2.

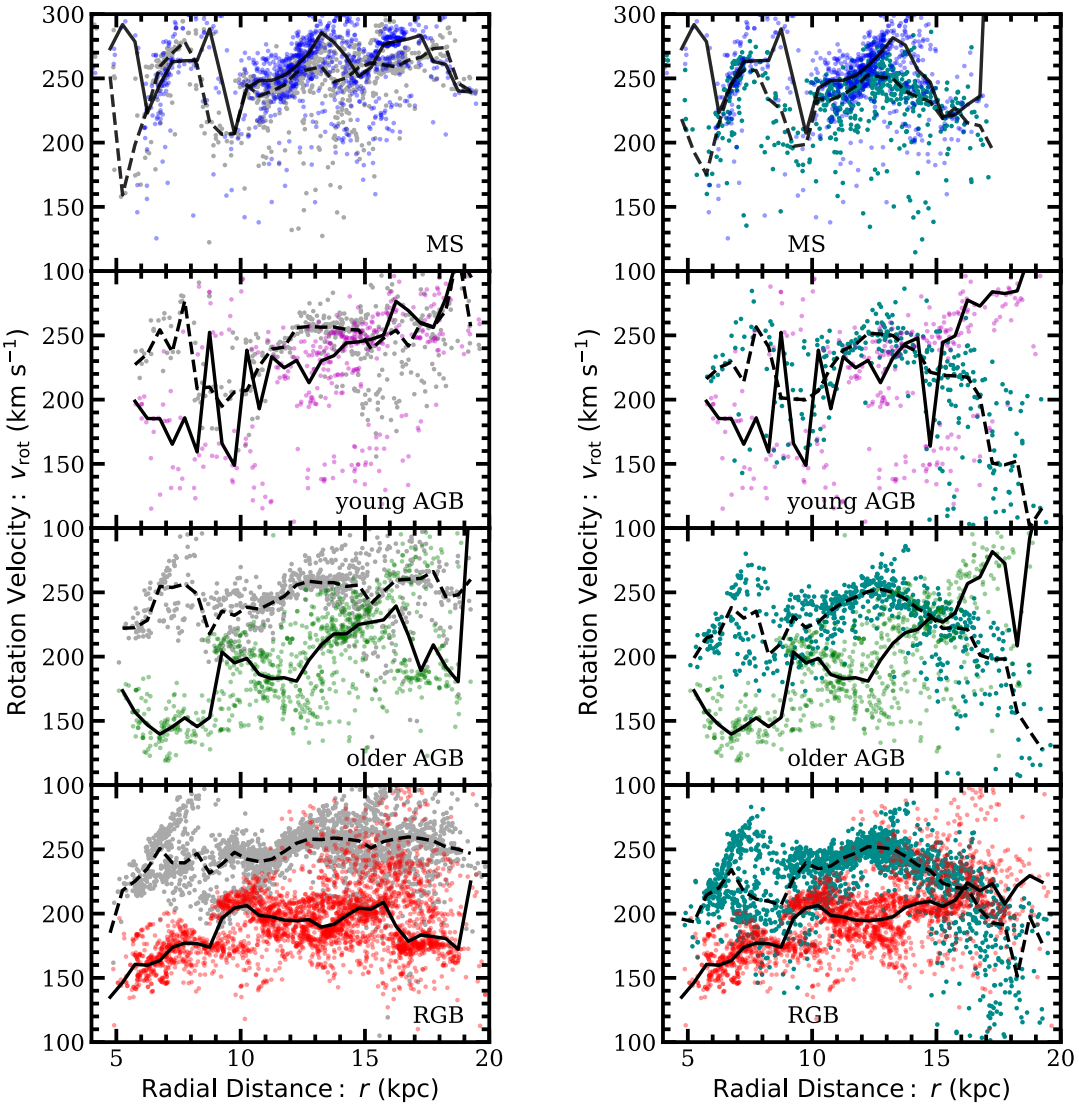

Figure 3.4: Deprojected RCs for the four stellar age bins and the paired main component of the gas velocity. From top to bottom: massive MS stars, young AGB stars, older AGB stars, and RGB stars. In each panel on the left, the gray points represent the HI along the same line of sight as the stars, and the color points represent the stars. On the right, the dark teal points represent the CO along the same line of sight as the stars and the color points represent the stars. The lines represent the median rotation velocity in a 0.5 kpc bin. The solid line represents the stars and the dashed, the gas. A titled ring model was used to account for the warps in M31's disk when deprojecting the line-of-sight velocity into a rotation velocity, as used in Chemin et al. (2009). The gap between the stellar RC and the gas RC, AD, increases monotonically with stellar age for both gas components.

$$v_a = v_{\rm rot,gas} - v_{\rm rot,\star} \tag{3.2}$$

Histograms of AD for each age bin are presented in Figure 3.5. The left panel shows AD with respect to the HI, and the right shows AD with respect to the CO. The range of AD is largest for the young AGB stars. One result of this is interesting substructure, which is addressed later in the paper. In both panels, the lag becomes larger with stellar age: the peak of the distributions shifts away from zero as stellar age increases.

The AD measurements with respect to both gas components are offset from one another. The difference in AD measurement is likely a result of the fact that the velocities for each gas component are calculated differently. The HI line-of-sight velocities are derived from Gaussian fits on the most extreme velocity peak in the HI spectrum. The CO line-of-sight velocities are derived from the first moment of the spectrum. Gaussian fits result in higher rotation velocities than velocities derived from first moment maps (Carignan et al. 1990).

For better comparison, we also derive the intensity weighted mean (IWM) of the HI line-of-sight velocities. To do this, we average the HI line-of-sight velocities across all HI peaks, which more closely resembles the first moment based CO velocities. The results of this analysis can be seen in Table 3.3.4 and in Figure 3.6. Table 3.3.4 shows median AD values and the corresponding one sigma standard errors on the median. Figure 3.6 shows how the median AD values evolve with stellar age. The solid gray line shows the AD relative to the HI velocities that were derived by Gaussian fits, and

the dashed gray line shows the AD relative to the HI IWM velocities. The difference between the HI IWM AD measurements and CO AD measurements is smaller than the AD measurement relative to the HI Gaussian fit velocities. The remaining small differences could be caused by different resolutions, gas properties, and the fact that while the two velocity measurement methods, first moment versus IWM are more similar than before, they are not identical. Furthermore, we see that the CO gas rotation speeds better match the rotation speeds of the young MS stars, which is what is expected based on the fact that young stars are born out of molecular gas. In the rest of the paper, we use HI line-of-sight velocities based on Gaussian fits to the most extreme velocity peak in the spectrum because the complexity of the HI spectrum makes the IWM an inferior measure of the rotation speed.

Surprisingly, the MS population shows a negative median AD value, suggesting the HI and the CO gas lag behind the stars. This implies the young stars are more settled into the circular velocity of the galactic potential than the collisional gas. Young stars are born in gas that is denser than the gas in this analysis so it is most likely that using HI or CO ($J = 1 \rightarrow 0$) as a proxy for circular motion is not perfect. Figure 3.14 shows that not all of the younger stars are leading the gas. In particular, there are groups of stars at 13-15 kpc that trail the gas like the other age groups. The explanation for this is not apparent. The two oldest age bins lag behind the stars on average by 20% and up to 40%, which is greater than the AD that is seen in the MW and other local galaxies (Ciardullo et al. 2004; Olling & Dehnen 2003). This suggests M31 has had a particularly violent heating history.

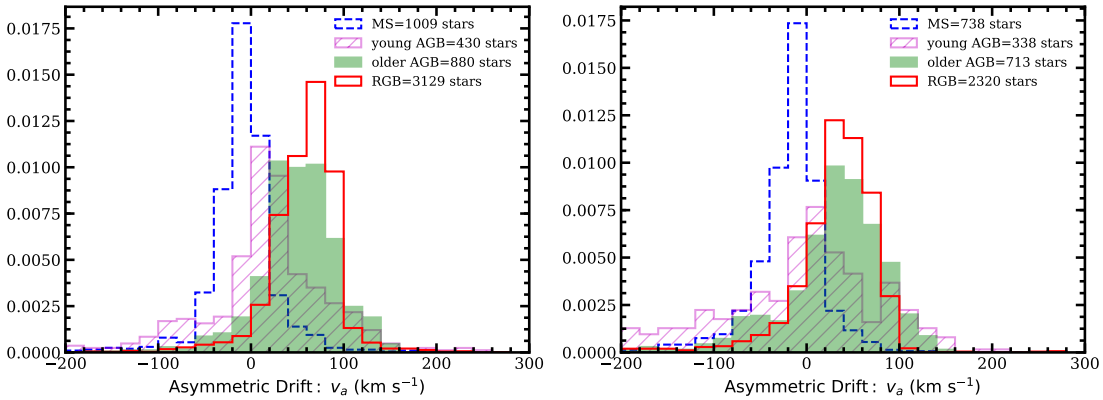

Figure 3.5: Normalized distributions of AD (Equation 3.2) for the four stellar age bins. In both panels, the histogram denoted by blue dashed line represent the massive MS stars, the ones with the purple stripes represents the young AGB stars, the green solid histograms represent the older AGB stars, and histograms denoted by the red line represent the RGB stars. The left panel shows the AD with respect to the HI and the right, AD with respect to the CO. The legend also contains the number of stars in each age bin. The magnitude of AD increases monotonically with stellar age.

Table 3.2: Median AD Values

Stellar Group	AD w.r.t HI (km s^{-1})	AD w.r.t HI IWM (km s^{-1})	AD w.r.t CO (km s^{-1})
MS	$-8.15^{+0.74}_{-0.72}$	$-13.54^{0.68}_{0.88}$	$-12.86^{+1.38}_{-0.86}$
young AGB	$17.69^{+3.29}_{-2.78}$	$6.32^{1.79}_{3.99}$	$0.18^{+6.38}_{-4.17}$
older AGB	$50.43^{+1.09}_{-1.26}$	$36.45^{1.30}_{1.45}$	$36.99^{+2.09}_{-1.55}$
RGB	$62.97^{+0.59}_{-0.40}$	$50.43^{0.46}_{0.39}$	$37.15^{+0.79}_{-0.64}$

Examining the transition to decreased rotational velocity with stellar age can give us detailed insight into the heating history of M31. Previous studies on the formation of M31 have not considered AD of different stellar populations. In theory, a smooth transition between the age bins suggests the heating was continuous. On the other hand, a sudden jump in lag between the age bins instead suggests that there was one event or sporadic events that heated the disk. In this analysis, we see an increase in lag at all age bins, as shown in Figure 3.6. This monotonic increase of AD suggests M31 has had relatively continuous accretion: there have been mergers before and after larger events, like the creation of the GSS (Ferguson & Mackey 2016; Sadoun et al. 2014) or the event that caused the star formation burst that occurred 2 Gyr ago (Williams et al. 2017, 2018; D'Souza & Bell 2018). While this analysis supports that multiple and relatively frequent mergers are needed to explain the trend of increasing AD with stellar age in M31, we cannot determine whether minor or major mergers are more important for creating this phenomenon. A comparison to simulations will be the subject of future work and will better answer the question of whether a major merger or minor mergers can recover the current dynamics of M31's disk.

Additionally, the shape of the velocity ellipsoid is beyond the scope of this paper but will be the subject of future analysis. This future analysis will include an extended sample of stars with greater azimuthal coverage but coarser age resolution. Measuring the shape of the velocity ellipsoid will constrain tangential anisotropy and will help determine the accuracy of the Jean's equation to model AD. Preliminary work with the asymmetric Jean's equation was done in Dorman (2015), and the predicted

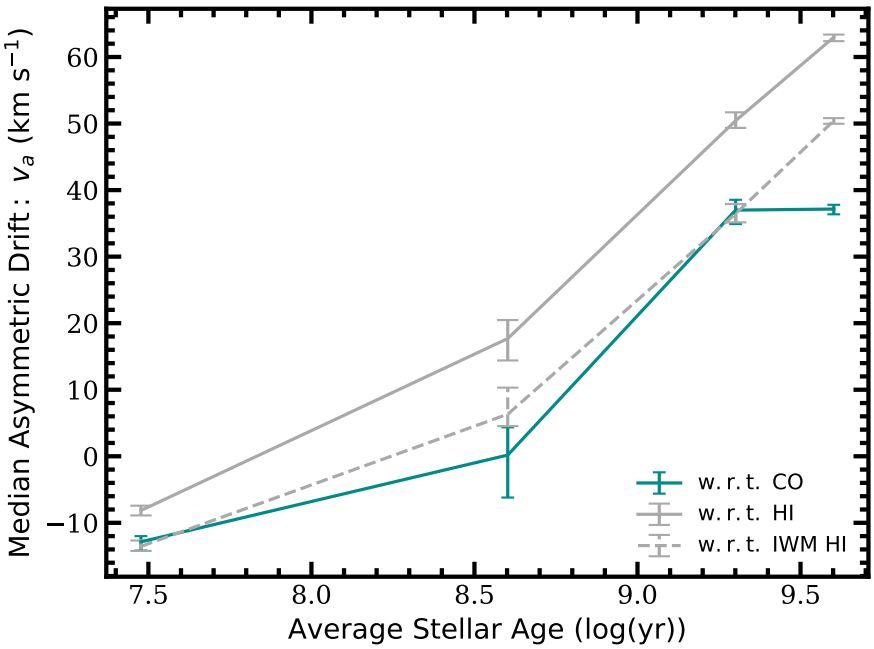

Figure 3.6: Average stellar age against median AD. The upper and lower error bars represent the one sigma confidence level on the median. The teal represents AD with respect to the CO gas, and the solid gray line represents AD with respect to the HI gas, as shown in Figure 3.5. The dashed gray line represents the AD with respect to the HI gas, where the velocity is intensity weighted (instead of determined by a Gaussian fit). The IWM method is more similar to how the CO velocities are determined. There is a monotonic increase in AD across every age bin, which suggests M31 has had relatively constant heating.

AD values are consistent with our measured values.

3.4 Exploring the Substructure in the RCs (and Resulting Scatter in the Asymmetric Drift)

As presented in the previous section, there is a clear correlation between lag and stellar age. In addition to this trend, the RCs in Figure 3.4 show substructure and scatter that cannot immediately be explained. In this section, we explore different possible sources that could be causing the messiness, and we examine the effects on AD measurements. Figure 3.7 shows maps of the four stellar age groups, and color represents AD values. This plot will be referred to throughout this section. Because the CO data does not extend the full stellar disk and does not contain peak multiplicity information, we limit the following analysis to the HI gas.

3.4.1 Halo Star Contamination

Because the disk is thick but not infinite, there is a risk that a sample of this kind could contain halo stars that are at the same sightlines as our data but beyond the finite disk scale height. Halo stars are old, and they exhibit lower rotation velocities than older stars in a disk. Including halo stars in our sample would skew our measured AD value. Dorman et al. (2013) decompose the bulge, disk, and halo of M31 using the luminosity function of bright stars from the PHAT survey, radial velocities of RGB stars from the SPLASH survey, and surface brightness profiles. Using these three criteria, they find that our sample is dominated by disk stars with negligible the halo and bulge star contamination. Furthermore, while having halo stars in our sample would increase the RGB AD, it would not affect the AD measurements for the other stellar age bins.

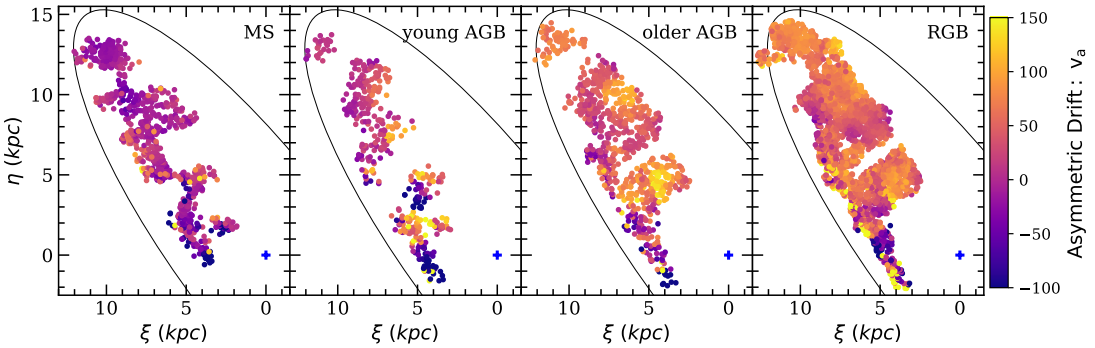

Figure 3.7: Maps of AD for the four age bins. Left to right: massive MS stars, young AGB stars, older AGB stars, and RGB stars. Color represents AD. The center of M31 is marked with the blue plus symbol in each panel. The ellipse is for visual reference. AD increases with stellar age.

We see that AD increases monotonically with age across all four age bins, so it is unlikely the high AD for the RGB group is caused by the presence of halo stars in that particular subsample.

3.4.2 Geometrical Effects

There is a possible geometrical effect resulting from the tilted ring model (Equation 3.1) that could cause some of the the RC scatter in Figure 3.4. The deprojection factor is the term inside the square root in Equation 3.1, and it depends on position angle. This term varies from one to infinity depending on where the star is in the disk. If the star lies on the major axis, this factor is at a minimum. Stars with small deprojection factors lie in the wedge area denoted by the aqua lines in Figure 3.1. If however, the star is on the minor axis, the deprojection term approaches infinity, regardless of the inclination: on the minor axis $\mathrm{PA}_\star - \mathrm{PA}_{\mathrm{TR}} = 90$, so the tangent will be undefined. This drastic increase in the projection factor amplifies the inability of

the tilted ring model to perfectly represent the disk. We separate sightlines for each age bin into two categories: the first has deprojection factors less than the median of the age bin, and the second has factors greater than the median. The left panel of Figure 3.8 shows the RCs that correspond to sightlines with lower deprojection factors, and the right panel shows the RCs that correspond to sightlines with higher deprojection factors. The RCs that correspond to sightlines with lower deprojection factors are flatter and contain less scatter than those corresponding to sightlines with a greater deprojection factor. This is especially clear in the HI RCs, which do not depend on stellar age. Because Equation 3.1 has no age dependence, each age bin is affected by the behavior of the deprojection factor equally. The trend of monotonically increasing AD with stellar age is clearer in the RCs that correspond to low deprojection factors. It is even stronger in these panels, as compared to the right panels, in which this trend is overshadowed by the scatter in the RCs. Furthermore, both the gas and the stellar line-of-sight velocity are deprojected by the titled ring model, so the model should not influence our measurements of AD. Figure 3.7 shows there is no strong azimuthal preference for higher or lower AD. There is a clustering of negative AD values with a large magnitude in the right most panel; these high AD values could be coincident with the bar. Most of the scatter in the RCs can be contributed to the tilted ring model being imperfect, but the source of the greater substructure in the RCs is still unclear. The RCs for the sightlines with low deprojection factors reveal the dramatic substructure in the older AGB population. Perhaps there are old AGB stars along the same line of sight as gas left over from recent star formation that is causing the shape of the RC.

This substructure could also be a result of minor mergers that disrupted this population of stars.

The right panel of Figure 3.8 shows the tilted ring model is not sufficient to describe the complexity of M31's disk structure. We construct RCs using a infinitely thin disk model, as described by Equation 3.3 to see if perhaps a simpler model decreases the scatter in the RC. Unlike the titled ring model, each star is given the same $\mathrm{PA_{TR}}$ and $\mathrm{i_{TR}}$. These values are the average of the $\mathrm{PA_{TR}}$ and $\mathrm{i_{TR}}$ ($\mathrm{PA_{TR,avg}}$ and $\mathrm{i_{TR,avg}}$) values used in Figure 3.4.

$$v_{\mathrm{rot}} = \pm \frac{v_\star - v_{\mathrm{sys}}}{\sin(i_{\mathrm{TR,avg}})} \sqrt{1 + \frac{\tan^2(PA_\star - PA_{\mathrm{TR,avg}})}{\cos^2(i_{\mathrm{TR,avg}})}} \tag{3.3}$$

The RCs using this model are shown in Figure 3.9. The resulting curves perhaps have less substructure than those in Figure 3.4 but not by a significant amount. This suggests that the geometry of M31's disk cannot be explained by a simple model either and also suggests that the substructure is complicated. Despite the inadequacy of the tilted ring model and infinitely thin disk model, we see that AD increases monotonically as a function of stellar age. Since this trend exists in both models, we believe that this is a real phenomenon.

3.4.3 The Multiplicity in the HI Spectrum

Chemin et al. (2009) observe the HI gas in M31 and find inner and outer HI warps. A single line of sight can thus pass through several HI clouds, causing there to be more than one peak in the HI spectrum. Chemin et al. (2009) do not limit their

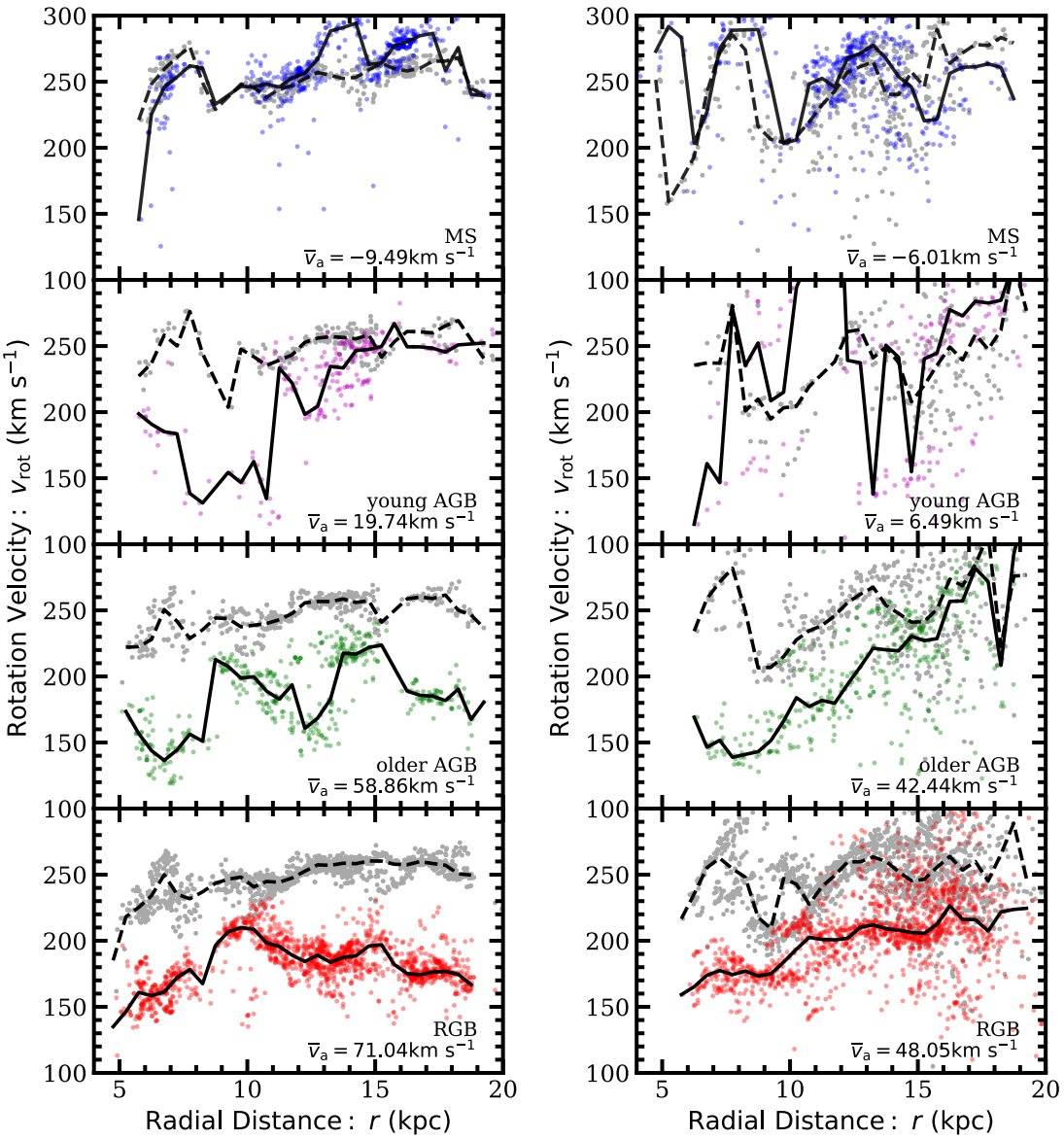

Figure 3.8: Left panel: the RCs for sightlines where the deprojection factor from Equation 3.1 is lower than the median factor for each age group. These sightlines represent stars in the wedge denoted by the aqua lines in Figure 3.1. The right panel is the RCs for sightlines where the deprojection factor is above the median for the age group. From top to bottom: massive MS stars, young AGB stars, older AGB stars, and RGB stars. In each panel, the gray points represent the HI and the color points represent the stars. The lines represent the median rotation velocity for 0.5 kpc bins. The solid line is for the stars and the dashed for the gas. Each panel shows the median AD values. The left panels show less scatter and a clearer trend of increasing AD with stellar age.

data analysis to a single or double peak fit so as to be able to account for more than two peaks in the spectrum. They find the multiplicity of HI ($N_{\rm HI}$) can range from one to five.

One result of this complexity is that the positions of stars can be measured inaccurately even when using a tilted ring model: a star and HI line of sight can be incorrectly assigned to the same radial bin, making substructure in the RCs. Figure 3.10 shows maps of the stars in this sample, and the color represents the number of components in the HI spectrum at that line of sight. Inner radii are more likely to have multiple components than outer radii. This is consistent with findings from Chemin et al. (2009): the HI disk is highly inclined at large radii, and the outer warp is projected along the line of sight onto inner regions, giving the illusion that there are multiple warps at small radii. The complexity in the inner regions is coincident with the location of the bar, which causes perturbations in the gas structure and dynamics via disruption and/or collision of gaseous clouds in warped crowded orbits and high speed clouds along orbits aligned with the bar. This also disrupts the HI inner ring, which causes structures at $r \sim$ 2.5 kpc and $r \sim$ 5 kpc (Chemin et al. 2009). These two sources of complexity in the HI line-of-sight velocities, (1) the outer warp leading to the projection of outer gas onto gas at smaller radii and (2) interactions with the bar, could cause substructure in the RCs. Comparing Figure 3.10 and Figure 3.7, we see the most complex sightlines, as denoted by five peaks in the HI spectrum, appear to also be the location of the greatest AD. The interactions with the bar that are causing the substructure in the RC could also be a source of the high magnitude of AD in this region. Thus, the gas and the stars

might be being perturbed by resonances associated with the bar.

The multiple peaks in the HI spectrum means a line of sight has multiple HI velocities. Typically, the velocity corresponding to the strongest peak (the velocity is that is largest in magnitude relative to the velocity of the system) is used in analyses, as we have done in this paper. We experiment with how this choice affects the RCs by comparing two velocities: that of the strongest peak and that of peak that corresponds to the velocity that is closest to the star's velocity at the same line of sight. The RCs do not differ in a noticeable way, so there is no trend between this choice of HI velocity and the stellar velocity dispersion (or AD). The RCs for this analysis can be seen in Appendix 3.6.1.

We also examine if the number of components in the HI spectrum is correlated with substructure in the RCs. Figure 3.11 shows the RCs for the RGB stars grouped into subsamples based on the number of peaks in the HI spectrum along the corresponding sightlines, from one peak to five peaks. While there is a clear lack of data points in the first 10 kpc whose line of sight correlates to an HI spectrum with a single peak, there is substructure and scatter regardless of the number of HI components. This is consistent with Figure 3.10 and findings by Chemin et al. (2009) that the inner radii of the HI disk have a more complicated shape. In the warped inner region, it is especially difficult to account for the geometry of the disk even with a tilted ring model (Sadoun et al. 2014). The median AD value varies throughout the subgroups but is surprisingly almost the same for the group with $N_{\rm HI} = 1$ as for the group with $N_{\rm HI} = 5$. Furthermore, the stars still lag behind the gas regardless of the number of peaks in the corresponding

HI spectrum. We see similar findings in all age bins; the RCs for the shorter lived MS stars, young AGB stars, and older AGB stars can be seen in Appendix 3.6.1 .

Figure 3.12 shows the radial distance, AD, and number of components in the HI spectrum along the line of sight for each star in the four age bins. For the AGB and RGB stars, there is a greater width of the distribution of lag at large radii ($r > 15$ kpc). This is counter to what is expected from the trend seen in Figure 3.11: since the HI spectrum is better behaved at outer radii, we would expect there to be less of a spread in lag at large radii and instead see a wider distribution of AD at smaller radii where the HI has multiple components in its spectrum. This discrepancy could be signs of an additional outer warp that does not present itself in the number of components in the HI spectrum.

We also look for possible correlations between the complexity of the line of sight as indicated by the HI and the velocity dispersion or AD. The top panel of Figure 3.13 shows cumulative histograms of the velocity dispersion for each age group. The bottom panel shows the cumulative AD histograms for the subgroups. The age groups are further divided into subpopulations based on the number of peaks in the HI spectrum along the line of sight. In general, the sightlines corresponding to multiple peaks in the HI spectrum have a greater magnitude of AD and velocity dispersion than the sightlines with a single HI component. Similarly, sightlines with five components in the HI spectrum always have greater velocity dispersion and AD magnitude than the other sightlines that correspond to fewer HI peaks. This is especially clear for the MS age group: the fraction of stars with $v_a \leq 0$ decreases as the number of HI components

increases. The difference between the multiplicity subgroups in the RGB age bin is smallest; there is less of a correlation between multiplicity in the HI spectrum and lag (or velocity dispersion) for longest lived populations. The dependence on HI multiplicity is most significant in the young AGB stars. Figure 3.13 also has vertical reference lines to highlight AD and velocity dispersion increase with stellar age despite the number of peaks in the HI spectrum.

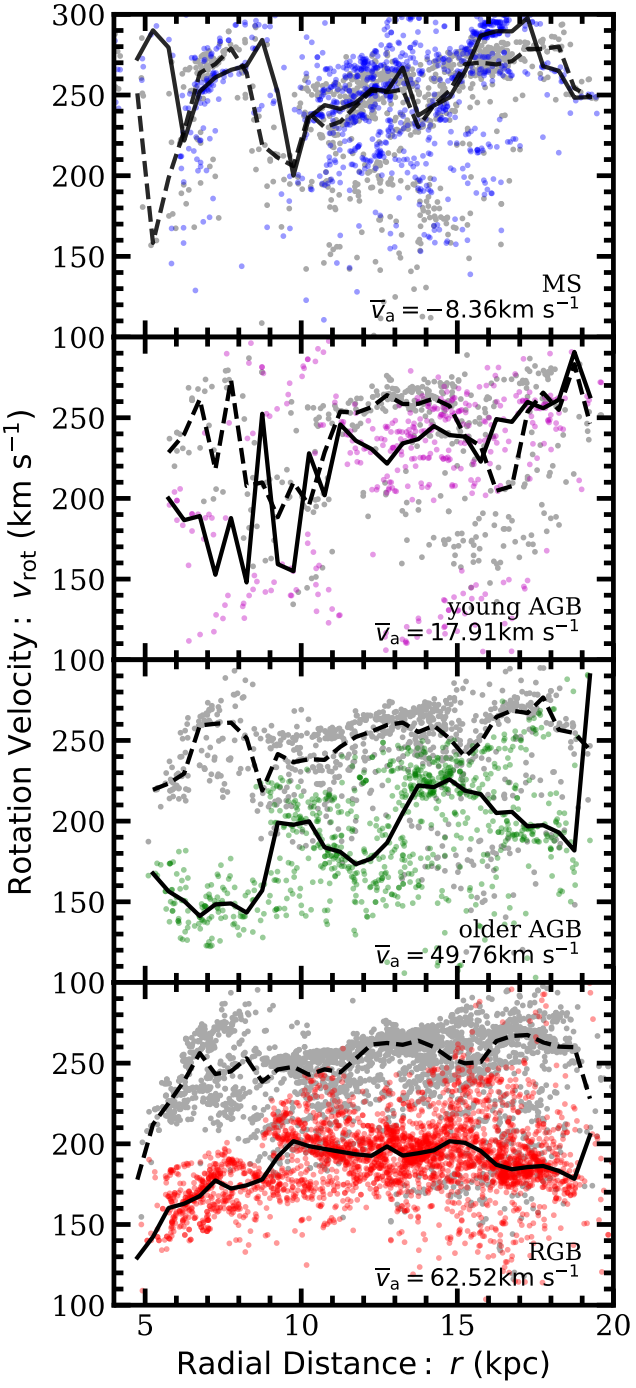

Figure 3.9: Deprojected RCs for the four stellar age bins and for the main component of the HI along the corresponding line of sight using an infinitely thin disk model instead of the tilted ring model. From top to bottom: massive MS stars, young AGB stars, older AGB stars, and RGB stars. In each panel, the gray points represent the HI and the color points represent the stars. The lines represent the median rotation velocity for 0.5 kpc bins. The solid line is for the stars and the dashed for the gas. Each panel shows the median AD values. Like in Figure 3.4, there is scatter and substructure in the curves, which shows a simpler model does not better represent the geometry of M31's disk.

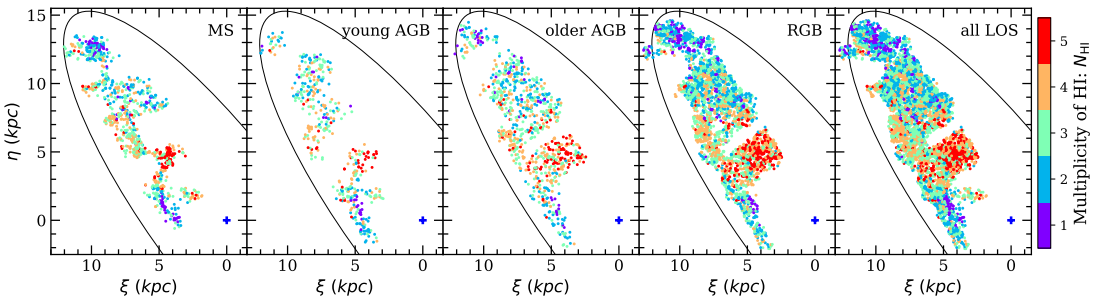

Figure 3.10: Multiplicity of HI maps for the four age bins. Left to right: massive MS stars, young AGB stars, older AGB stars, and RGB stars. Color represents the number of peaks in the HI spectrum along the line of sight. The center of M31 is marked with the blue plus symbol in each panel. The ellipse is for visual reference. The sightlines with multiple components in the HI spectrum are more likely to be in inner regions and may be coincident with the bar.

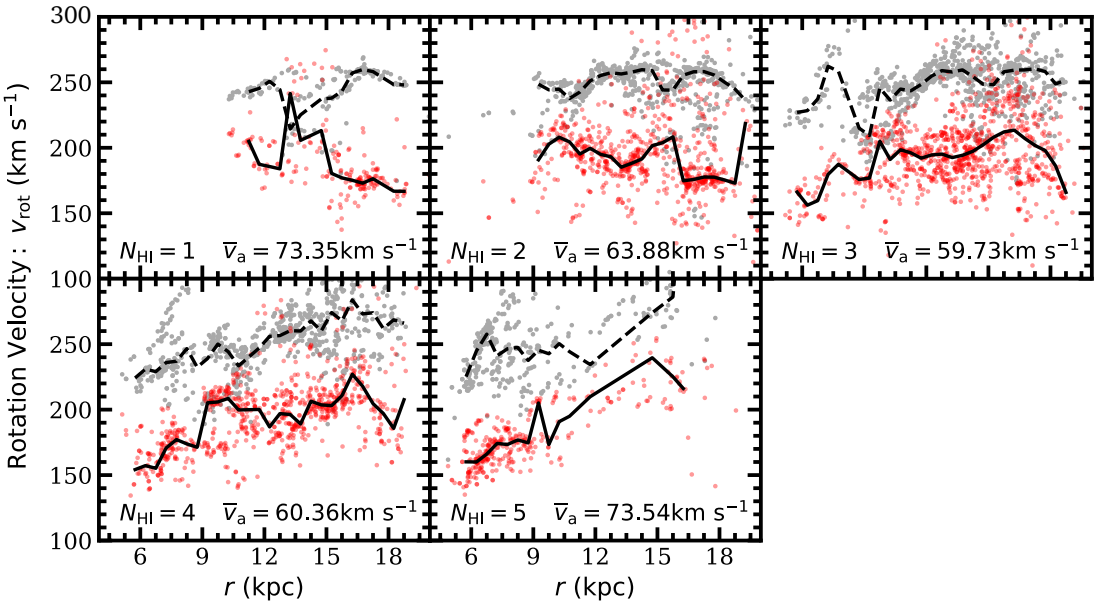

Figure 3.11: RCs for the RGB stars grouped into subsamples based on the number of peaks in the HI spectrum along the corresponding sightlines. The number of peaks range from one to five. The red points represent the star velocities and the gray, the HI. The lines represent the median rotation velocity for a 0.5 kpc bin. The solid line is for the stars and the dashed the gas. Each panel gives the median AD. There is a clear lack of stars that correspond to a line of sight with one peak in the HI spectrum in the inner disk region. This region is well populated by stars along sightlines with five peaks in the HI spectrum, indicating that the inner 10 kpc of the HI disk is messier than the outer radii. The stars still lag behind the gas for each subsample regardless of the number of components in the HI spectrum at that line of sight.

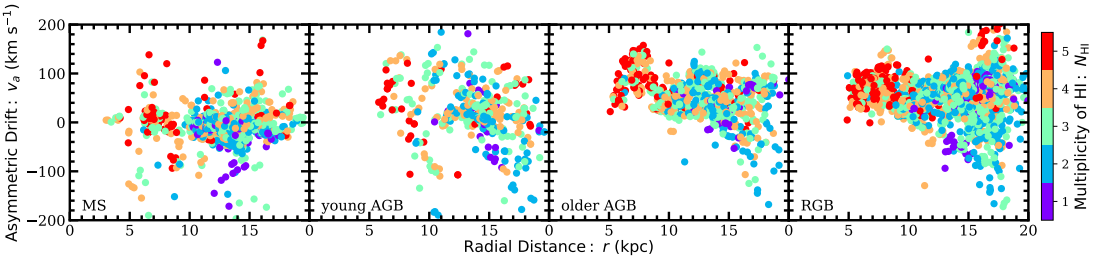

Figure 3.12: AD as a function of radius. The color is the number of peaks in the HI spectrum. The purple points represent sightlines that have one peak in the HI spectrum, blue represents those that have two peaks, green represents three peaks, orange represents four peaks, and red represents five peaks. From left to right: the massive MS stars, the young AGB stars, the older AGB stars, and the RGB stars. The range of AD increases at outer radii for the older three populations.

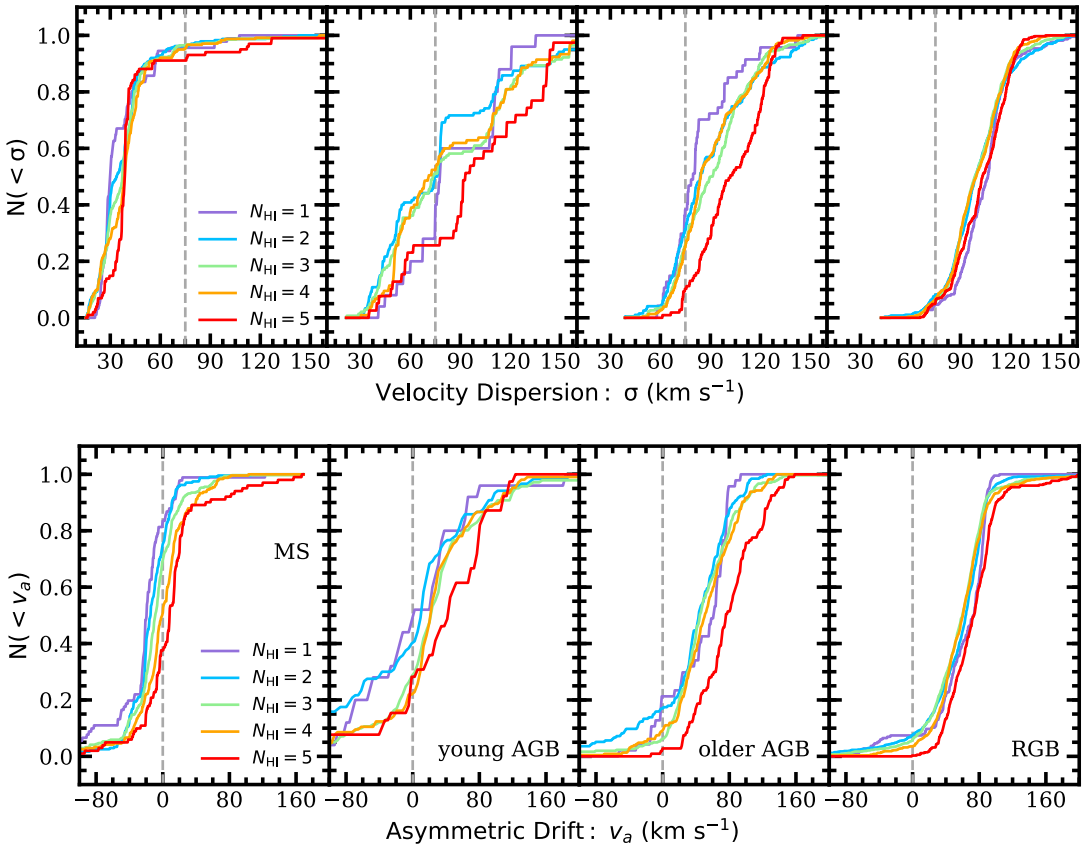

Figure 3.13: Cumulative histograms for velocity dispersion (upper panels) and AD (lower panels) for subsamples based on the number of peaks in the HI spectrum along the corresponding sightlines. From left to right: massive MS stars, young AGB stars, older AGB stars, and RGB stars. The purple line represents sightlines that have one peak in the HI spectrum, blue represents those that have two peaks, green represents three peaks, orange four peaks, and red represents five peaks. The vertical dotted line marks σ = 75 km s^{-1} and v_a = 0 km s^{-1} for reference. Stars along sightlines with five components in the HI spectrum have greater velocity dispersion and AD than those with fewer components. Despite the number of peaks in the HI spectrum, longer lived stars have greater velocity dispersion and AD.

3.5 Conclusion

In this study:

- We use observations from the PHAT and SPLASH surveys of M31 along with 21-cm line measurements to compare the stellar rotation velocities of $\sim 6,000$ stars, which we divide into four aged populations based on color (30 Myr, 0.4 Gyr, 2 Gyr, and 4 Gyr), to the rotation velocities of two gas components (CO and HI).

- We show that AD is a function of stellar age: the youngest stars lead the HI and the longer lived populations lag behind the gas. The lag between the stars and the gas increases monotonically across each age bin, which suggests M31 has experienced continuous heating events. The median AD values for each stellar population with respect to the HI are $-8.15,\ 17.69,\ 50.43,$ and 62.97.

- We present substructure in the RCs and explore possible sources: geometrical effects and multiplicity in the HI spectrum. A significant portion of the scatter in the RCs is caused by a geometrical effect of the tilted ring model that is used to deproject line-of-sight velocity into a rotation velocity. This demonstrates that the tilted ring model is not sufficient to describe the multiple warps in the disk of M31. Despite the limitations this puts on our ability to perfectly model the disk and its dynamics, we show that the underlying trend of monotonically increasing AD with stellar age is a true phenomenon.

3.6 Appendix

3.6.1 The Multiplicity of the HI spectrum

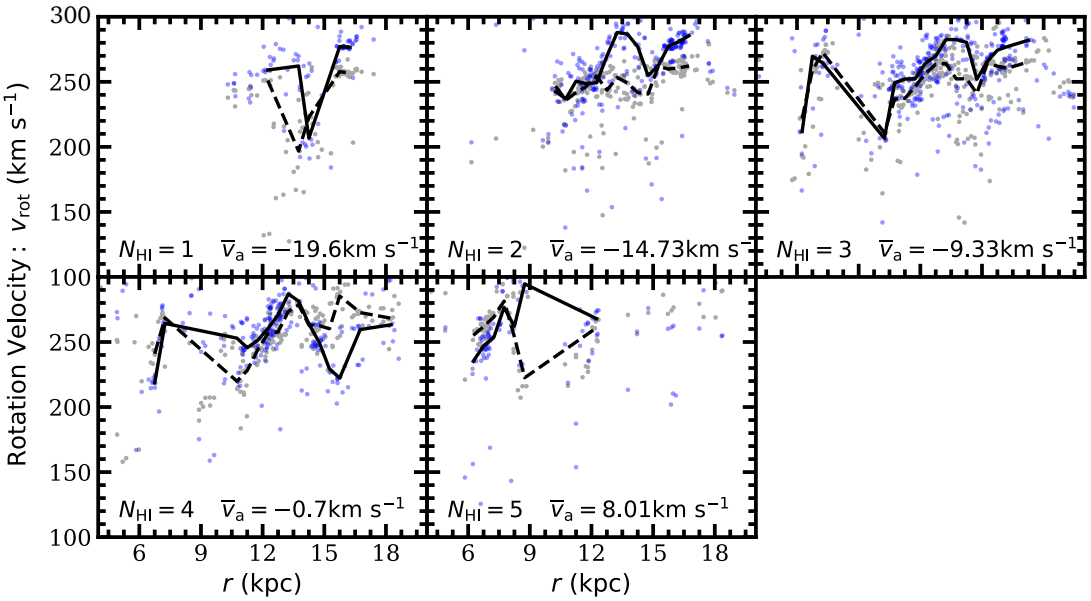

Figure 3.14: Same as Figure 3.11, except the blue points represent massive MS star velocities and the gray points the HI. The median lines are only drawn over regions that contain at least five stars per 0.5 kpc bin.

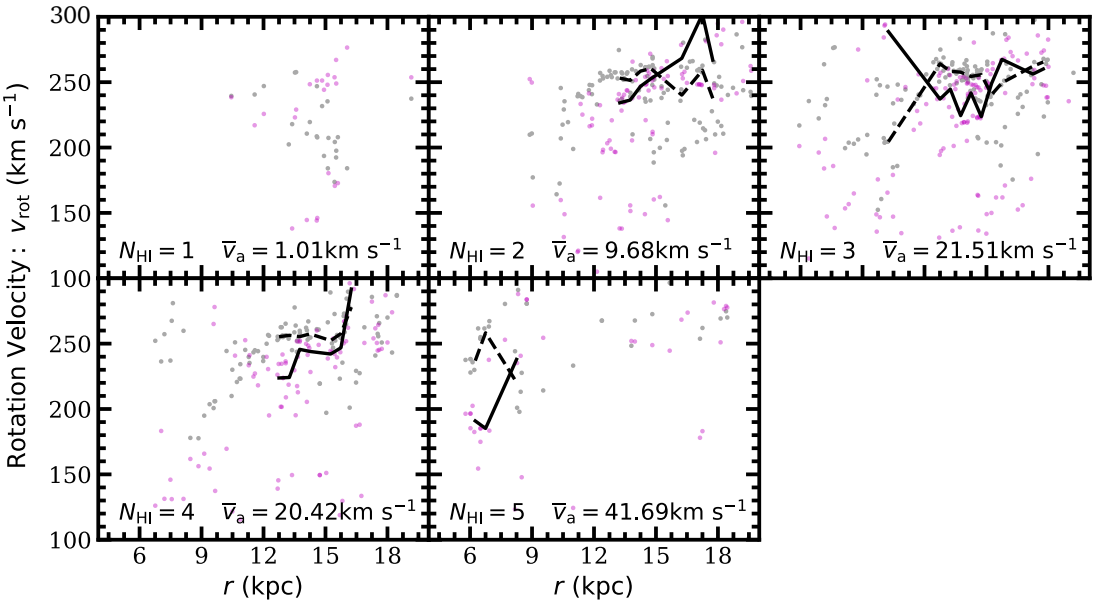

Figure 3.15: Same as Figure 3.11, except the purple points represent intermediate mass young AGB star velocities and the gray points the HI. The median lines are only drawn over regions that contain at least five stars per 0.5 kpc bin.

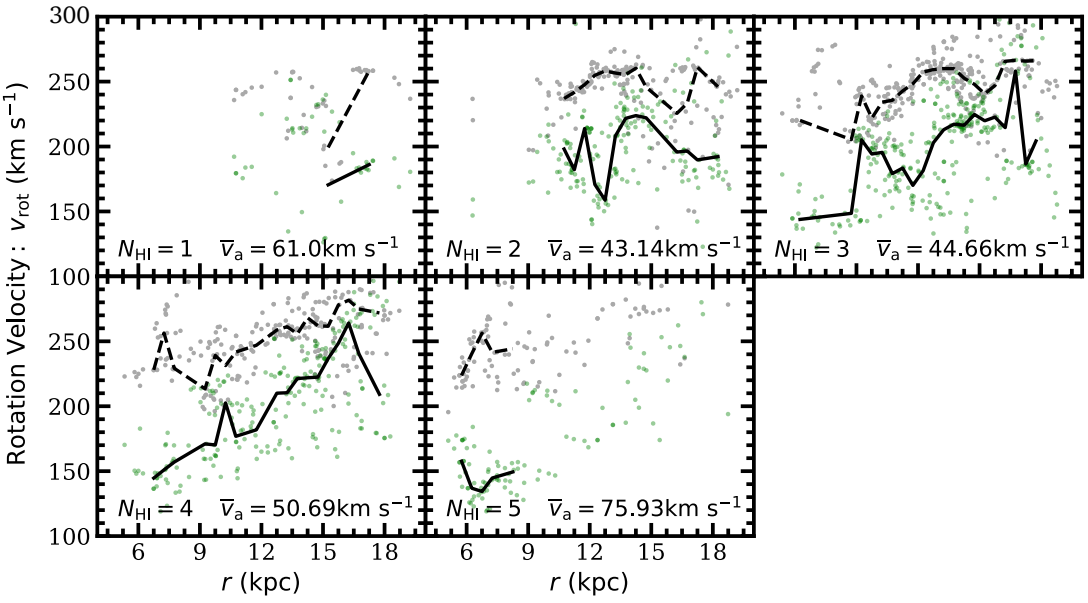

Figure 3.16: Same as Figure 3.11, except the green points represent intermediate mass older AGB star velocities and the gray points the HI. The median lines are only drawn over regions that contain at least five stars per 0.5 kpc bin.

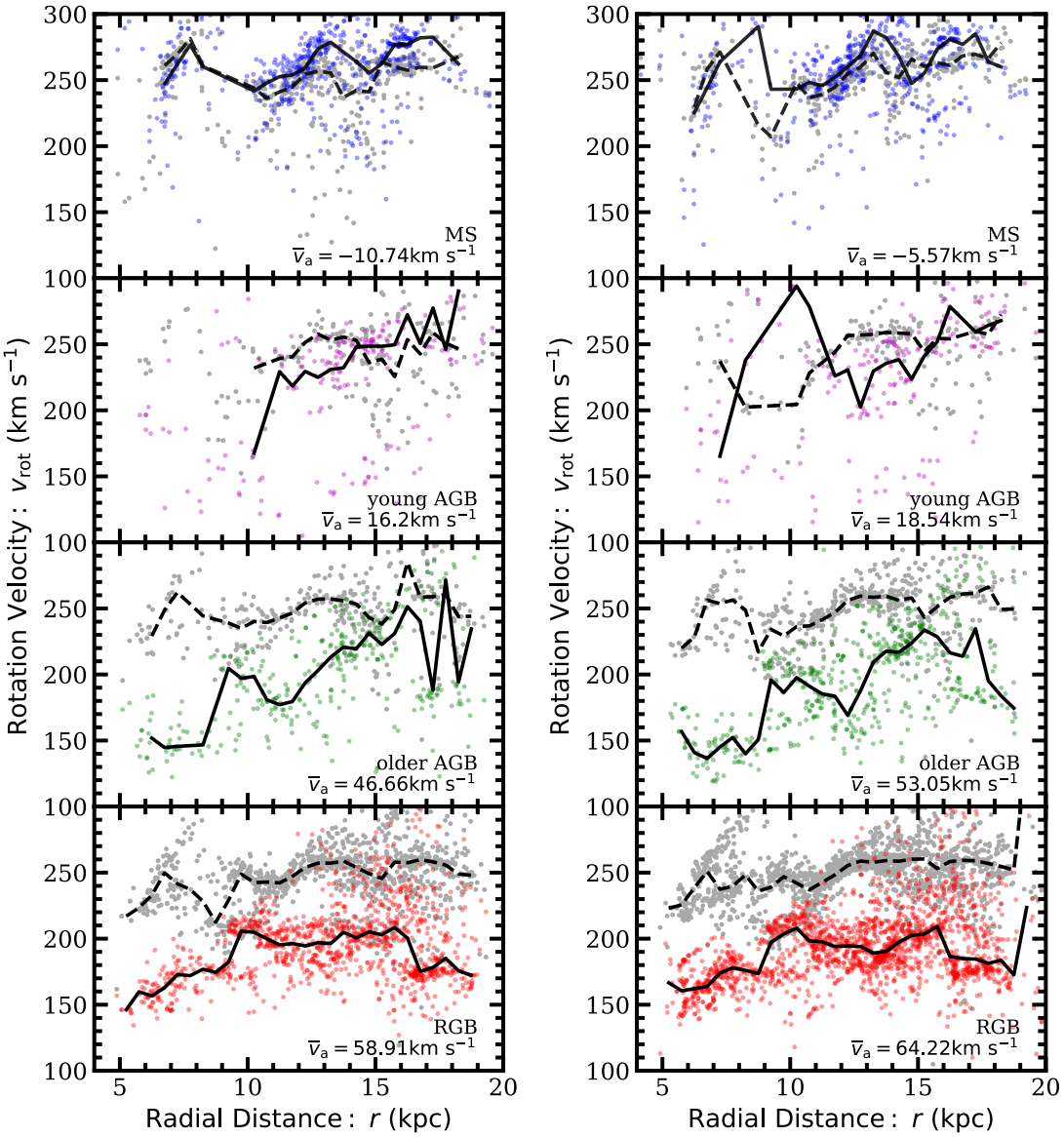

Figure 3.17: Left panel: the RCs for sightlines in which the strongest HI component is also the peak associated with the velocity closest to that of the star. The right panel is the RCs for sightlines where this is not the case. From top to bottom: massive MS stars, young AGB stars, older AGB stars, and RGB stars. The color points represent the star velocities and the gray the HI. The lines represent the median rotation velocity for a 0.5 kpc bin. The solid line is for the stars and the dashed the gas. Each panel gives the median AD. There is a significant amount of scatter and substructure in both the left and right panels, and both show similar trends of increasing AD with stellar age.

3.6.2 Effects of Dusty Sightlines

Next we examine the effects of dust on the substructure in the RCs. Dust extinction biases us to observe more stars on the near side of the dust disk. Because of warps in M31 and patchiness in the dust layer, the radial location of the near side stars changes drastically as you move across the disk.

Figure 3.18 shows extinction maps for the sightlines in our study, as measured by Dalcanton et al. (2015). The median extinction value across the disk is $A_v = 1.6$. Figure 3.19 shows the cumulative fraction of stars at each extinction value. The vertical line denotes an extinction value of 1, which is later used in Figure 3.21 to divide the population into clear and dusty sightlines. A larger of fraction of MS stars have a higher extinction than the other three age bins, which is consistent with the idea that stars form in dusty regions.

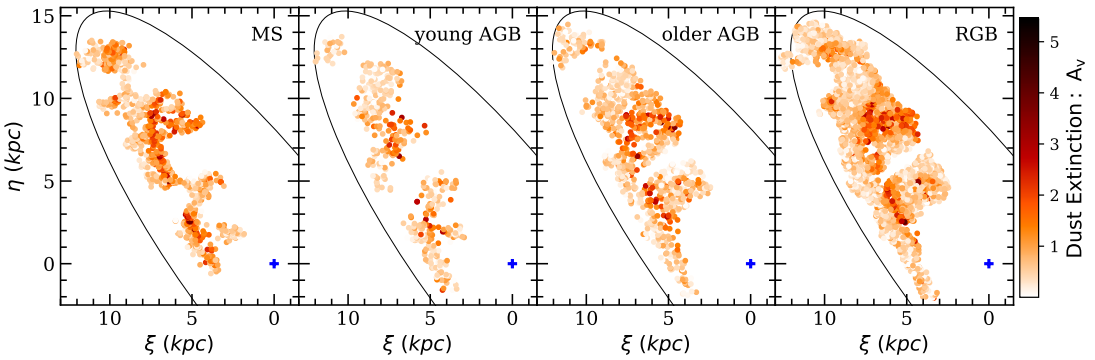

Figure 3.18: Dust extinction maps for the four age bins. Left to right: massive MS stars, young AGB stars, older AGB stars, and RGB stars. Color represents extinction values as measured in Dalcanton et al. (2015). The center of M31 is marked with the blue plus symbol in each panel. The ellipse is for visual reference.

Figure 3.20 shows dust extinction against velocity dispersion and AD. Lower

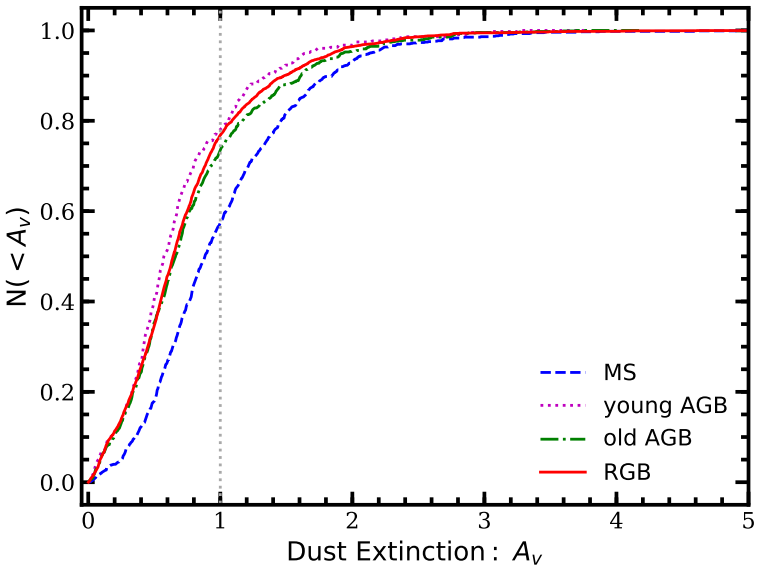

Figure 3.19: Cumulative extinction values for each age bin. The MS stars are represented by the dashed blue line, the young AGB stars by the dotted purple line, the older AGB stars by the dashed dotted green line, and the RGB stars by the solid red line. An extinction value of $A_v = 1$ is denoted by the dotted line. This will be referenced in Figure 3.21. The massive MS stars have the highest fraction of stars with $A_v > 1$.

velocity dispersion is expected in areas of high extinction because in these areas, a smaller number of stars in front of the dust disk are sampled instead of probing stars both in front and behind the dust layer. However, as seen in Figure 3.20, there are too few stars at high extinction to see if there are correlations between the dust extinction, dispersion, and lag. There appear to be no trends amongst these values at lower extinction, which suggests this study is not significantly affected by dust extinction. Figure 3.21 shows RCs for clear ($A_v < 1$) and dusty ($A_v \geq 1$) sightlines. Most of the sightlines, correspond to the stars in our sample have $A_v < 1$. There appears to be no systematic difference in the AD between $A_v < 1$ and $A_v > 1$ sightlines for a given

stellar subsample. There is a hint that the RC scatter is slightly smaller for the $A_v > 1$ sightlines. While it may be tempting to interpret this lower RC scatter as the result of viewing only the near side of the stellar disk, we point out two caveats: (1) the young MS stars have a low AD and are presumably in a thin disk but nevertheless display this lower RC scatter for $A_v > 1$ sightlines, and (2) the HI, which is unaffected by dust extinction, also shows lower RC scatter for $A_v > 1$ sightlines. Instead, it is possible that the reddened sightlines happen to correspond to parts of the stellar and gas disk that have slightly more ordered kinematics than average. However, the analysis in this section is limited to examining dusty and clear sightlines and is unable to test if an individual star is behind or in front of the dust.

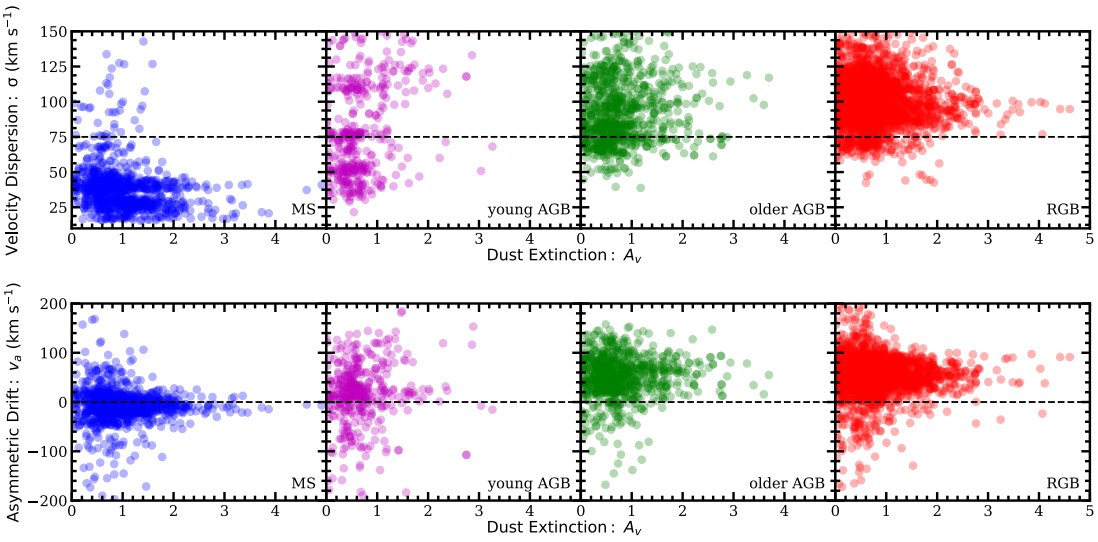

Figure 3.20: Top panel: the velocity dispersion as a function as extinction;. The bottom panel is AD as a function of extinction. Left to right: massive MS stars, young AGB stars, older AGB stars, and RGB stars. The horizontal dotted line marks $\sigma = 75$ km s^{-1} and $v_a = 0$ km s^{-1} for reference. There do not appear to be trends between extinction and velocity dispersion (or AD) at low extinction, and there are too few stars at high extinction make conclusions about correlations.

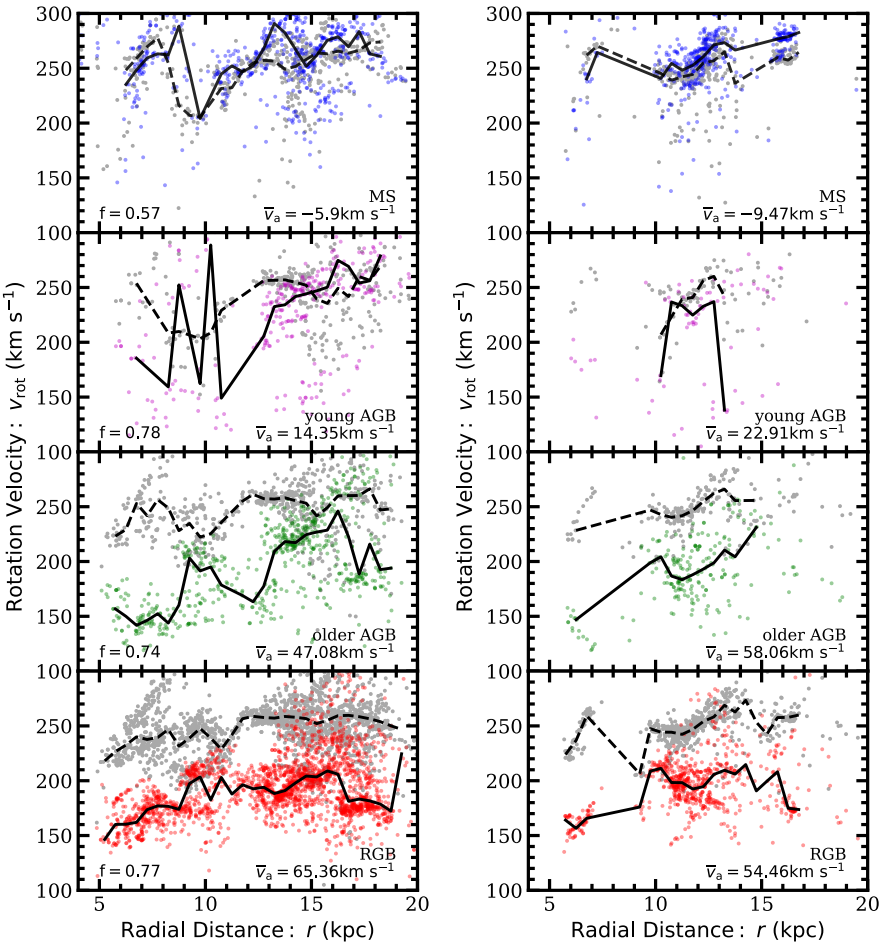

Figure 3.21: Left panel: the RCs for sightlines where the $A_v < 1$. The fraction of total stars for the age bin with $A_v < 1$ are written in the left panels. The right panel is the RCs for sightlines where $A_v \geq 1$. From top to bottom: massive MS stars, young AGB stars, older AGB stars, and RGB stars. In each panel, the gray points represent the HI and the color points represent the stars. The lines represent the median rotation velocity for a 0.5 kpc bin. The solid line represents the stars, and the dashed represents the gas. The median lines are only drawn over regions that contain at least five stars per bin. Each panel gives the median AD. Both sets of RCs show the trend of increasing AD as a function of stellar age.

3.6.3 Contamination from Reddened Young Hot Stars

In the analysis done in the previous section, we are limited to clear or dusty sightlines instead of examining the reddening of individual stars, which would be ideal.

Knowing if a star has been reddened can clarify potential discrepancies: for example, young hot stars that are behind dust will appear redder and as a result can be misclassified as older stars, and thus the higher velocity dispersion seen in the RGB bin in Figure 3.3 could be an artifact of a small population of younger stars in the RGB population.

While we cannot know the reddening of all of the stars in this study, the RGB population can be more closely examined. Dalcanton et al. (2015) analyze a near-infrared CMD of RGB stars in M31 to look for evidence that an individual star has been reddened. We use the same unreddened line from their study to determine if RGB stars in our sample have experienced reddening and therefore could be a mislabeled younger star. Figure 3.22 shows the CMD for the RGB star population using the F110W and F160W HST filters (corresponding to J and H). Most stars lie on the solid line, which denotes unreddened stars. We split the CMD into three regions, as shown in Figure 3.22. Region I is most likely to contain stars that have been reddened and therefore could be misclassified young hot stars, and Region III is least likely to have reddened stars.

Figure 3.23 shows characteristics of the the three regions, as denoted in Figure 3.22. The left panel of Figure 3.23 shows the extinction values in each of the regions. Region I has a bimodal line of sight extinction distribution: the secondary peak is at a higher extinction than that of the peaks of the other two regions. Younger reddened stars could be occupying this peak. The right panel of Figure 3.23 shows the distribution of AD for each region. The AD for Region I peaks at a lower value than the other two regions. The AD for Region I is significantly greater in magnitude than the AD

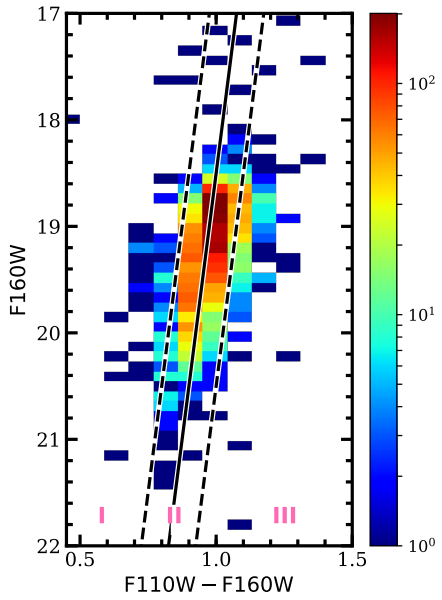

Figure 3.22: The CMD for the RGB stars using the F110W and F160W HST filters (corresponding to J and H). The solid line represents unreddened stars (Dalcanton et al. 2015). Most of the RGB stars sampled are well described by the unreddened line (Region II). Region III contains stars that are least likely to be reddened hot young stars. Points to the far left of the solid line (Region I) could be younger stars that have experienced reddening and were mistakenly classified as RGB stars but could also be metal-poor giants.

for the massive MS population. However, since the peak AD is lower than the median AD for Region II and Region III the median AD of Region I is more similar to the MS population than Region II and Region III. This suggests there could be contamination from younger stars in the sample we have classified as RGB stars.

The RCs for each of the three regions are shown in Figure 3.24. Stars in Region I with $A_v \geq 1$ are marked with a larger square symbol in the top panel. These stars lie in the secondary peak for Region I in the left panel of Figure 3.23 that corresponds to a greater extinction value. The rotational velocities of these stars are

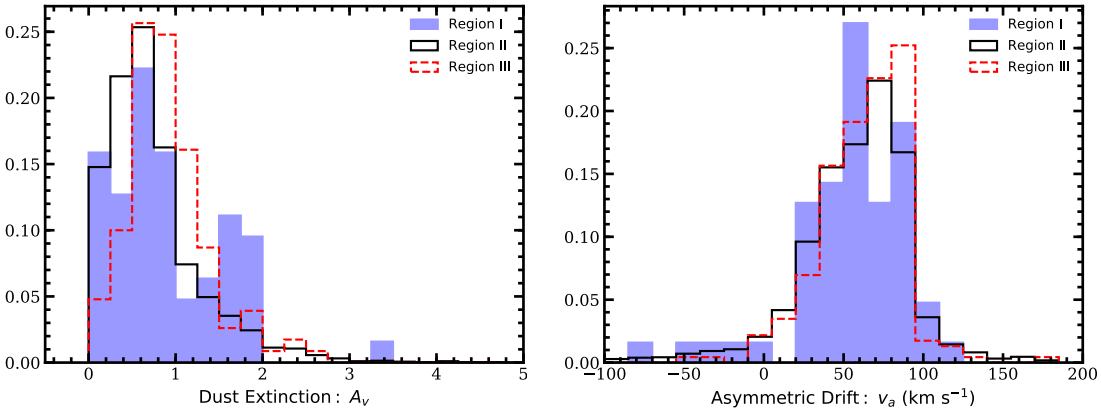

Figure 3.23: Histograms of characteristics for the three RGB CMD regions as denoted in Figure 3.22. Left panel: the line of sight dust extinction values. Right panel: AD. Region I is filled blue histogram, Region II is solid line black histogram, and Region III is the dashed line red histogram. Region I has a secondary peak at high extinction and a smaller magnitude of AD than the other two regions, which suggests it could have reddened young stars.

not significantly different from the velocities of stars in Region I with clear line of sight, Region II, and Region III. They are consistent with the RGB AD: within 2% of the median AD value found for the entire population. Furthermore, they are inconsistent with the behavior of the MS population, as they still lag behind the gas. Thus, while Figure 3.23 suggests there could be young hot stars misclassified as older stars, the RCs suggest these stars are anomalies but not younger stars. There are also so few stars in Region I that are potentially reddened hot young stars compared to the total RGB population (0.39% of the total RGB population) that even if they were young reddened stars, their contamination is insignificant and not a cause of the substructure in the RGB RC.

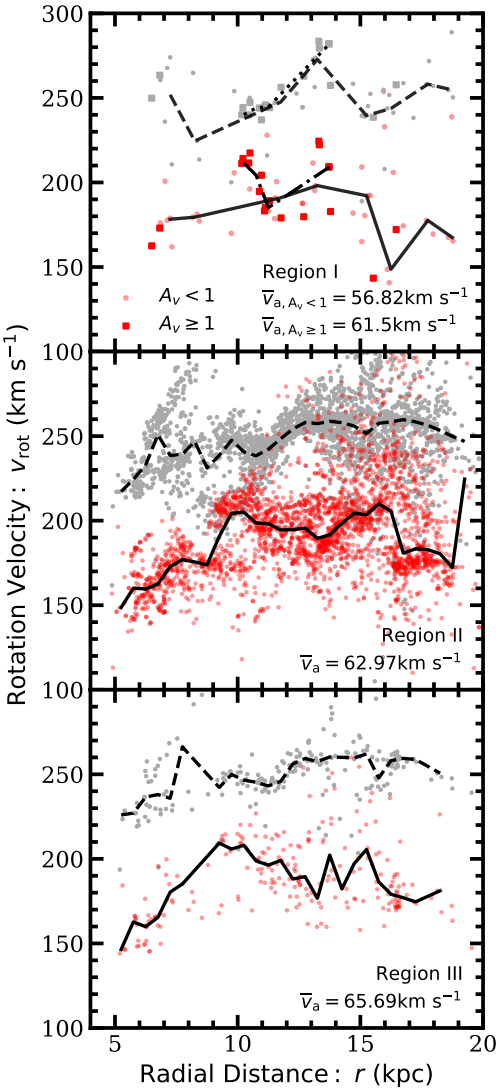

Figure 3.24: RCs for the RGB stars in the three RGB CMD regions as denoted in Figure 3.22. From top panel to bottom: Region I, Region II, and Region III. In each panel, the red points represent the star velocities, and the gray represent the HI. The lines represent the median rotation velocity for a 0.5 kpc bin. In the middle and bottom panels, the solid line is for the stars and the dashed the gas. The median lines are only drawn over regions that contain at least two stars for bin for the top panel and five stars per bin for the second and third panel. In the top panel, the solid line represents the stars in Region 1 with $A_v < 1$, and the dotted dashed line represents the stars in Region 1 with $A_v \geq 1$. The dashed line represents the gas in this region along clear lines of sights, and the dotted line is for the gas along dusty lines of sight. The large square markers in the top panel represent stars in Region I that have $A_v \geq 1$, as seen in the left panel of Figure 3.23, and could be misclassified young hot stars. However, they have an AD value that is consistent with the rest of the RGB population.

Chapter 4

Asymmetric Drift of Andromeda Analogs in the IllustrisTNG Simulation

4.1 Introduction

The kinematics of stars are influenced by dynamical heating events that occur within (i.e., Giant Molecular Clouds (GMCs), spiral arms, bars) or to (i.e., mergers) the galaxies they reside in. Such events are common, are needed to explain the present-day properties of galaxies, and could explain what makes some galaxies unique (e.g. Seth et al. 2005; Walker et al. 1996). Because of their similar masses ($M_{\rm vir} \approx 10^{12}\ M_{\odot}$), the Milky Way (MW) and the Andromeda (M31) galaxies are considered to be analogs of each other (e.g. Patel et al. 2017). However, despite this similarity, the disk kinematics

of the MW and M31 differ drastically. The MW has a population of thin disk stars, while almost all of the disk stars in M31 exist in a thick or kicked up disk (Dorman et al. 2013). These stars are much hotter than classical thin disk stars (Dorman et al. 2013). Additionally, the disk of M31 has a higher velocity dispersion than our own solar neighborhood (Holmberg, J. et al. 2009; Sysoliatina, K. et al. 2018; Dorman et al. 2015; Budanova et al. 2017) and a steeper age-velocity dispersion gradient than the MW (Dorman et al. 2015; Bhattacharya et al. 2019). While it is possible that the MW and M31 formed under different conditions that led to their distinct dynamics, mergers may also explain the higher velocity dispersion observed in M31 (Leaman et al. 2017). As searching for evidence of dynamical heating via internal and external sources is more easily accessible than disentangling different galactic birth conditions, in this study, we aim to understand the impact of external sources of dynamical heating, specifically that caused by mergers, on the observed kinematics of stellar populations in M31.

Mergers lead to the growth of galaxies via the accretion of gaseous and stellar material to the inner and outer regions of galaxies (Abadi et al. 2003); thus they affect not only galactic disks but also the halos of galaxies by perturbing the orbits of stars residing at radial distances of a few to a few hundred kiloparsecs from the center of a galaxy (e.g. Quinn & Goodman 1986). These dynamically heated stars can lead to a kicked-up or puffed up disk, like the one seen in M31 (e.g. Dorman et al. 2013; Purcell et al. 2010). Additionally, simulations show that mergers can heat or accrete stars: these heated or accreted stars can have a permanent increase in velocity dispersion of up to 400% when compared to stars formed in-situ (Walker et al. 1996). Since stars have

long dynamical time scales, they retain these differences (e.g. Abadi et al. 2003; Purcell et al. 2010). In addition to heating existing stars, mergers can play an important role in setting the birth kinematics of stars. Brook et al. (2004) illustrate that stars born in epochs of rapid accretion of gas from hierarchical growth exhibit different and much hotter $z = 0$ kinematics than stars that were born during periods of quiescence. Thus, mergers play an important role both in setting the birth kinematics of stars in a merger event and also heating the kinematics of existing stars.

Because of its relatively close proximity of 785 kpc (McConnachie et al. 2005), we can study the entire disk and halo of M31 using individual, resolved stars and search for evidence of mergers. In the last decade, two major surveys of the M31 region have revealed potential relics of mergers throughout M31's disk and halo. The wide-field Pan-Andromeda Archaeological Survey (PAndAS; Ibata et al. 2007, 2013) has surveyed the halo of M31 to a projected distance of 150 kpc, revealing debris in the form of tidal streams and shelves (e.g. Hernquist & Quinn 1988, 1989; Escala et al. 2019; McConnachie et al. 2018). The most prominent debris feature is the Giant Stellar Stream (GSS) (Ibata et al. 2001, 2005; Ferguson et al. 2002), which spans nearly 100 kpc from the center of M31. The second survey is the Pan-chromatic Hubble Andromeda Treasury (PHAT) (Dalcanton et al. 2012; Williams et al. 2014), which among other discoveries has revealed M31's global star formation history (Lewis et al. 2015; Williams et al. 2017), a ring of star formation at 10 kpc (Lewis et al. 2015), and the age-velocity dispersion relation (Dorman et al. 2013).

As more evidence for a fairly constant and violent merger history for M31 have

emerged, so has the question about the types of mergers that shaped M31 into the galaxy we see today. Until recently, the favored theories for M31's formation history were an ancient major merger followed by a series of minor mergers (e.g. Kormendy et al. 2013; van den Bergh et al. 2006; Courteau et al. 2011). Simulations of minor mergers in M31's halo have successfully recovered many observed features: the simulations from Tanaka et al. (2009) show that roughly 15 minor mergers are necessary to form the stellar debris seen in M31 today, and Fardal et al. (2008) illustrates that a minor merger can recover the formation and velocity dispersion of the GSS as well. Furthermore, the motions of globular clusters at high galactic radii suggest that M31 has had more than one major period of accretion (Mackey et al. 2019). However, new studies suggest that instead of an ancient and larger merger, a relatively recent (∼2-3 Gyr ago) major merger could explain many of these observed phenomenon while preserving the disk of M31 (D'Souza & Bell 2018). For example, Hammer et al. (2018) find a major merger model recovers both the substructure resembling the GSS and the age-velocity dispersion gradient in M31's disk (Dorman et al. 2015). They conclude a major merger can explain the burst of star formation approximately 2 Gyr ago (Williams et al. 2017), a ring of star formation at 10 kpc (Lewis et al. 2015), and the mass of the stellar halo (Ibata et al. 2013; Bell et al. 2017). Thus, while it is believed that M31 has had a long and ongoing history of accretion (e.g. Ferguson & Mackey 2016), the exact merger history is still unknown, and therefore leads to an ongoing debate as to whether or not a single, recent major merger could explain several observed properties in M31's halo and disk better than a series of recent minor mergers.

Hammer et al. (2018) highlight the importance of recovering M31's disk dynamics when testing different merger histories for M31. *In this study, we aim to determine if the relative difference between the stellar dynamics and gas dynamics of the disk of M31 are consistent with a major merger scenario.* To do so, we will analyze the stellar and gas dynamics across a sample of M31 mass analogs selected from a cosmological simulation, accounting for a range of merger histories across a large sample of simulated galaxies, and compare these properties to observed measurements of the lag between the gas rotation velocity and that of the stars, or the asymmetric drift (AD), in the disk of M31 from Quirk et al. (2019). In doing so, we will explore whether AD changes with merger history and thereby determine how significant of a role external dynamical heating has played in the current kinematics of these analogs.

In this study, we are solely limited to exploring the effects of external sources of dynamical heating (i.e. mergers) because the resolution of simulated analogs selected from a cosmological box does not allow us to probe internal sources occurring on sub-kiloparsec scales such as perturbations from spiral waves (e.g. Sellwood & Binney 2002; Sellwood 2014), galactic bars (e.g. Dehnen & Binney 1998; Saha & Elmegreen 2018), or GMCs (e.g. Jenkins & Binney 1990; Ting & Rix 2019). As such, we cannot comment on the effects of these drivers on the disk dynamics of massive galaxies. While internal sources of heating affect a galaxy's kinematics, they cannot alone explain the kinematics observed today. External sources of dynamical heating, mergers, are also necessary to explain some Local Group galaxies' velocities (Leaman et al. 2017). Furthermore, while stellar feedback can drastically affect the disk of galaxies less massive than the MW

or M31 (El-Badry et al. 2016), mergers are more important than stellar feedback for setting the present-day kinematics of massive galaxies. Thus, in this work we focus solely on the effects of external dynamical heating on AD, with the overarching goal of shedding light on the recent merger history of M31.

This paper is organized as follows: in Section 4.2, we discuss the IllustrisTNG simulations and the selection criteria we use to choose our sample of analogs. Section 4.3 describes the methods used to calculate rotation velocities, construct rotation curves, and calculate AD. In Section 4.4, we illustrate how AD as a function of stellar age changes with merger history, and in Section 4.5 we make comparisons to observational results. In Section 4.6, we summarize our findings.

4.2 Data

4.2.1 The Illustris Suite

The IllustrisTNG Project is a suite of N-body and hydrodynamic simulations evolved from redshift $z = 127$ to $z = 0$ using the moving-mesh `AREPO` code (Marinacci et al. 2018; Naiman et al. 2018; Springel et al. 2018; Pillepich et al. 2018; Nelson et al. 2018; Springel 2010). The simulations span a cosmological volume of $(110.7\ \mathrm{Mpc})^3$ and are initialized with the following cosmological parameters from Planck Collaboration et al. (2016): $\Omega_m = 0.3089$, $\Omega_\Lambda = 0.6911$, $\Omega_b = 0.0486$, $\sigma_8 = 0.8159$, $n_s = 0.9667$, and $h = 0.6774$. Throughout our analysis, we adopt a value of $h = 0.704$ (WMAP-9; Hinshaw et al. 2013).

The IllustrisTNG Project (Marinacci et al. 2018; Naiman et al. 2018; Springel

et al. 2018; Pillepich et al. 2018; Nelson et al. 2018) is a follow-up suite of simulations to the original Illustris Project (Nelson et al. 2015; Vogelsberger et al. 2014), including an updated galaxy formation model described in Weinberger et al. (2018) and Pillepich et al. (2018). The most significant improvements to the galaxy formation model include the treatment of AGN feedback, an improved parametrization of galactic winds, and the addition of magnetic fields.

In our analysis, we use data from the IllustrisTNG100-1 simulation (hereafter IllustrisTNG), the midsize and mid-resolution simulation in the suite including both dark matter and baryons. IllustrisTNG follows the evolution of 1820^3 dark matter particles and 1820^3 hydrodynamical cells, achieving a dark matter particle mass resolution of $m_{\rm DM} = 7.5 \times 10^6\ M_\odot$ and a baryonic mass resolution of $m_{\rm bary} = 1.4 \times 10^6\ M_\odot$. Halos and subhalos are identified using the `SUBFIND` (Springel et al. 2001; Dolag et al. 2009) halo-finding routine. We use the IllustrisTNG merger trees created with the `SUBLINK` code (Rodriguez-Gomez et al. 2015) to track the mass history of subhalos in our analysis. In the following sections, we identify a primary sample of M31 analogs in IllustrisTNG.

4.2.2 Selection of M31 Mass Analogs

M31 analogs are chosen as all central (or primary) subhalos at $z = 0$ where the FoF group virial mass is $M_{\rm vir} = 1 - 2.2 \times 10^{12}\ M_\odot$ (see D'Souza & Bell 2018). Virial mass is calculated for each `SUBFIND` FoF group following the methods of Bryan & Norman (1998). We also require that these primary subhalos have a stellar mass within the range $5 - 20 \times 10^{10}\ M_\odot$ (Tamm et al. 2012; Sick et al. 2014). Finally, we require that the maximum circular velocity for each subhalo is at least 200 $km\ s^{-1}$ to ensure

that our analogs generally represent the observed HI rotation curve of M31 (Chemin et al. 2009; Corbelli et al. 2010). Using these selection criteria, we find 216 M31 analogs in IllustrisTNG. We eliminate one analog that has no associated gas, bringing the *full sample* to a total of 215 analogs.

The left panel of Figure 4.1 shows the distribution of virial masses for the full sample (blue histogram) and for the subset of 93 M31 analogs that will serve as the *primary sample* (blue filled histogram). The primary sample is selected based on visual inspection of each simulated galaxy's rotation curve and provides a checkpoint to eliminate any analogs without sufficient statistics to calculate both stellar and gaseous rotation curves (see Section 4.3.3). The middle and right panels show the distribution of stellar mass and maximum circular velocity, respectively, for the full sample of M31 analogs in IllustrisTNG (blue histograms) and the primary sample (blue filled histograms). The gray vertical line in the right panel indicates the maximum circular velocity of M31's HI rotation curve (Corbelli et al. 2010). All three properties of the primary sample are representative of the broader population of M31 analogs.

4.2.3 Stellar Assembly for IllustrisTNG Analogs

Our main goal is to explore if the merger history of galaxies in our simulated sample show any correlation with the values of AD. As such, the stellar assembly and merger history catalogs for the IllustrisTNG suite are also used to probe the formation histories of the M31 analogs identified in Section 4.2.2. The stellar assembly and merger histories of the original Illustris-1 simulated galaxies are discussed in Rodriguez-Gomez et al. (2015); Rodriguez-Gomez (2016); Rodriguez-Gomez et al. (2016). The same tools

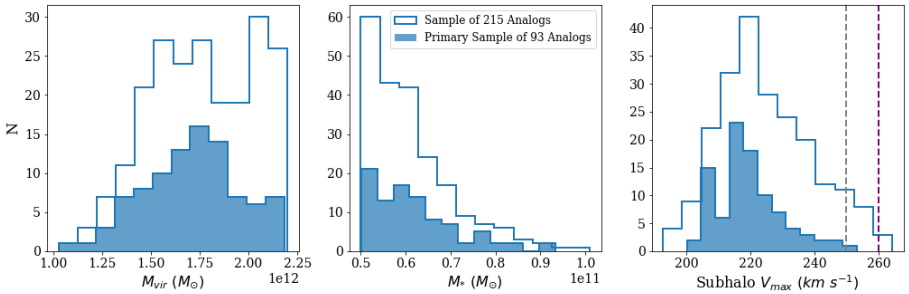

Figure 4.1: Histograms of virial mass (left), stellar mass (middle), and subhalo v_{max} for all M31 mass analogs. In all panels, the blue histogram represents the full sample of 215 analogs, and the blue filled histogram represents our primary sample of 93 analogs that are chosen based on visual inspection of their radially average rotation curves (see Section 4.3.3). In the right panel, the gray vertical dashed line denotes the peak circular velocity of M31 as measured in Corbelli et al. (2010) and the purple dashed line represents the approximate peak circular velocity of both halves of M31's disk in Chemin et al. (2009). Our primary sample is generally representative of the full sample of M31 analogs in all properties.

were used to create the equivalent catalogs for IllustrisTNG. Below, we describe the properties of interest for this analysis and their definitions as defined by the previously mentioned papers.

- time of last major merger: the lookback time at which the last major merger (stellar mass ratio $<$ 4:1) occurred
- total number of major mergers: the total number of completed major mergers (stellar mass ratio $<$ 4:1)
- total number of minor mergers: the total number of completed minor mergers (stellar mass ratio $>$ 10:1 and $<$ 4:1)

Figure 4.2 shows the distribution of the time of last major merger for the 215 M31 analogs in our primary sample. The median time of last major merger is 8 Gyr

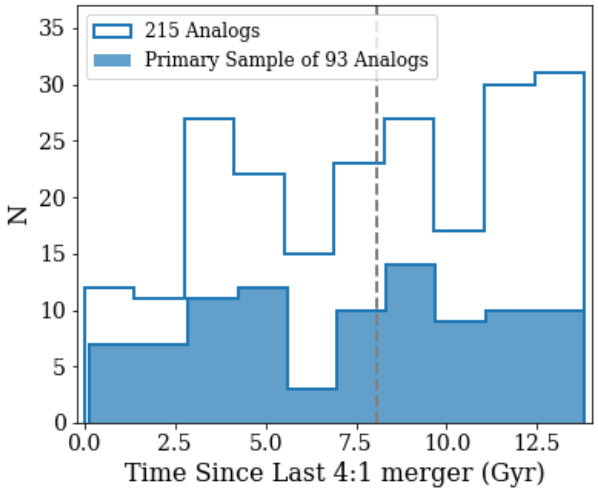

Figure 4.2: Histograms of time since an analog's most recent 4:1 merger. The blue histogram represents the full sample of 215 analogs, and the blue filled histogram represents our primary sample of 93 analogs. The vertical line marks the median time for the primary sample at 8.0 Gyr. Our primary sample is generally representative of the broader distribution of M31 analogs.

ago as denoted by the vertical dashed gray line, thus many analogs have had relatively quiet recent merger histories.

Figure 4.3 illustrates the total number of mergers (major and minor) for the primary sample in black. The distribution of total 4:1 mergers is indicated by the blue filled histogram and the total number of 10:1 mergers is represented by the red histogram. On average, M31 analogs in our primary sample experience 5-10 mergers in total. In total, the primary sample experiences 441 4:1 mergers, 369 10:1 mergers, summing to 810 mergers overall.

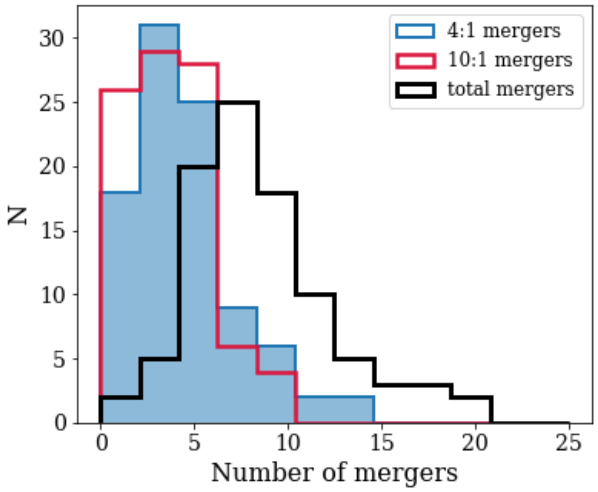

Figure 4.3: Histograms of number of mergers for the analogs in the primary sample. The blue filled histogram shows the distribution of number of 4:1 mergers, the red histogram represents the number of 10:1 mergers, and the black histogram represents the total number of mergers.

4.3 Methods

AD is often defined as the difference between the circular velocity derived from the potential and the stellar rotation velocity (Strömberg 1946). For the purposes of comparing this work to Quirk et al. (2019), we define AD slightly differently than Strömberg (1946) and Walker et al. (1996). Instead of relying on models of the potential to calculate circular velocity, we use the rotation velocity of the gas data to calculate AD, as in Quirk et al. (2019), since this gives a more empirical measurement.

The rotation velocity of the gas is used as a proxy for circular velocity because gas is collisional and therefore can easily dissipate energy and maintain a low energy orbit (Sellwood & Moore 1998). Gas creates radial pressure support, which in low mass disks can cause the tangential velocity of the gas to fall below its circular velocity;

however this is not the case for massive disks like M31 (Dalcanton & Stilp 2010). Stars, on the other hand, are not collisional and thus can maintain an eccentric orbit if they are gravitationally perturbed. When comparing their circular rotation velocities, stars may lag behind gas because they are following a different orbital path and/or moving more slowly.

In this sense, AD is a measurement of the difference between a star's orbit and a roughly circular orbit, as the gas is only a proxy for circular velocity. Thus, it can also be treated as a long-term effect of dynamical heating. Since the perturbations from dynamical heating can permanently alter the orbital paths of stars (e.g. Leaman et al. 2017), it can change a star's angular momentum such that random motions are increased in a stellar population, and thus the group's average motion is less dominated by orderly rotation (Sellwood & Binney 2002). Effects of dynamical heating may be long lasting, and individual stars in galaxies often preserve the effects of heating. Walker et al. (1996) find that minor mergers temporarily increase AD in a galaxy using idealized N-body simulations.

In this work, we will focus on the effect of external dynamical heating, and specifically that caused by 4:1 major mergers for a cosmological sample of M31 mass analogs. Where possible, we will make comparisons to existing AD measurements in M31, as this is the only galaxy for which observational results of AD as a function of stellar age are available (Quirk et al. 2019). In our own galaxy, AD has been used to construct rotation curves beyond the solar neighborhood and to correct the local standard of rest (LSR) (Golubov 2014; Huang et al. 2016) but has not been studied as

a function of age or for individual stars.

4.3.1 Rotating the Coordinates

To calculate rotation curves and subsequently AD, we first apply a center of mass (COM) shift and rotate the particles/cells in each simulated M31 analog to a face-on reference frame. IllustrisTNG particle/cell positions and velocities are reported relative to the simulation box edges, so we first shift the data to a (0,0,0) Cartesian reference frame by subtracting the COM of the dark matter halo from both the stellar and gaseous data. This COM position comes directly from the IllustrisTNG group catalogs (i.e. the position of each FoF group). We have checked whether using the center of mass of the baryons rather than the dark matter alters the results and find no significant differences.

To rotate the particle/cell data to a face-on reference frame, we calculate the net specific angular momentum vector for all gas cells belonging to a given halo. Then we apply a rotation matrix to the cell data such that the unit vector of the net angular momentum of the gas is mapped to the z-axis in the face-on reference frame. The same procedure is repeated with all star particles belonging to a given halo. Thus, the stars and gas are each rotated with respect to their own net angular momenta. In this new reference frame, the galaxy's disk lies in the xy-plane. Finally, particles with a z scale-height > 10 kpc are eliminated to ensure we only include data for the gas and stars roughly in the disks to construct rotation curves and subsequently AD.

4.3.2 Smoothing the Particles/Cells

Once the particles/cells are rotated to the face-on reference frame, we divide the stellar particles into four broad age groups: Group 1 with ages < 1 Gyr, Group 2 with ages $1 - 5$ Gyr, Group 3 with ages $5 - 10$ Gyr, and Group 4 with ages > 10 Gyr. These age bins differ from those used in the observational analysis of AD in M31 in Quirk et al. (2019) in order to take advantage of the full range of stellar particle ages that exists in the IllustrisTNG simulation. The observational constraints on M31 in Quirk et al. (2019) are limited to stellar ages of up to $\sim$4 Gyr, as older stars are too faint to observe easily. IllustrisTNG, on the other hand, provides ages spanning approximately a Hubble time. However, there is a lack of young (< 500 Myr) stars in IllustrisTNG, which prevents us from breaking Group 1 into age bins that better match the observational results in M31. This lack of young stars may be a result of the AGN feedback model in IllustrisTNG (Weinberger et al. 2018; Terrazas et al. 2020).

Quirk et al. (2019) calculates AD of stars with respect to neutral HI gas. To follow this, we also calculate AD with respect to neutral gas data in this analysis. With the IllustrisTNG simulated galaxies, we implement this by limiting our analysis to only include the gas data where the neutral hydrogen fraction, n_H, is above some threshold. Since there is no exact boundary for what gas constitutes as neutral, we initially varied the neutral fraction cutoffs to find the highest fraction that still included enough gas cells for good statistics and to have a full spatial expanse across the inner 20 kpc of each analog. We find that $n_H > 0.6$ is a reasonable threshold, as on average $21.1 \pm 11\%$ of gas particles fall into this range for the primary sample.

After the stellar particles are divided into the four age groups and the neutral gas cells are isolated, we locally smooth the line-of-sight velocity (the vertical component or V_z in the face-on reference frame). Instead of smoothing velocities using a grid of set positions, we use the true positions of all particles/cells in a given M31 analog and center a smoothing circle on each particle/cell, as in Dorman et al. (2015) and Quirk et al. (2019).For stellar age Groups 2 and 3, we use a circle of radius 0.75 kpc and a circle of 1.05 kpc for the less populated Groups 1 and 4 and for the neutral gas cells. This radius size mimics the 200 ″-275 ″resolution in HI observations in M31, described in Quirk et al. (2019). The size of the circle was optimized to probe local kinematics and to include enough data points for good statistics. If there are at least 10 particles/cells in a circle, we assign the median of the velocity components to that particle/cell. We use these median components to calculate a rotation velocity and assign it to the position of the particle/cell that the circle is centered on. If there are not 10 members in a particle's/cell's smoothing circle, we do not calculate a rotation velocity at that position. That particle/cell may still be included in the membership of nearby circles and thus would contribute towards the calculation of the median velocities at other positions if those circles pass the membership requirement. We also experimented with adjusting circle membership requirements to balance retaining data with being able to smooth the data. Similar to Quirk et al. (2019), we chose a membership requirement of 10.

To ensure that our smoothing does not obscure any substructures in the rotation curves and subsequent bias to AD, we created rotation curves with and without the smoothing and find no significant differences. We illustrate the smoothing process

for an example halo in our primary sample in Section 4.3.5.

4.3.3 Calculation of Rotation Curve

For the rest of our analysis, we use the smoothed kinematics for the primary sample of M31 analogs. We calculate a rotation velocity for every star particle and gas cell that passes the circle-membership requirement in the smoothing process. To calculate the rotation velocity, we find the tangential velocity of the particles/cells by first calculating the projected radial velocity and the total planar velocity, shown in the equations below. We limit our rotation velocity calculations to the 2D xy plane in our face-on rotated frame so the resulting rotation velocities are comparable to de-projected rotation velocities in observations (Quirk et al. 2019).

$$v_{rad} = \frac{x \cdot v_x + y \cdot v_y}{\sqrt{x^2 + y^2}} \tag{4.1}$$

$$v_{tot} = \sqrt{v_x^2 + v_y^2} \tag{4.2}$$

$$v_{rot} = v_{tan} = \sqrt{v_{tot}^2 - v_{rad}^2} \tag{4.3}$$

The above procedure gives us a rotation velocity for every smoothed star particle and neutral gas cell. To calculate AD we must be able to directly compare the rotation velocity of the star particles and neutral gas cells. However, the gas cells and star particles do not have the same spatial extent and analogs typically have an unequal

number of stellar particles and gas cells. Instead of trying to pair each star particle to a neutral gas cell as in Quirk et al. (2019), we radially bin all of the particles/cells and calculate the median rotation velocity within that bin. Our radial bins sample from 2 kpc to 20 kpc with a spacing of 0.1 kpc. We radially bin in this fashion separately for each stellar age bin and also for the neutral gas cells. As seen in the bottom panel of Figure 4.5, there is no clear azimuthal dependence of the rotation velocity, so we do not obscure any local substructure through this binning.

4.3.4 Visual Inspection of Rotation Curves

Since both the gas cells and star particles of these M31 analogs are necessary to calculate AD, we perform an additional visual inspection of the rotation curves of each analog in the full sample to ensure they have enough spatially overlapping stellar particles and gas cells across the inner 20 kpc of the analog. Those that do not have spatial overlap between the gas cells and star particles for at least five radial bins are removed. After this visual inspection, 93/215 M31 analogs from IllustrisTNG remain and will be referred to as the *primary sample*.

4.3.5 Demonstrating Smoothing Particle/Cell Data

In this section, we choose an analog from the primary sample that best represents M31's rotation curve to demonstrate smoothing the particle/cell data prior to calculating rotation curves. The halo properties of this example analog are listed in Table 4.1, and the mock image of this simulated galaxy is shown in Fig 4.4 (Torrey et al. 2015; Rodriguez-Gomez et al. 2019). The results of velocity smoothing (described

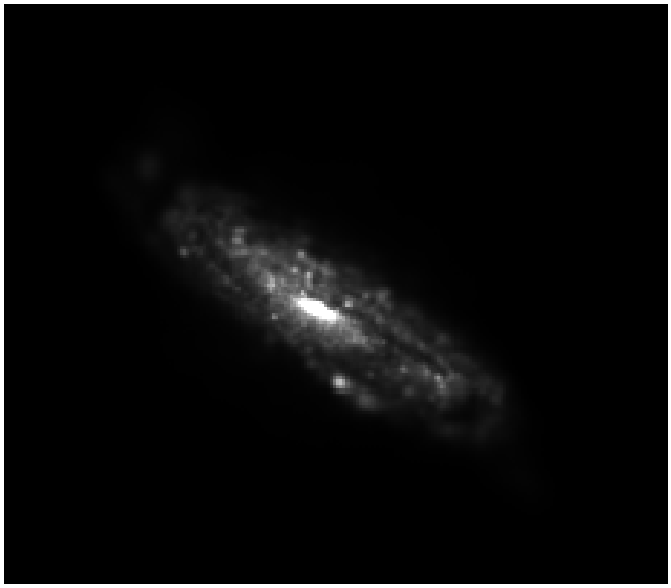

Figure 4.4: Mock image of analog 449972 as if viewed with the Sloan Digital Sky Survey (SDSS) g filter.

in Section 4.3.5) for this analog is illustrated in Figure 4.5, which shows the individual line-of-sight velocity, the post-smoothing median line-of-sight velocity, and the rotation velocity of each star particle for the four age bins as a function of position. For this analog, 16088 of the original 19919 central neutral gas cells remain after the smoothing process, and 77832 of the 87141 central star particles remain. This is typical of M31 analogs in the primary sample. The smoothed kinematic data retains the underlying kinematics needed to calculate AD without strong loss of information, so we continue to smooth the data for the entire primary sample.

4.3.6 Calculation of AD as a function of Stellar Age

AD, (also denoted by v_a), is the difference between the rotation velocity of the gas and that of the stars.

Table 4.1: Analog 449972 Halo Properties

$M_{\rm vir}$	$2.01 \times 10^{12}\ M_\odot$
$M_\star$	$9.08 \times 10^{10}\ M_\odot$
$V_{\rm max}$	247 km s^{-1}
Time Since Last 4:1 Merger	4.12 Gyr
Number of 4:1 Mergers	4
Number of 10:1 Mergers	5

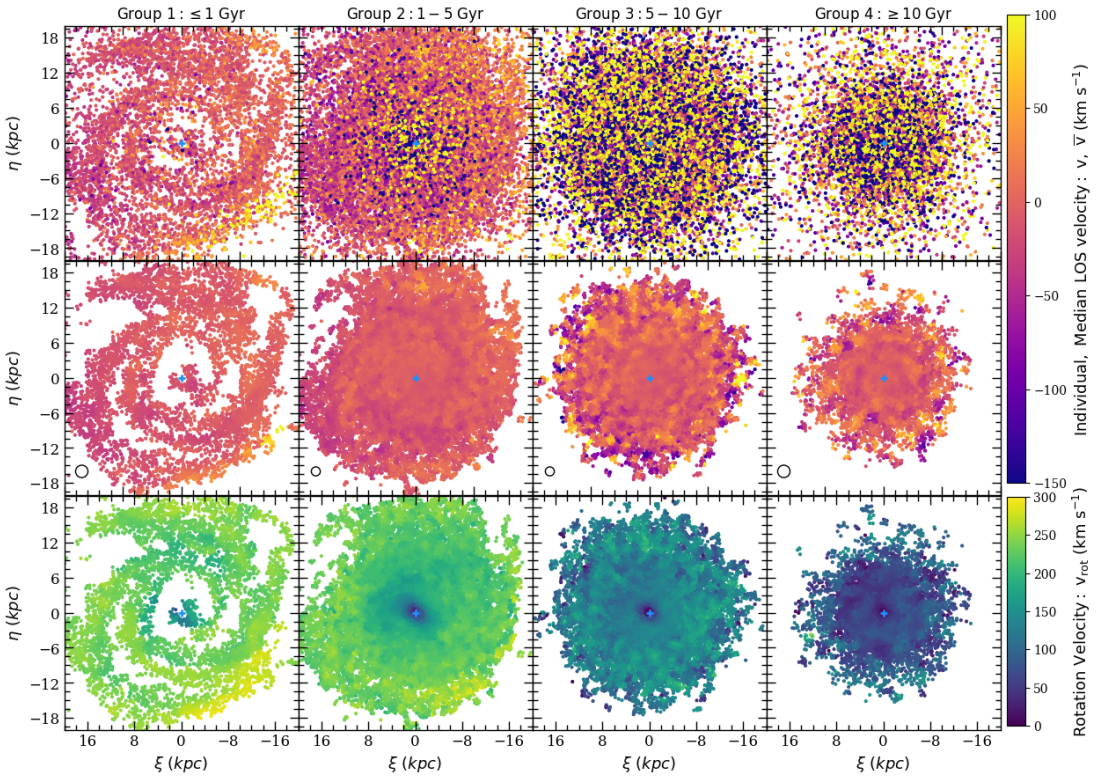

Figure 4.5: Individual line-of-sight velocity (top row), local medians of the line-of-sight velocity (middle row), and rotation velocity (bottom row) as a function of location and age for star particles in analog 449972. From left to right: age < 1 Gyr, age $1 - 5$ Gyr, age $5 - 10$ Gyr, and age > 10 Gyr. Smoothing circles are used to calculate the median of the individual line-of-sight velocities. We use a circle of radius 0.75 kpc for Groups 2 and 3 and 1.05 kpc for the less populated Groups 1 and 4. The circles in each panel of the middle row show the respective sizes of the smoothing circles. The blue cross marks the center of the analog.

$$v_a = v_{\rm rot,gas} - v_{\rm rot,\star} \tag{4.4}$$

We calculate the AD at each radial bin for the four stellar age groups individually. Thus at each radial bin, we have an AD measurement for Group 1, 2, 3, and 4 with respect to the same neutral gas cell rotation velocities. An example of the results of the AD calculations from the corresponding rotation curve are presented in Figure 4.6. The left panel shows the rotation curve for this analog: the neutral gas is represented by the grey points, the blue triangles represent stars with ages < 1 Gyr, the purple points represent stars between $1 - 5$ Gyr, the green squares represent stars between $5 - 10$ Gyr, and the red dashes represent the stars > 10 Gyr. The right panel shows histograms of the AD for the four stellar age groups for the example analog 449972. The blue histogram represents stars that are < 1 Gyr, the purple hatch marks represents stars between $1 - 5$ Gyr, the green solid histogram represents stars between $5 - 10$ Gyr, and the red histogram represents the stars > 10 Gyr. In all following figures of AD, the histograms will follow the same style and color pattern for each stellar age bin. The trend of AD increasing as a function of stellar age is clearly visible in this example. In the next section, we describe trends with AD for the primary sample of analogs.

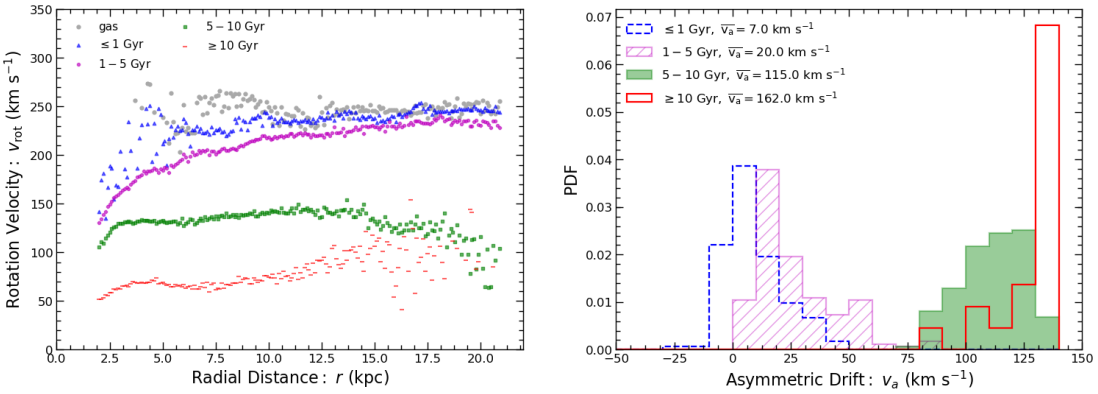

Figure 4.6: Left panel: Radially binned rotation curve for analog 449972. The neutral gas is represented by the grey points, the blue triangles represent stars with ages $<$ 1 Gyr, the purple points represent stars between $1-5$ Gyr, the green squares represent stars between $5-10$ Gyr, and the red dashes represent the stars $>$ 10 Gyr. Right panel: normalized histograms (probability distribution function) of AD values for analog 449972. The blue dashed histogram represents stars that are $<$ 1 Gyr, the one with the purple hatch marks represents stars between $1-5$ Gyr, the green solid histogram represents stars between $5-10$ Gyr, and histogram denoted by the red line represents the stars $>$ 10 Gyr. AD increases with stellar age.

4.4 Results

To calculate the cumulative rotation curves and AD values as a function of stellar age for the whole primary sample, we first calculate both the rotation curve and AD for each individual analog as described in the previous section (see Figure 4.6). Since the rotation curves are radially binned, the cumulative rotation curve for the whole primary sample is constructed by taking the median rotation velocity for each age group along every radial bin. To compare the AD values across all of the analogs, we find the median of AD for each of the four stellar age bins for every analog. Thus, for our primary sample, we have 93 median AD values for each of the four age bins. We show the distribution of these median AD measurements along with the cumulative

Table 4.2: Median AD Values for the Primary Sample

Stellar Age Group	Median AD ($\mathrm{km\,s^{-1}}$)
Group 1: < 1 Gyr	-6^{+5}_{-6}
Group 2: $1 - 5$ Gyr	$+10^{+8}_{-5}$
Group 3: $5 - 10$ Gyr	$+56^{+16}_{-7}$
Group 4: > 10 Gyr	$+103^{+18}_{-33}$

rotation curves across the primary sample of analogs in Figure 4.7. We find there is a progression to higher AD as stellar age increases. This trend and the amplitude of median AD values are aligned with expectations from theory and with the observational study of AD as a function of stellar age in M31 (Quirk et al. 2019). The peak and the width of the distributions ($16^{\mathrm{th}} - 84^{\mathrm{th}}$ percentile) for each age bin are listed in Table 4.4. Quirk et al. (2019) find that stars that lag the gas in M31 tend to do so by 30 $\pm$ 10 % (Quirk et al. 2019), while in the MW stars lagged behind the gas by 11 $\pm$ 8 % (Bovy et al. 2009, 2012). The AD in the MW is similar to that in other local galaxies (e.g. Ciardullo et al. 2004; Herrmann & Ciardullo 2009; Westfall et al. 2007, 2011). These observations probed stars that were younger than Group 4 in this analysis.

Since we aim to understand the possible correlation between AD and merger histories in this work, we use the properties included in the stellar assembly catalogues described in Section 4.2.3 to divide our primary sample into two subgroups: analogs that have experienced a 4:1 merger since a given time and those that have not experienced a merger more recent than the given time. We vary the time frame of interest from the past 4 Gyr, to the past 8 Gyr (approximately the median time of last 4:1 merger across the analogs), and to the past 12 Gyr. We create rotation curves (Figure 4.11) and

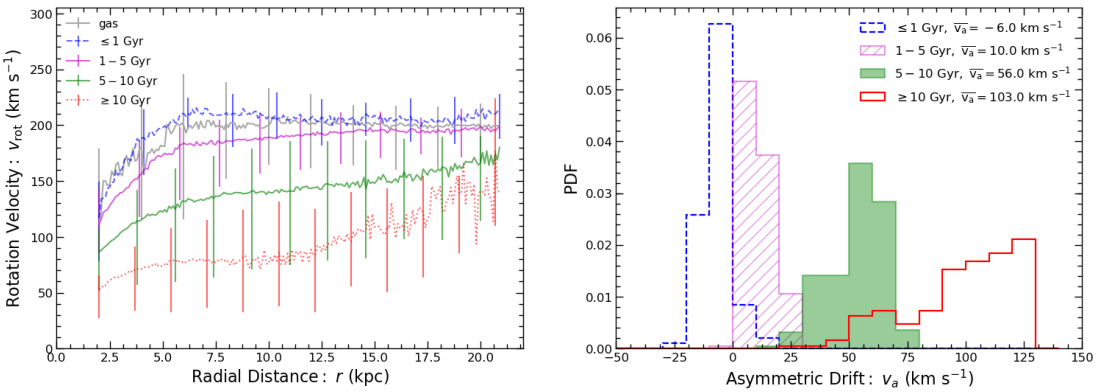

Figure 4.7: Left panel: Rotation curve for the primary sample of analogs. Each point represents the median rotation velocity at a radial bin with a width of 0.1 kpc across all of the analogs in the primary sample. The grey line represents the gas cells, the blue dashed line represent star particles with ages < 1 Gyr, the purple line represents star particles with ages 1-5 Gyr, the green line represents star particles with ages 5-10 Gyr, and the red dotted line represents star particles with ages > 10 Gyr. The vertical bars represent the width of the distribution ($16^{\text{th}} - 84^{\text{th}}$ percentile) of rotation velocities in a given radial bin. Right panel: Normalized histograms (probability distribution function) of AD values for the 93 analogs of the primary sample. For each analog, we find the median AD value of the four age bins; these histograms represent the distribution of those medians across all of the analogs. The colors correspond to the age bins as follows: < 1 Gyr (blue dashed histogram), $1 - 5$ Gyr (purple hatched histogram), $5 - 10$ Gyr (green solid histogram), and > 10 Gyr (red histogram). AD increases with stellar age.

histograms of the median AD (Figure 4.8) for the subgroups for each of the specified time frames. The median AD values are listed in Table 4.4.

In the majority of cases for all time frames, AD is higher in the group that experienced the 4:1 merger than it is in the group that did not have a 4:1 merger more recent than the specified time frame (the "no 4:1 merger group"). magenta. The exception is for Group 1 in the 4 Gyr time frame, where the magnitude of AD is slightly higher for the no 4:1 merger group and Group 2 in the 12 Gyr time frame, where AD is roughly equal for the two subgroups. For all time frames, the largest difference between the two subgroups is in Group 3. These are stars with ages $5 - 10$ Gyr. Brook et al. (2004) show that the epoch in which a star is born can shape its kinematics. For example, they find stars born during a period of rapid hierarchical growth, roughly 8.5 to 10.5 Gyr ago, have the kinematical characteristics of thick disk stars, whereas those born in a quiescent epoch have characteristics that resemble the thin disk. Overall, the total difference in AD between the two subgroups decreases as the time since the last 4:1 merger increases, suggesting that some effects from ancient mergers settle over time.

In all cases, AD also increases with stellar age despite the time of last 4:1 merger. This is particularly interesting when looking at analogs that have not had a 4:1 merger in the past 12 Gyr. For these simulated galaxies, AD must be influenced by other dynamical heating sources, including internal sources of dynamical heating, such as GMCs, galactic bars, and spiral arms or by other external events such as minor mergers and other tidal encounters. Another possible explanation is that stars were born in hotter and less rotationally-supported disks in the past or that the older stars

Table 4.3: Median AD Values as a Function of Merger History

Time Since Last 4:1 Merger	Stellar Age Group	Median AD $[\,\mathrm{km\,s^{-1}}]$ (4:1 Merger)	Median AD $[\,\mathrm{km\,s^{-1}}]$ (No 4:1 Merger)
4 Gyr	Group 1	-4^{+8}_{-8}	-7^{+6}_{-8}
	Group 2	$+30^{+18}_{-19}$	$+6^{+5}_{-3}$
	Group 3	$+91^{+13}_{-15}$	$+43^{+13}_{-12}$
	Group 4	$+131^{+14}_{-39}$	$+100^{+16}_{-27}$
8 Gyr	Group 1	-8^{+6}_{-8}	-5^{+6}_{-7}
	Group 2	$+14^{+10}_{-11}$	$+6^{+6}_{-4}$
	Group 3	$+85^{+9}_{-13}$	$+29^{+16}_{-5}$
	Group 4	$+128^{+14}_{-33}$	$+95^{+15}_{-28}$
12 Gyr	Group 1	-6^{+4}_{-6}	-2^{+17}_{-16}
	Group 2	$+10^{+7}_{-5}$	$+11^{+12}_{-11}$
	Group 3	$+61^{+9}_{-17}$	$+41^{+15}_{-24}$
	Group 4	$+105^{+21}_{-35}$	$+95^{+15}_{26}$

were accreted. In the next section, we will discuss these implications further.

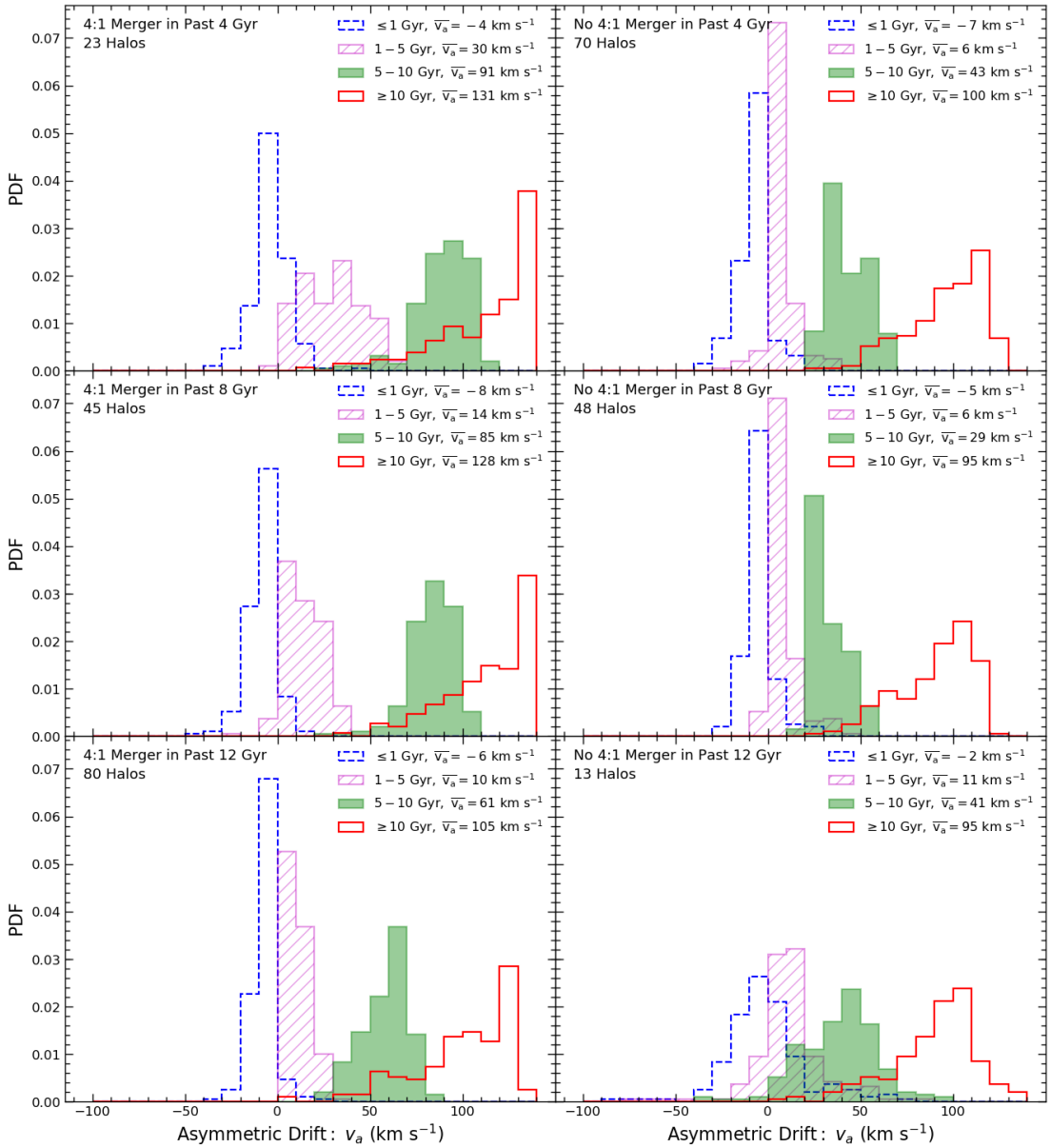

Figure 4.8: Histograms of median AD values for the primary sample of analogs subdivided into two subgroups: those that have had a 4:1 merger (left panels) and those that have not (right panels) in a given time frame. In the top two panels, the time frame is the past 4 Gyr, in the middle panels it's the past 8 Gyr, and in the bottom panels it's the past 12 Gyr. In every panel, the blue histogram stars that are < 1 Gyr, the one with the purple hatch marks represents stars between $1 - 5$ Gyr, the green solid histogram represents stars between $5 - 10$ Gyr, and histogram denoted by the red line represents the stars > 10 Gyr. The number of analogs in each subgroup is written in the top left of each panel. On average, the median AD is higher for the merger subgroups.

4.5 Discussion

4.5.1 Comparisons to Measurements of Asymmetric Drift in Andromeda

We further examine the AD of analogs that have had a 4:1 merger in the past 4 Gyr and those that have not (top panels in Figures 4.8 and 4.11), since recent studies suggest that M31 might have had a major merger in the past several billion years. Figure 4.9 shows the comparison of AD in the simulated analogs to the AD measured in M31 as in Quirk et al. (2019). The blue shaded regions represent AD for the analogs that have experienced a 4:1 merger in the past 4 Gyr, and the pink represents the AD for analogs that have not. The vertical line marks 4 Gyr. Stars to the right of this line existed during the merger event, while stars to the left might have been born during or after the merger.

The smallest difference in AD between the subgroups is in Group 1. These stars would have been born after the merger event. The largest difference is in Group 3. These stars would have formed $1 - 6$ Gyr before the merger. In all cases, AD is higher for the group of analogs that experienced a merger since a given time, showing that recent 4:1 mergers can perturb stars even in the inner 20 kpc of a galaxy.

The black circular points in this figure show the observations of AD from (Quirk et al. 2019). Each point represents an average stellar age for a broad stellar evolution classification: massive main sequence (MS), intermediate mass asymptotic branch (AGB), older AGB, and less massive red giant branch (RGB). To emphasize that each point represents a range of stellar age, we have arbitrarily added dotted horizontal bars on each point to show +/- 50% of the mean age. The star formation

history of M31 is known more precisely than is represented here (Lewis et al. 2015; Williams et al. 2017), but we use broader age bins as to match the analysis in Quirk et al. (2019) and allow for easy comparison. The observational AD measurements from M31 are most similar to the blue shaded region, suggesting that the observed AD trends in M31 could be consistent with a 4:1 merger in the past 4 Gyr. We posit that internal heating could be an explanation for why the observed AD measurements are greater than the median values across the analog sample (see Section 4.5.2). Furthermore, the observational M31 AD measurements are more similar to this analog subgroup than AD measured in analogs with more ancient mergers (the middle and bottom panels of Figure 4.8.) This is a potential piece of evidence that M31 did in fact have a recent major merger and suggests that the GSS could indeed have been formed by a major merger event that also led to prominent features that have been observed in M31's halo such as the various stellar streams, shelves, and tidal features mentioned in Hammer et al. (2018); D'Souza & Bell (2018).

For comparison, we also plot the median AD values for the example analog 449972 in black square points. The properties of this analog are shown in Table 4.1 and Figures 4.5 and 4.6. This analog last had a 4:1 merger 4.12 Gyr ago, but its AD is much higher for the oldest stellar age groups than the overall primary sample. Since this analog has one of the highest $V_{\rm max}$ and $M_\star$ values in our sample, it may provide the best insight on the kinematics of the old stars in M31 relative to the younger stellar populations.

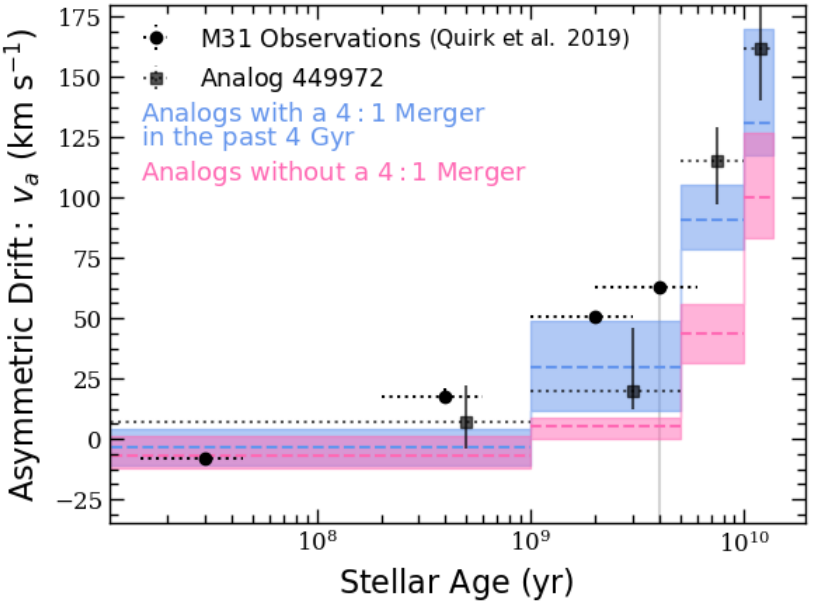

Figure 4.9: AD as a function of stellar age for the primary sample of analogs and observations of M31's disk. The shaded regions represent the median AD of stellar Groups 1, 2, 3, and 4 from the primary sample of analogs. The dashed lines in each region shows the median AD value, and the shading shows the 1σ confidence levels. The blue represents analogs that have experienced a 4:1 merger within the past 4 Gyr, and the pink represents those that have not. The vertical line marks 4 Gyr. The black squares represent the median AD for the example analog 449972. This analog last had a 4:1 merger 4.12 Gyr ago. The observations from Quirk et al. (2019) are the black circles. The observations are most similar to the AD from the analogs that have experienced a 4:1 merger within the past 4 Gyr.

4.5.2 Assessing the Influence of Minor Mergers and Other Effects on AD

The AD observed in M31 naturally includes minor mergers, other tidal fly-bys, and sources of internal heating. The resolution of IllustrisTNG-100 does not allow us to probe how AD is affected by internal sources, like scattering via GMCs and spiral arms, as many internal heating sources rely on a thin disk. However, we can assess whether minor mergers play a significant role in the magnitude of AD and in the increasing AD as a function of stellar age using the primary sample.

To check whether minor mergers can also influence AD, we find five analogs in the primary sample with no 4:1 merger in the past 13.1 Gyr and analyze their dynamics based on the number of 10:1 mergers they have experienced. These five halos are split into a subgroup containing the halos that have experienced five to six 10:1 mergers and those that have only experienced zero or one 10:1 merger. AD increases with stellar age for all five halos. The AD for stellar age Groups 1, 2, and 3 is independent of the number of 10:1 mergers. The AD for the oldest stars (Group 4) is higher ($\sim$ 20 km s^{-1}) in the analogs with the most 10:1 mergers but is still significantly below that of the AD for the primary sample, indicating that 4:1 mergers play a much larger role in influencing AD than 10:1 mergers. Furthermore, this suggests that minor mergers cannot explain why AD increases with stellar age (see also Section 4.4, Figure 4.8) but rather that this pattern is likely a signature of any of the following processes: physical sources of internal heating, older stars being born with hotter birth kinematics, or from older stars born ex-situ. AD can be as high as 65 km s^{-1} for stellar age Group 4 even for analogs

with zero or one 10:1 merger and no 4:1 mergers.Understanding the specifics of internal heating events versus artificial noise and their separate contributions to AD requires further work with a set of higher resolution simulations and is beyond the scope of this analysis.

4.6 Summary and Conclusions

We have analyzed the AD of M31 mass analogs in the IllustrisTNG simulation to look for trends with stellar age. For the 93 analogs in our primary sample, we also examined merger histories to look for any correlations with AD. Our main conclusions are summarized below:

1. We find that AD for M31 mass analogs in the IllustrisTNG simulation increases with stellar age, as in the observations in (Quirk et al. 2019). Our stellar age bins are defined as Group 1: $<$ 1 Gyr, Group 2: 1-5 Gyr, Group 3: 5-10 Gyr, and Group 4: $>$ 10 Gyr. Each stellar age bin is compared to the properties of neutral gas, defined as gas cells with neutral hydrogen fractions ¿ 0.6.

2. The M31 mass analogs are selected independently from their merger histories. Upon examining their merger trees, we find that major mergers do affect the value of AD. However, they are not the sole agent giving rise to observed trends in AD as we find that AD increases as a function of stellar age even without a major merger event. Thus, AD is also influenced by internal dynamical heating, minor mergers and birth kinematics. Understanding the specific internal processes by which AD is affected requires a suite of higher resolution zoom-in simulations such as Auriga

or IllustrisTNG50.

3. We divide the primary sample into two subgroups based on the analogs that have experienced a 4:1 merger since a given time (i.e, in the last 4 Gyr, 8 Gyr, and 12 Gyr) and those that have not experienced a merger more recent than the given time to determine how strongly AD is affected by the most recent major merger. On average, analogs that have experienced a merger have higher AD (up to a 48 km s^{-1} difference) than those analogs that have not experienced a merger in the time frame of interest. The effect is greatest for stars in Group 3: those with age $5 - 10$ Gyr, regardless of time since the last 4:1 merger.

4. The AD measurements observed in the disk of M31 from Quirk et al. (2019) are similar to the subgroup of the primary sample that experienced a 4:1 merger within the past 4 Gyr. This is a piece of evidence that M31 may have experienced a major merger event in the past several billion years.

4.7 Appendix

4.7.1 Particle Density Plots for Example Analog 449972

Figure 4.10 shows a more detailed view of analog 449972's geometry. The left panel shows the gas cell density in the inner 100 kpc of the simulated galaxy. The right panel shows the stellar particle density across the same extent. The orange and gray circles illustrates the 20 kpc region encompassing the data in the left and right panels, respectively. All rotation curves are calculated using particle/cell data within this 20 kpc region relative to the COM. For this M31 analog, 56% of gas cells with $n_H > 0.6$ and 97% of stellar particles are encompassed by the 20 kpc radius, so the rotation curves used to calculate AD are representative of the most prominent inner regions of the M31 analogs with little contamination from non-spherical substructures.

4.7.2 Primary Sample Rotation Curves

In this section, we show the rotation curves from the merger and no merger subgroups (Figure 4.11). These rotation curves are used to make the histograms of AD shown in Figure 4.8. The vertical gap between the stellar particle rotation curves and the gas data rotation curve is a visual representation of AD.

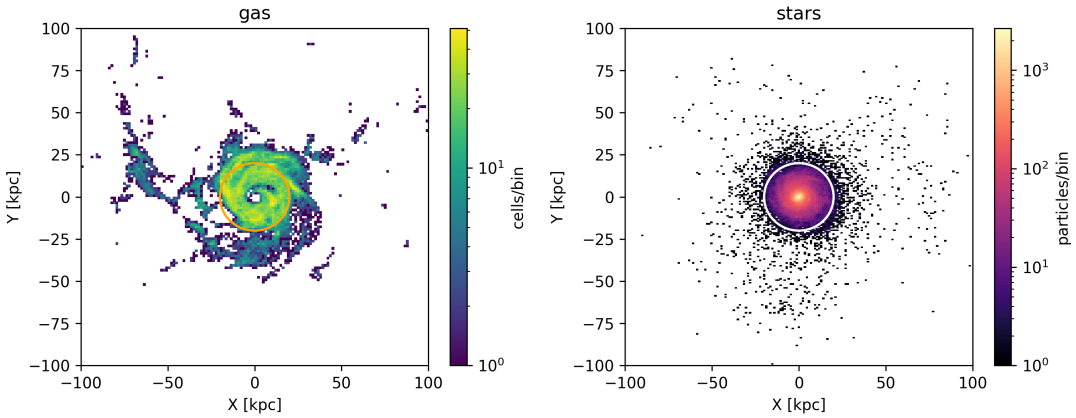

Figure 4.10: Density maps for one M31 analog (ID 449772). The data has been rotated to the face-on reference frame as described in Section 4.3.1 and only includes particles within 10 kpc of the disk plane. The left panel shows the gas density only for the cells where $n_H > 0.6$ and the right panel shows the stellar density. In the left and right panels, the orange and white circles, respectively, denote a radius of 20 kpc.

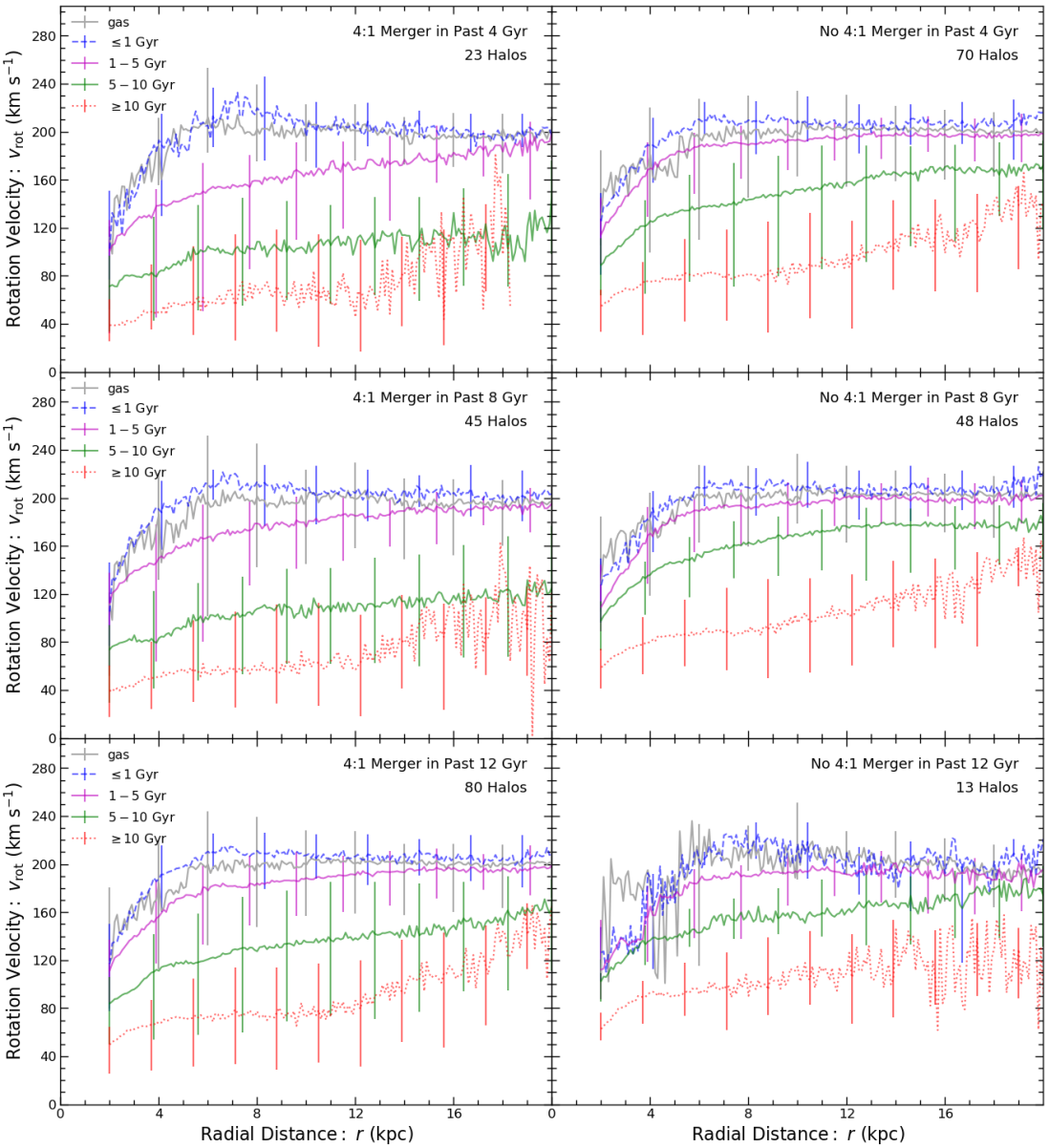

Figure 4.11: Rotation curves for the primary sample of analogs subdivided into two groups: those that have had a recent 4:1 merger (left panels) and those that have not (right panels). In the top two panels, we define 4:1 merger time frame as having occurred in the last 4 Gyr. In the middle panels, the time frame is 8 Gyr, and in the bottom panels it is 12 Gyr. In every panel, the grey line shows the rotation curve of the neutral gas, the blue dashed line represents stars that are < 1 Gyr, the purple represents stars between $1 - 5$ Gyr, the green represents stars between $5 - 10$ Gyr, and the red dotted line represents the stars > 10 Gyr. The vertical bars show the width of distribution of median rotation values ($16^{\text{th}} - 84^{\text{th}}$ percentile) across all of the analogs at a given radial bin. The oscillations in the individual rotation curves shows the radial variations in rotation velocity.

Chapter 5

The Triangulum Extended (TREX) Survey: The Stellar Disk Dynamics of M33 as a Function of Stellar Age

5.1 Introduction

The Triangulum Galaxy (M33) is one of two dwarf spirals in the Local Group (Gaia Collaboration et al. 2021). With a stellar mass of roughly $4.8 \times 10^9 M_\odot$ (Corbelli et al. 2014), it is ten times less massive than the Milky Way (MW) and Andromeda (M31) and twice as massive as the Large Magellanic Cloud (LMC). It has a high star formation rate (SFR), $\sim 0.7 M_\odot \mathrm{yr}^{-1}$ (Blitz & Rosolowsky 2006), characteristic of later

type spirals. Furthermore, it is a relatively isolated galaxy, making its disk more pristine. As high redshift galaxy observations push down to lower stellar masses, M33 becomes an important local comparison point.

While M33 is sufficiently close to be studied in detail, much remains unknown. For example, there is debate as to its interaction history with M31. Some of M33's properties could be explained by an interaction; such as its highly warped H I disk that extends far beyond the stellar disk, out to 22 kpc (Braun & Thilker 2004; Putman et al. 2009; Semczuk et al. 2018), the apparent disturbances to the outskirts of M33's stellar disk (McConnachie et al. 2009; McConnachie et al. 2010), and the mutual burst of star formation $2-4$ Gyr ago for both M31 and M33 (e.g., Putman et al. 2009; McConnachie et al. 2009; Lewis et al. 2015; Ferguson & Mackey 2016; Semczuk et al. 2018; Williams et al. 2017). However, new studies using the proper motion of both galaxies from Gaia DR2, the Hubble Space Telescope (HST) and the Very Long Baseline Array (VLBA), and cosmological simulations support the notion that M33 is on its first infall (Patel et al. 2017; Patel et al. 2017; van der Marel et al. 2018) and has had no significant interaction with M31.

Furthermore, M33 is more complex then expected for a low luminosity galaxy, which are thought to be dominated by a single component, although the highest mass dwarfs can have a thick disk in addition to a stellar halo (Roychowdhury et al. 2013; van der Wel et al. 2014; Patra Nath 2020; Kado-Fong et al. 2020, 2021). However, M33, is proving to be more complex, with a newly confirmed centrally-concentrated halo (Gilbert et al. 2022) and bar (Williams et al. 2021; Smercina & et al. in preparation;

Lazzarini & et al. in preparation) and the mysterious warps described above (Braun & Thilker 2004; Putman et al. 2009; Semczuk et al. 2018).

Resolved stellar spectroscopy is a valuable tool to unlock the history of M33, especially when information from spectroscopic observations is examined as a function of stellar age. This is *only* possible in the Local Group, in which the distances to galaxies allow us to view their entire disk while resolving individual stars. For example, stellar line-of-sight velocity dispersion as a function of stellar age can point to gradual heating and heating via one event, as seen in M31, where the high velocity dispersion increases monotonically with stellar age, suggesting a constant and violent merger history (Dorman et al. 2015). Comparing stellar kinematics to gas kinematics can also give insight into a galaxy's dynamical heating history, as was demonstrated in M31 (Quirk et al. 2019), as the asymmetric drift of stellar populations is correlated with their velocity dispersion in the plane of the disk. Furthermore, comparing this observed asymmetric drift to that in simulations suggests that M31 had a relatively recent 4:1 merger (Quirk & Patel 2020). M33's distance of 859 kpc (de Grijs & Bono 2014) is comparable to that of M31 (McConnachie et al. 2009), so we can measure spectroscopy of individually resolved stars in M33. These techniques may also be capable of constraining the merger history of M33.

We expect M33 to be a particularly interesting target for these studies. Unlike M31's obvious remnants from its violent history, M33 is morphologically less disturbed. It has however a much higher SFR (Blitz & Rosolowsky 2006) and lower disk mass surface density (Corbelli et al. 2014), placing its disk in a very different regime than

M31's. M33 is also the prime environment to observe the effects of internal heating (i.e., bursts from star formation, perturbations from giant molecular clouds and the bar, and density waves from spiral arms) because of its low mass and low inclination (Warner et al. 1973, $\sim 54°$). Stellar feedback can cause powerful inflows and outflows of gas and bursts of star formation, which can result in drastic radial migration in low mass galaxies and can even lead to the creation of a stellar halo (e.g., Stinson et al. 2009; Maxwell et al. 2012; El-Badry et al. 2016). This internal feedback could have drastically changed the stellar kinematics of M33 since its birth. Stellar disks are fragile (Toth & Ostriker 1992), and while more massive disks are likely able to survive major merger events (e.g., D'Souza & Bell 2018; Hammer et al. 2018) and low mass disks are believed to have to survive many minor events (Helmi et al. 2012), low mass disks, like that of M33, are unlikely to remain intact after major merging events. This notion paired with the fact that M33 is relatively isolated ($\sim$ 230 kpc from M31), and about half of its stellar mass comes from stars that are $\sim$ 10 Gyr (Williams et al. 2009), means that the disk of M33 is fairly pristine and therefore can give us insight into the evolution of isolated high redshift galaxies.

In this paper, we present the TRiangulum EXtended (TREX) Survey of $\sim$ 7000 *targets, making it the largest stellar spectroscopic survey of M33.* The survey spans across the entire disk of M33, out to a deprojected radius of $\sim$ 11 kpc. It is the first dataset that consists of individually resolved stars that extends across the entire inner and into the outer disk. *With this dataset, we examine the kinematics of stars in the disk of M33 as a function of stellar age to measure the dynamical heating of the evolving*

disk. This analysis, which uses a subset of the total sample, is the first study of disk kinematics as a function of stellar age in M33 using only individual stars and is overall the third of its kind (after the MW and M31). The robust dataset presented here has already been used to confirm the existence of a dynamically hot component in M33 (Gilbert et al. 2022).

This paper is organized as follows. In Section 5.2 we present our new spectroscopic dataset and archival datasets used in this study. Section 5.3 describes the separation of stars into broad age bins and the removal of possible halo stars, and Section 5.4 shows the calculation of local velocity dispersion, rotation velocity, and asymmetric drift. Section 5.5 highlights a comparison of observed kinematics to the kinematics seen in M33-like simulated galaxies, and Section 5.6 compares them to the kinematics of M31 and the MW Solar Neighborhood. We summarize the main points of this work in Section 5.7, and in Section 5.8.1, we show the kinematics of rare spectral types.

5.2 Data

Our study made use of large catalogs of stellar photometry and spectroscopy, as well as imaging data of the M33 gas content. Below we describe the photometric, stellar spectroscopic, and gas imaging catalogs.

5.2.1 Stellar Data

We started with large libraries of resolved stellar data, including space-based and ground-based photometry. These, in turn, allowed us to obtain our stellar spectroscopic dataset. We selected targets from a wide range of masses and evolutionary stages, including massive main sequence (MS), massive helium burning (HeB), intermediate mass asymptotic giant branch (AGB), and low mass red giant branch (RGB) stars. The use of these different stellar types is described later in Section 5.3. These different stages were not prioritized equally over the four observing epochs, see description below and Figure 5.2. The broad evolutionary stage of a star comes from color magnitude diagrams (CMD) of the photometry catalogs described in Section 5.2.1. We describe this process in detail below.

Photometry

Our strategy for target selection relies on selecting bright isolated stars from resolved stellar photometry. The high precision of this photometry allows us to target stars in the crowded central regions of M33 with confidence that we were observing isolated stars instead of blended light from multiple sources.

Over the four years of spectroscopic observations, our stellar selection varied in response to the available photometry and evolving scientific opportunities, as stated in Figure 5.2. We relied on a mix of photometry from the Hubble Space Telescope (HST) and the Canada-France-Hawaii Telescope (CFHT). Targets observed in 2016 were selected using archival HST data with broad bands F475W + F814W, or F606W

+ F814W or where there was a gap in HST coverage, using data from MegaCam on CFHT with $i-$ and $g-$ bands. The HST fields were observed with the Advanced Camera for Surveys (ACS) and the reduction is described in Williams et al. (2009, 2014). Each of the 2016 masks overlapped with multiple of these ACS fields. The CFHT/MegaCam data was reduced using the MegaPipe reduction pipeline (Gwyn 2008). The primary targets for these masks were RGB stars, but also included some AGB and red HeB stars and a small number of MS and BHeB stars.

The 2018 and 2019 slitmasks had targets selected from HST photometry from the Panchromatic Hubble Andromeda Treasury: Triangulum Extended Region (Williams et al. 2021, PHATTER) and CFHT/MegaCam (same as described above). The PHATTER survey observed stars in the Andromeda and Triangulum galaxies with six filter photometry using ACS and WFC3: F275W, F336W, F475W, F814W, F110W, and F160W (Dalcanton et al. 2012; Williams et al. 2021). The photometric catalogs are described in Williams et al. (2014, 2021).

The availability of six filter photometry allows us to more precisely divide stars into broad age bins, as described later in Section 5.3. With the six filter photometry, we were able to target a range of stellar evolutionary stages for the 2018 masks: MS, HeB, AGB, and RGB stars. To sample a broad range of stellar ages, we preferentially targeted rarer stars, including a large number of bright HeB stars. These stars were identified from PHATTER CMDs. CFHT/MegaCam data was used to fill in the outer parts of the DEIMOS slitmasks that extended beyond the HST PHATTER footprint, into the low density outer disk where HST resolution is less needed. For the 2019 masks, RGB

stars were the primary targets. These stars were identified from PHATTER CMDs if in the PHATTER range. If they came from the CFHT/MegaCam MegaPipe reduction, we prioritized stars with $g - i > 0.5$ and $21 < i < 22$.

The 2020 slitmasks were positioned to probe the outer disk, and they are beyond the PHATTER footprint and any other continuous HST coverage. For these outer slitmasks, we used the catalog from the Pan-Andromeda Archaeological Survey (PAndAS) (McConnachie et al. 2018). PAndAS used CFHT/Megacam to observe >400 square degrees of sky centered on Andromeda and Triangulum with $i-$ and $g-$ bands. The observations and data reduction are described in McConnachie et al. (2018). Only objects that were flagged by the PAndAS team to most likely be stars were included in our target list. We prioritized placing RGB stars on these masks ($g - i > 0.5$ and $20.5 < i < 22.5$).

To avoid blends, especially in the crowded central regions, we applied an isolation criterion $I_{neighbor} < I_{target} - (\frac{d}{0.8''})^2 + 3$ to exclude stars with neighbors that are too close and/or too bright and therefore might contaminate the target's light during spectroscopic observation with DEIMOS(Dorman et al. 2012). We applied this criterion to all of the photometry catalogs used, although it was most critical for the crowded regions targeted using PHATTER photometry. If a target candidate has a single neighbor that fulfills this criterion, it is excluded from the slitmask.

Even with this criterion, it is possible to have multiple objects in a given slit. The majority of these serendipitous observations have good quality spectra and well-measured velocities that did not interfere with the main target's spectrum. However,

since we do not have easily paired photometry for these objects, we do not include them in this particular study, although they will eventually be incorporated. The total number of targets is 7684, with 2381 from 2016, 2457 from 2018, 906 from 2019, and 1940 from 2020. Adding in the serendipitous targets would increase the sample by $\sim 27\%$.

Keck II DEIMOS Spectroscopy

The spectroscopic data comes from four epochs of observing. All observations were taken with the DEIMOS Spectrograph (Faber et al. 2003) on the Keck II 10 meter telescope. The program uses thirty-six DEIMOS slitmasks and two different grating setups– one to target a wide range of stellar evolutionary phases and one to target older, redder stars. The first ten slitmasks were observed in 2016 using the 600 line mm^{-1} grating, which has a resolution of $R \sim 2000$, and a central wavelength and wavelength range of 7200Å and $\lambda \sim 4600$–9800 Å, respectively. This setting allows us to target a wide range of spectral types. In 2018, we observed eleven slitmasks across the central disk using the same configuration. In 2019, we obtained four additional slitmasks of spectroscopic data. The first used the 600 line mm^{-1} grating configuration, and the remaining three were observed using the 1200 line mm^{-1} grating ($R \sim 6000$) to account for additional moon light and to target older stars. With this grating, we used a central wavelength of 7800Å and a wavelength range of $\lambda \sim 6300$–9800 Å, focusing on the redder part of the spectrum where RGB stars emit significant flux. In the Fall of 2020, we observed the last eleven slitmasks in the outer disk with the 1200 line mm^{-1} configuration.

The layout of the thirty six slitmasks can be seen in Figure 5.1. Because of the high density of stars in the inner regions, we were able to have slitmasks targeting different stars at the same slitmask location and orientation. Some of the targets on different slitmasks were repeated to get higher signal for faint targets and to help calibrate velocity measurement errors. The positions of the 2019 slitmasks are the same as the two most northern 2018 slitmasks. Each slitmask was observed for approximately 2 hours. The table in Figure 5.2 lists the names, positions, orientations, exposure times, numbers of stars observed, years observed, gratings used, photometry sources for target selection, and the main targets for each DEIMOS slitmask. For primary targets, "range" indicates MS, HeB, AGB, and RGB stars.

The DEIMOS spectra were reduced with the `spec2d` and `spec1d` programs (Cooper et al. 2012; Newman et al. 2013). This software has been adapted from its original use for the Sloan Digital Sky Survey to be used on DEIMOS spectroscopy. The resulting one-dimensional spectra were flat-fielded and sky subtracted and then cross correlated against stellar template spectra to measure the line-of-sight velocity of the target star (Simon & Geha 2007). The velocity measurements were confirmed visually using the `zspec` software. At this step, each measurement is given a quality rating, and rare stars and MW foreground stars are identified (more details below). We then shifted the velocities to the heliocentric frame.

We account for possible miscentering of the star in the slit width direction, which causes a systematic wavelength shift. To do so, we calculated the wavelength shift of the atmospheric absorption line at 7600 Å. We call this shift the A-band correction

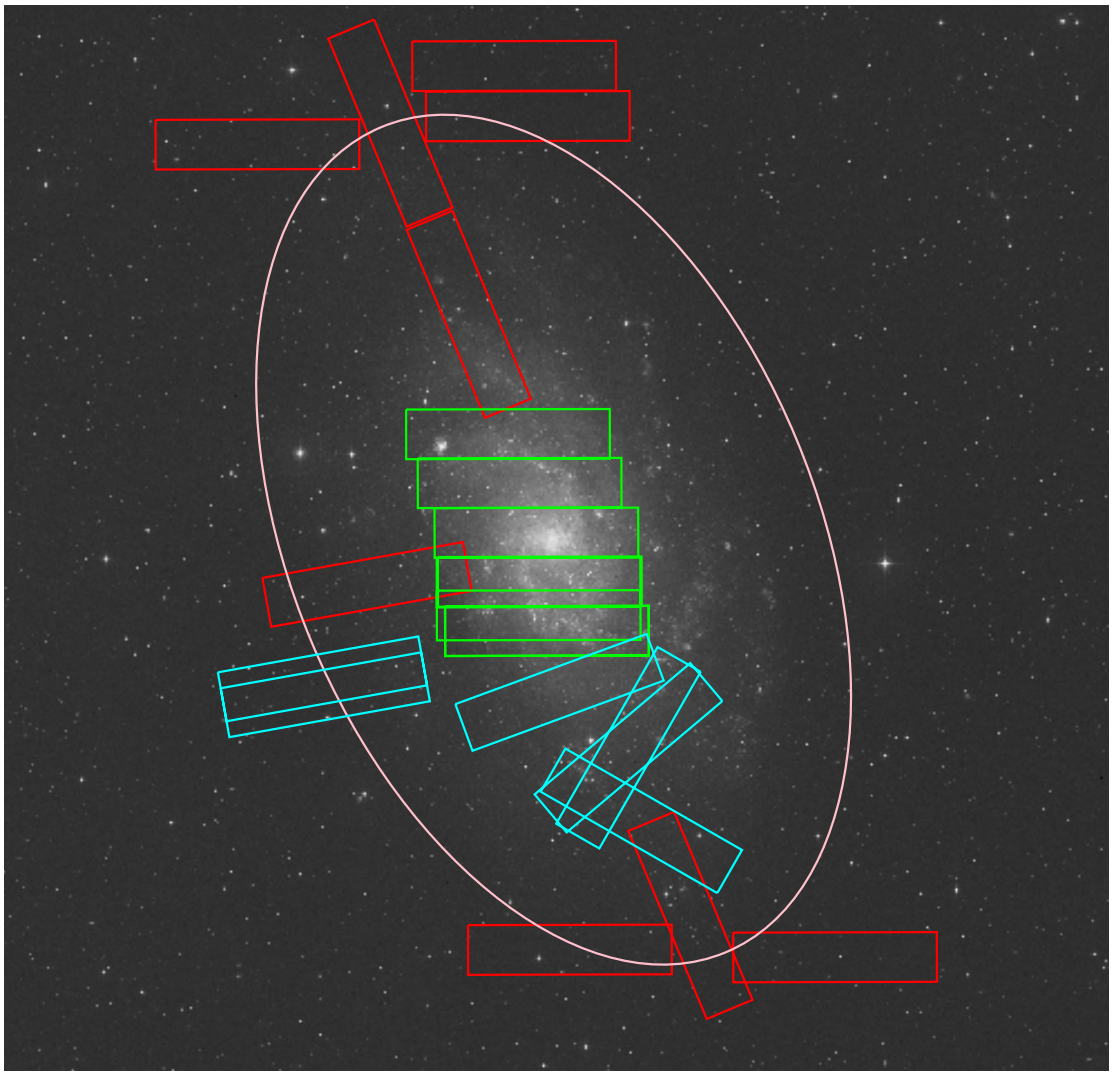

Figure 5.1: Layout and orientation of the thirty six DEIMOS slitmasks across the disk of M33 for the TREX Survey. Each rectangle on the image represents the rough shape and size of a DEIMOS slitmask (approximately 16′by 4′). The cyan bricks were observed in 2016, the green in 2018 and 2019, and the red in 2020. Because of the high density of stars in the central regions, we targeted different stars at the same slitmask position in 2018 and 2019. The 2019 slitmasks placements are the top two green slitmasks. The ellipse represents the approximate location of a break in the exponential surface density profile of the disk at $\sim 36'$ (Ferguson et al. 2007; Barker et al. 2011). The background image of M33 is from the Digital Sky Survey (DSS). In this orientation, north is up, and east is to the left.

Name	Center (J200)	Mask PA (°)	Exposure Time (min)	N Targets	Year	Grating (l mm^{-1})	Photometry Source	Primary Targets
M33D2A	1:33:47.95 30:27:18.8	110	76	246	2016	600	Archival HST + CFHT	RGB
M33D2B	1:33:47.95 30:27:18.8	110	88	244	2016	600	Archival HST + CFHT	RGB
M33D3A	1:33:22.21 30:22:50.3	310	72	250	2016	600	Archival HST + CFHT	RGB
M33D3B	1:33:22.21 30:22:50.3	330	70	252	2016	600	Archival HST + CFHT	RGB
M33D3D	1:33:22.21 30:22:50.3	310	70	244	2016	600	Archival HST + CFHT	RGB
M33D4A	1:33:17.50 30:16:56.9	240	70	239	2016	600	Archival HST + CFHT	RGB
M33D4B	1:33:17.50 30:16:56.9	240	84	227	2016	600	Archival HST + CFHT	RGB
M33D4C	1:33:17.50 30:16:56.9	240	76	233	2016	600	Archival HST + CFHT	RGB
M33MA1	1:35:16.71 30:28:25.4	100	76	225	2016	600	Archival HST + CFHT	RGB
M33MA2	1:35:15.66 30:27:08.6	100	67	221	2016	600	Archival HST + CFHT	RGB
A1M33P	1:33:52.61 30:32:15.9	90	112	234	2018	600	PHATTER + CFHT	range
A2M33P	1:33:52.60 30:32:15.9	90	112	245	2018	600	PHATTER + CFHT	range
B1M33P	1:33:55.69 30:36:10.8	90	149.2*	226	2018	600	PHATTER + CFHT	range
B2M33P	1:33:55.23 30:36:14.4	90	81.5	209	2018	600	PHATTER + CFHT	range
C1M33P	1:33:56.46 30:40:10.4	90	120	208	2018	600	PHATTER + CFHT	range
C2M33P	1:33:56.46 30:40:10.4	90	110	200	2018	600	PHATTER + CFHT	range
D1M33P	1:34:02.73 30:44:11.0	90	132.5	220	2018	600	PHATTER + CFHT	range
D2M33P	1:34:02.73 30:44:11.0	90	110	213	2018	600	PHATTER + CFHT	range
E1M33P	1:34:07.06 30:48:07.2	90	120	228	2018	600	PHATTER + CFHT	range
E2M33P	1:34:07.06 30:48:07.2	90	120	224	2018	600	PHATTER + CFHT	range
K1M33P	1:33:55.69 30:33:31.8	90	117.7	250	2018	600	PHATTER + CFHT	range
D1M33R	1:34:02.73 30:44:11.0	90	100	240	2019	1200G	PHATTER + CFHT	RGB
D2M33R	1:34:02.73 30:44:11.0	90	193*	226	2019	1200G	PHATTER + CFHT	RGB
E1M33R19	1:34:07.06 30:48:07.2	90	62.5	201	2019	600	PHATTER + CFHT	RGB
E2M33R	1:34:07.06 30:48:07.2	90	100	239	2019	1200G	PHATTER + CFHT	RGB
pTE1	1:35:00.02 30:36:01.6	100	108	200	2020	1200G	PAndAS	RGB
pTN1a	1:34:51.22 31:13:10.7	100	120	194	2020	1200G	PAndAS	RGB
pTN1b	1:34:51.22 31:13:10.7	22.5	120	174	2020	1200G	PAndAS	RGB
pTN2a	1:34:21.72 30:57:46.6	22.5	180*	218	2020	1200G	PAndAS	RGB
pTN2b	1:34:21.72 30:57:46.6	22.5	108	214	2020	1200G	PAndAS	RGB
pTN3	1:34:04.46 31:17:45.8	90	120	143	2020	1200G	PAndAS	RGB
pTN4	1:33:59.33 31:13:43.0	90	129.2	166	2020	1200G	PAndAS	RGB
pTN5	1:35:41.37 31:11:27.2	90	108	147	2020	1200G	PAndAS	RGB
pTS1	1:32:59.31 30:09:19.0	22.5	108	183	2020	1200G	PAndAS	RGB
pTS2	1:32:05.42 30:05:53.2	90	71	137	2020	1200G	PAndAS	RGB
pTS3	1:33:44.32 30:06:35.3	90	115	164	2020	1200G	PAndAS	RGB

Figure 5.2: Information for the 36 DEIMOS slitmasks that make up the TREX Survey. The position angle (PA) of the long axis of the slitmask is measured counterclockwise from north. Exposure times marked with an asterisk do not represent the effective exposure time and include exposures with bad seeing.

and applied it to the measured velocity of the star. We found that the A-band correction varies across the mask depending on the slit's position along the length of the mask, possibly because of a slight positional and/or rotational misalignment of the mask in the sky. To account for the spatial variation, we fitted a polynomial to the A-band velocity as a function of mask position for the stars with the best quality spectra. The polynomial was then applied to all stars to calculate the A-band correction based on the stars' positions along the mask. A typical A-band correction is $\sim -1.3\,\mathrm{km\,s^{-1}}$ and varies by $\sim 7\,\mathrm{km\,s^{-1}}$ across a mask.

The systematic uncertainties for the old stars observed with the 600 line $\mathrm{mm^{-1}}$ and 1200 line $\mathrm{mm^{-1}}$ gratings were calculated as in Simon & Geha (2007); Collins et al. (2011), giving 5.6 $\mathrm{km\,s^{-1}}$for the 600 line $\mathrm{mm^{-1}}$ and 2.2 $\mathrm{km\,s^{-1}}$for the 1200 line $\mathrm{mm^{-1}}$ grating. We also estimate random uncertainties, derived from duplicate velocity cross correlation measurements of RGB stars (1.65 $\mathrm{km\,s^{-1}}$for the 600 line $\mathrm{mm^{-1}}$ and 1.85 $\mathrm{km\,s^{-1}}$for the 1200 line $\mathrm{mm^{-1}}$ grating). The final error is the result of adding the estimated random uncertainties to the systematic uncertainties in quadrature. We do not yet have enough duplicate observations of young and intermediate age stars to calculate an estimate of the systematic uncertainty. Initial analysis of the duplicate young stars suggest that a typical velocity measurement error for these stars is $\sim$ 12 $\mathrm{km\,s^{-1}}$. For now, we take the velocity errors from the `spec1d` pipeline (Cooper et al. 2012; Newman et al. 2013) for the young and intermediate age stars. A typical velocity error measurement is assumed to be ~ 6 $\mathrm{km\,s^{-1}}$, but this is likely an underestimate of the true velocity uncertainty. We will rectify this in the future after obtaining a larger

sample of repeat observations.

MW foreground stars are not identified during target selection. Instead, they are removed from our sample if there is Na I absorption present during visual inspection of their spectra, as this indicates the star is likely a dwarf star (Gilbert et al. 2006). Once these visually classified foreground stars are removed, we compared the line-of-sight velocities of the remaining stars to a Besancon model (Robin et al. 2003, 2014; Robin et al. 2017; Amôres et al. 2017) at the location of the TREX Survey with a color and magnitude cut similar to the range of the targets, shown in Figure 5.3. The MW foreground stars have radial velocities that peak at -39 km s^{-1}, with 57% of the distribution at > -50 km s^{-1}. Only 18 stars, or 0.70% of our *final* sample (described in Section 5.3) has line-of-sight velocities > -50 km s^{-1}, so our study is largely free of MW contamination.

Targets are also removed from our sample if their spectra suggests the target is an extended source (i.e., background galaxy) or if the quality of the spectrum is too poor to return a well measured velocity. We also eliminate stars with $|v_{LOS}| > 500$kms^{-1} or that are miscentered in the slit enough to cause a needed correction on the order of 80kms^{-1} (Sohn et al. 2007; Simon & Geha 2007) based on the polynomial fit estimate. Stars with extreme velocities compared to M33's systematic velocity are unlikely to be members of M33 or to have properly measured velocities. With foreground stars, poor quality targets, and duplicate measurements removed, our spectroscopic dataset consists of 4118 stars in M33. In this specific study, we further narrow our sample based on velocity measurement error (Section 5.4), CMD placement (Section 5.3), and, for the

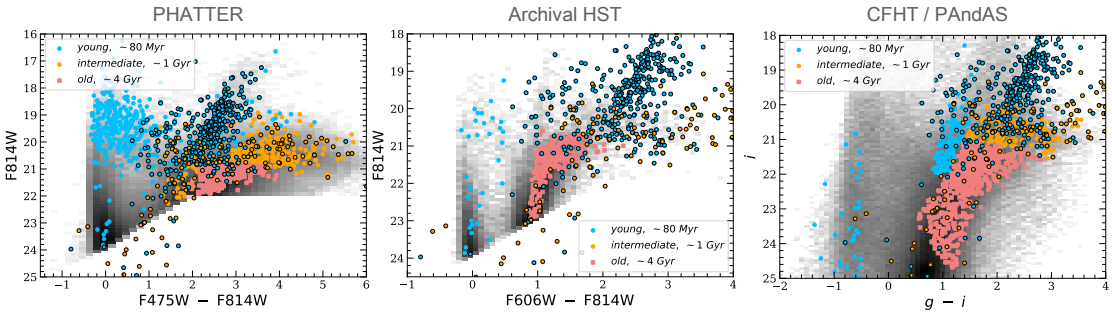

Figure 5.3: Color-magnitude diagrams of the subsets of photometric catalogs used for target selection with the final stellar sample overplotted. The left panel shows stars with HST photometry with the F457W and F814W bands. Most of these stars are from the PHATTER survey; some are from archival HST images. The center panel shows stars selected from archival HST photometry with the F606W and F814W bands only. The right CMD shows stars selected from the CFHT/Megacam + MegaPipe and from the PAndAS catalogue. In each panel, the blue points represent the young stars, the orange represents the intermediate age stars, and the red squares represent the old stars, and the grey represents a Hess diagram version of the full photometric catalogs. The points outlined in black are young weak CN stars (blue) and intermediate age carbon stars (orange) with ages derived from spectroscopic analysis instead of CMD divisions; see Appendix 5.8.1 for more details. We list the adopted average age for each bin in the legend. All magnitudes have been extinction corrected.

older stars, the probability of belonging to the stellar disk component (Section 5.3.1). With the final sample of resolved spectroscopy, we can examine the line-of-sight velocity for individual stars across the disk in M33.

5.2.2 Gas Data

Unlike stars, which retain their kinematic memories of past dynamical heating, dense gas's comparatively rapid cooling dissipates energy, leaving the gas as a low velocity dispersion tracer of the disk's gravitational potential. In this study, we use velocity measurements of H I, CO, and Hα to make comparisons between the dynamics of the gas and stars in the disk of M33.

The H I measurements from the Very Large Array (VLA) are described in

Gratier et al. (2010) and have 5″–25″ resolution (FWHM), depending on the specific pointing (see their Table 2 and 3). The data are from archival VLA imaging obtained in 1997, 1998, and 2001. The resulting gas line-of-sight velocities have an RMS uncertainty of $\sim 1.3\,\mathrm{km\,s^{-1}}$.

The CO(2-1) data were observed using the Institute for Radio Astronomy in the Millimeter Range (IRAM) 30 meter antenna by Gratier et al. (2010); Druard et al. (2014). The observations began in 2008 and build off of those from Gardan et al. (2007). The angular resolution of the data is 12′ with a spectral resolution of 2.6 $\mathrm{km\,s^{-1}}$ (RMS).

The Hα measurements were observed by Kam et al. (2015) at Observatoire du Mont Megantic with a 1.6-m telescope and the Fabry-Perot interferometer in September 2012, producing an angular resolution of $\leq 3''$ and a typical velocity measurement uncertainty is $\sim 10\,\mathrm{km\,s^{-1}}$ (FWHM).

Further details on the observations and data reduction are described in the references listed above. All of the gas velocity measurements have been shifted to the heliocentric frame. Each star corresponds to a specific a single pixel of the gas maps, which allows us to make local and direct comparisons of the gas and stellar kinematics. In Section 5.4.1, we discuss how we locally average the stellar kinematics to better match the resolution of the gas imaging so that one star does not represent the stellar kinematics of an entire pixel in a gas map.

The extent of the H I dataset is vast, so we are able to pair almost all stars with the nearest (in projection) H I velocity measurement. The percentages of stars paired with H I measurements are 91%, 79%, and 71% for the young, intermediate age, and

old stars, respectively. (We discuss the division of stars into age bins in Section 5.3). The CO and Hα velocity measurement maps have a smaller extent so only stars with a projected radius of ≤ 4 kpc are able to be paired to a CO and Hα measurement. For Hα, this includes 24%, 12%, and 4% for the young, intermediate age, and old stars. For the CO, it covers 34%, 25%, and 12% for the young, intermediate age, and old stars.

5.3 Broad Age Groups

We divide stars loosely into three age groups based on average stellar age at present day. First we use color magnitude diagrams (CMD). Different regions on a CMD are dominated by stars of different masses and ages. For example, the MS-dominated region we target consists almost entirely of massive stars with short stellar lifetimes. Regions dominated by evolving AGB stars are populated by intermediate mass stars with present day ages older than the main sequence, but not as old as the targeted RGB stars, which occupy a region dominated by older low mass stars with present day ages > 2.5 Gyr.

We can use stellar population models to estimate average ages for each CMD stellar region (Williams et al. 2014, 2021). In the rest of the paper, we will refer to stars in the AGB region as "intermediate age," and stars in the RGB region as "old." We combine MS stars, blue HeB, and red HeB, and into a single broad age group that we will refer to as "young." Even though the RHeB stars are far to the red, they are put into the young group because we targeted high mass ones with short lifetimes. See Figure 5.3 for the approximate location of each stellar lifetime division for our sample.

After the CMD division, we re-categorize weak CN and carbon stars based their spectroscopic information, regardless of their CMD location. Both the intermediate age carbon and young weak CN stars are identified using a combination of visual inspection and machine classification of stellar spectra; they are discussed in greater detail in Appendix 5.8.1. We assign weak CN stars to the young age group and carbon stars to the intermediate age group because the average age of these stars are consistent with the young and intermediate age group, respectively. We have marked these stars in Figure 5.3 with black outlines to distinguish them from the CMD divisions.

We assign each broad bin an average age using simulated CMDs: $\sim$ 80 Myr for the young stars group; $\sim$ 1 Gyr for intermediate age stars; and $\sim$ 4 Gyr for the old stars. These age averages come from Williams et al. (2021); Smercina & et al. (in preparation) who compare the PHATTER targets to simulated CMDs using Padova isochrones (Marigo et al. 2017). These age ranges are quite broad. The range (16^{th} to 84^{th}) in the young group is $\sim 20 - 180$ Myr, the intermediate age bin spans ages $\sim 0.56 - 2.2$ Gyr, and the old age bin spans $1.4 - 9$ Gyr. (See Williams et al. (2009) for specific star formation histories of regions in M33.) Additionally, these age bins have some overlap and contamination due to the approximate nature of CMD divisions. However, the average ages for each bin are distinct enough to broadly study stellar kinematics as a function of age, which is the goal of this work. We compare the dynamics of these three broad groups and look for trends with stellar age.

5.3.1 Removing Halo Contamination

Gilbert et al. (2022) provide evidence for the existence of a dynamically hot

component in M33, using a subset of the spectroscopic dataset used in this paper. They do not find evidence for this component in their young stellar sample, made up of weak CN stars, which are best described by a single dynamically cold component. The stars of the hot component make up $\sim 22\%$ of the total old sample of the TREX Survey, which we correct for using the model described in Gilbert et al. (2022) to remove likely halo contaminants from the old disk population.

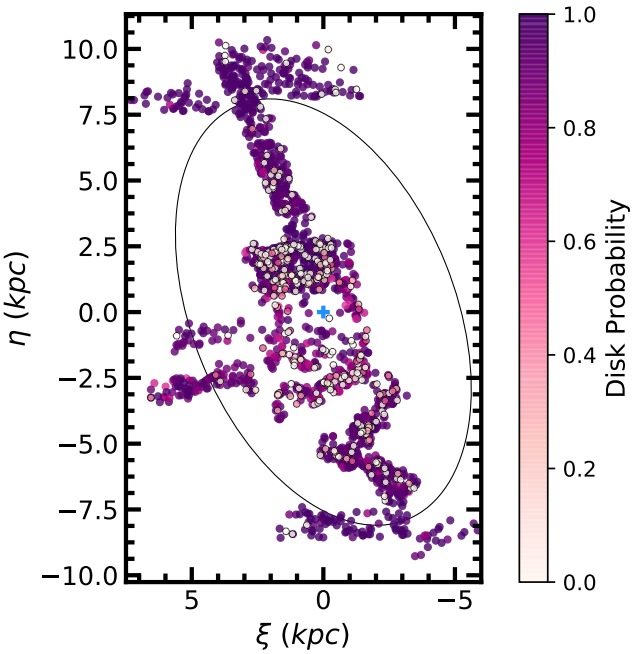

Figure 5.4: Map of the intermediate age and old stars color coded by probability of belonging to a dynamically cold component. The ellipse represents the approximate location of the disk break. The center of M33 is marked with a blue cross.

Gilbert et al. (2022) model the disk and halo assuming a tight kinematic connection to the H I disk. They compare the line-of-sight velocities of stars to the line-of-sight velocity of the H I at the same radius using the titled ring model in Kam et al. (2017), rather than individual H I measurements. They model the disk and halo as

Gaussians in a transformed line-of-sight velocity space defined as the difference between a star's velocity and the calculated line-of-sight velocity of the disk or halo component at the star's disk location, assuming the fractional rotation speed for that component. This allows each component to rotate at a fraction of the speed of the H I disk model. The best fit model from Gilbert et al. (2022) then returns a probability that a given star's kinematics belong to a dynamically cold component. Although the Gilbert et al. (2022) analysis focuses only on the old stars, we see preliminary evidence that the intermediate age population may host a similar component, and thus we apply the same model to remove candidate kinematically hot AGB stars. The model was run separately on the AGB stars utilizing the same model formalism and procedure used by Gilbert et al. (2022) for RGB stars. We use the probability from the model to keep all intermediate age and old stars with velocities that are at least 80% likely to belong to the dynamically cold component, eliminating velocity outliers and producing a more pure disk-like population. We assume all young stars are disk stars. Figure 5.4 shows a map of the intermediate age and old stars color coded by probability their kinematics are consistent with a cold component.

Removing stars with disk probabilities which are $< 80\%$ eliminates $\sim 14\%$ of the initial intermediate age bin and $\sim 23\%$ of the initial old age bin. For the old stars, the percentage of stars eliminated from the disk sample is consistent with the expected fraction of RGB halo stars from Gilbert et al. (2022). Future work, utilizing an increased AGB sample, will characterize the kinematics of the AGB population as a whole and explore the nature of the AGB stars which have velocities well removed

from the M33 disk velocity. In Section 5.5 and 5.6, we explore the implications of not removing possible halo stars.

With the quality cuts and the elimination of old halo stars and intermediate age halo star candidates, our study consists of 952 young stars, 521 intermediate age stars, and 1088 old stars for a total of 2561 stars.

5.4 Stellar Kinematics as a Function of Age

We get line-of-sight velocities for the stars in our sample from the stellar spectroscopic observations. In this section, we describe how we use the line-of-sight velocities to calculate local line-of-sight velocity dispersion, construct rotation curves, and calculate asymmetric drift for each stellar age bin.

5.4.1 Local Velocity Smoothing

We calculate the local velocity dispersion by examining the velocities of neighbors around each star. We start with a $50''$ radius aperture for selecting neighbors and then grow in radius by $5''$ until there are at least fifteen stars of the same broad age bin within the circle. The sizes of the circles used are illustrated in the last column of Figure 5.5. For the young group, the median radius was $85''$, for the intermediate age group the median radius was $120''$, and for the old age group the median radius was $100''$, which is 0.35 kpc, 0.5 kpc, and 0.42 kpc, respectively, at the distance of M33.

If the circle gets to $300''$ and still does not contain fifteen members, we do not calculate a line-of-sight velocity average or velocity dispersion at that location. The

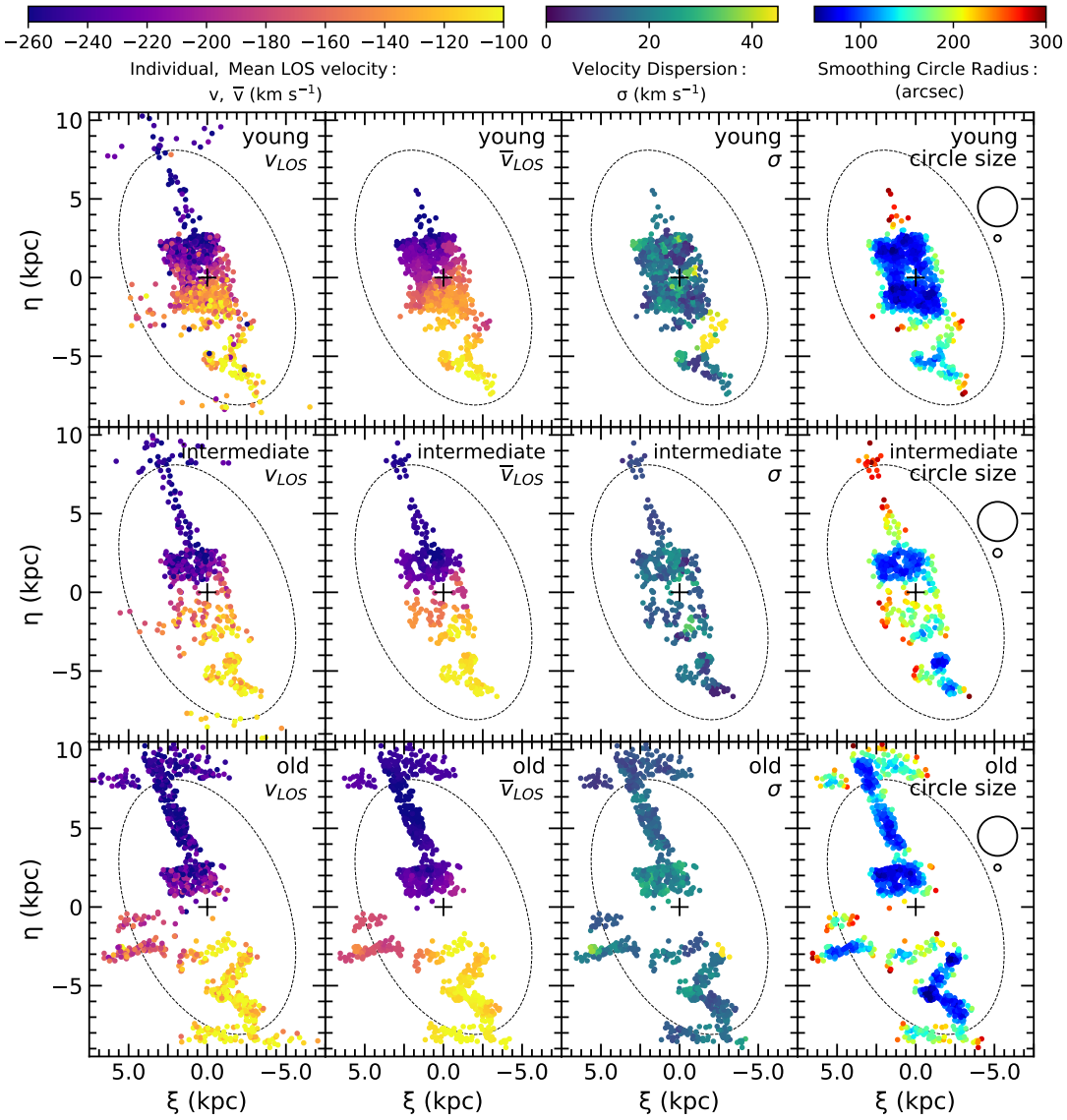

Figure 5.5: Line-of-sight velocity and velocity dispersion as a function of position for the three broad age bins. The top row shows the young stars. The middle represents the intermediate age population, and the bottom row shows the old population. For all rows, the color in the first column represents individual line-of-sight velocity. For the second column, color represents the smoothed line-of-sight velocity. The third column shows the local velocity dispersion. The last column shows the size of the radius of the smoothing circle used at that point. The smallest and largest smoothing circle used are also shown. The ellipse represents the approximate location of the disk break. The center of M33 is marked with a black cross. The inner disk (r $<$ 3.75kpc) has higher velocity dispersion for all age bins, and the young stars show an extended area of high dispersion.

velocity of the skipped star can still contribute to the analysis of its neighbors however. This smoothing technique is similar to that used in Dorman et al. (2015), Quirk et al. (2019), and (Quirk & Patel 2020). After smoothing, we have local velocity dispersion measurements centered on 879 young stars, 462 intermediate age stars, and 1053 old stars.

The resulting velocity maps are shown in Figure 5.5. The second column shows the locally averaged line-of-sight velocities for each age bin. The third column shows the local velocity dispersion, the calculation of which we describe below. The fourth column shows the size of the smoothing circle that was used for each center, along with the size of the smallest and largest smoothing circle used for that age bin.

5.4.2 Velocity Dispersion

We calculate the weighted mean of the line-of-sight velocities and the inverse variance weighted root mean square dispersion (RMSE) of the members (Equation 5.1 and 5.2). In these two equations, the weights are normalized and derived from the velocity measurement errors ($\sigma_{\mathrm{err},i}$ in the following equations) such that, $\sum_{i=1}^{n} w_i = 1$ and $w_i = \sigma_{\mathrm{err},i}^{-2}$. The velocity measurement error model is discussed in Section 5.2.1.

$$\overline{x} = \sum_{i=1}^{n} x_i \times w_i \tag{5.1}$$

$$\sigma_v = \sqrt{\sum_{i=1}^{n} (x_i - \overline{x})^2 \times w_i} \tag{5.2}$$

We use the inverse variance weighted RMSE as the dispersion. We only consider stars of the same age bin in the averaging and dispersion calculation.

Along with local velocity dispersion, we compute the median velocity dispersion for each of the three age bins, which is reported in Table 5.1. We can compare these values to the global models fit from Gilbert et al. (2022), who find a global velocity dispersion of $\sim 16\,\mathrm{km\,s^{-1}}$ for the young stars and $\sim 21\,\mathrm{km\,s^{-1}}$ for the old stars, which is similar to the median local velocity dispersions reported here.

We also show details of the velocity dispersion distributions in Figure 5.6. The left panel shows the median value, interquartile range, and outliers for the three age bins across the full extent of the TREX Survey. Overall, we find that velocity dispersion does not vary strongly with stellar age, as the median values of each population do not vary significantly. Furthermore, the median values of each age bin are relatively low and are roughly twice the average dispersion of the H I (Chemin et al. 2020, 8 $\mathrm{km\,s^{-1}}$). The low magnitude of velocity dispersion and the lack of an increase with stellar age are not expected when compared to expectations from simulations of slightly more massive disk galaxies (Martig et al. 2014) or observations of star clusters in M33 (Beasley et al. 2015). However, these studies do not remove dynamically heated populations that are likely to belong to a halo, so it is not an exact comparison.

Martig et al. (2014) find that the shape of the age-velocity dispersion relation for young and intermediate age stars is dependent on recent merger or other heating activity, whereas the velocity dispersion for the oldest stars is more dependent on birth kinematics. They also find that uncertainties in ages can obscure possible trends in the

Age Group	Mean σ_{LOS} (kms^{-1})
Young	$15.9^{+0.3}_{-0.2}$
Intermediate Age	$15.2^{+0.2}_{-0.2}$
Old	$16.5^{+0.2}_{-0.1}$

Table 5.1: Medians of weighted velocity dispersion as a function of broad age bin. The errors on the median value represent the difference between the 16$^{\text{th}}$and 84$^{\text{th}}$ percentiles divided by $\sqrt{\text{N}}$, where N is the number of stars.

age-velocity dispersion relation. Since the age bins in this work are broad, we could be missing a more subtle trend, but this would not explain the low magnitudes.

While the medians of the distributions are similar, the distributions themselves are broad enough that they may be widened by trends with radius. In the right panel of Figure 5.6, we show the distributions of velocity dispersion for each age group broken into an inner ($r < 5$ kpc) and outer ($r < 5$ kpc) subgroup. For all age bins, the distribution of velocity dispersion shifts lower in the outer region compared to in the inner region, although the median velocity dispersion for the young stars is higher in the outer region. The number of outliers is higher in the inner region for the young and intermediate age stars.

We look more closely at velocity dispersion as a function of radius in Figure 5.7, which shows the distributions of velocity dispersion and radius. There is a clear downward trend in the intermediate age and old stars populations as one goes out to greater radii. This suggests the outer disk is dynamically cooler than the inner disk, which is consistent with the findings of Gilbert et al. (2022) and disk galaxies in general (e.g. Bottema 1993). Koch et al. (2018) find that the velocity dispersion of the H I decreases by ~ 2 km s^{-1}from the center of M33 to $\sim r = 8$ kpc. For the young stars, any trend is less clear because of the extended area of high dispersion, which we examine

below, however there is a slight trend of increasing velocity dispersion with radius.

Although there is not much trend between velocity dispersion and age, there is an extended area of extreme velocity dispersion for the youngest group of stars. Figure 5.5 shows this extended area of high velocity dispersion in the young star population. We examined this anomalous region in detail to test if the substructure is real or potential velocity measurement artifact. First, we looked at young stars with extreme velocities that contribute to the high velocity dispersion in this extended region. Their velocities are well measured and pass our quality cuts. Secondly, this region is also not dominated by the largest size smoothing circle. Because of this, we think the areas of high velocity dispersion in the young stars are real effects and will investigate it further using duplicate velocity measurements as future work. A smaller portion of this same

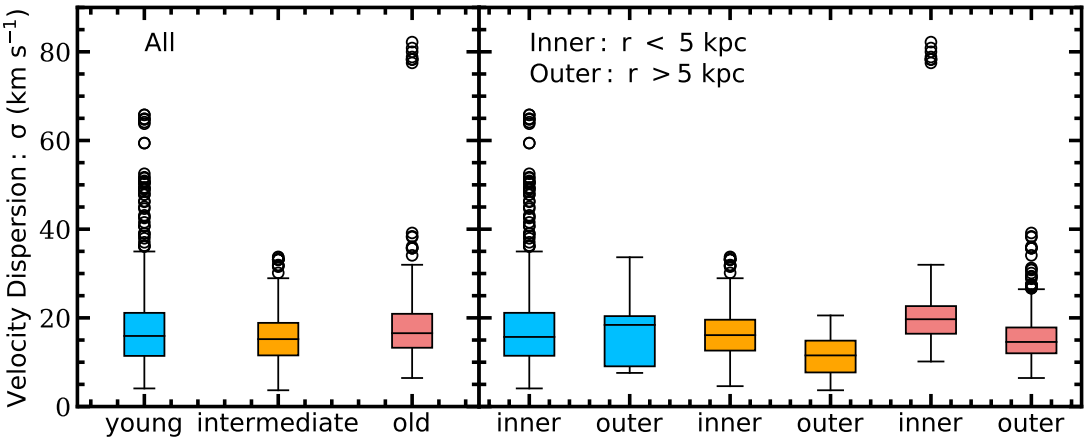

Figure 5.6: Velocity dispersion distributions for the three age bins. The left panel shows the distributions for the full final population. The right panel shows each age bin divided into an inner ($r < 5$ kpc) subgroup and an outer subgroup ($r > 5$ kpc). For all boxplots, the shaded box represents the interquartile range, the horizontal line across the box represents the median, and the open circles show the outliers. The outliers are stars with a velocity dispersion that are at least 1.5 σ from the first or third quartile value, which is the distance marked by the whiskers. Velocity dispersion does not vary significantly with stellar age and is on average higher in the inner region.

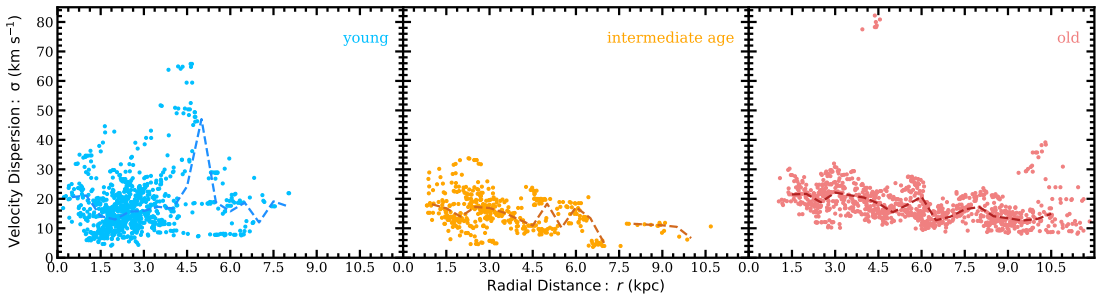

Figure 5.7: Velocity dispersion as a function of deprojected radius for the young, intermediate age, and old populations. Median lines are also plotted. For the intermediate and old age bins, velocity dispersion is higher in the inner regions than in the outer regions. The old stars show one concentrated area of extreme velocity dispersion, while the young stars show an extended area of high dispersion, and the intermediate age stars show no high velocity dispersion. The area of extreme velocity dispersion for the old stars is overlapped with an area that also has extreme velocities for the young stars.

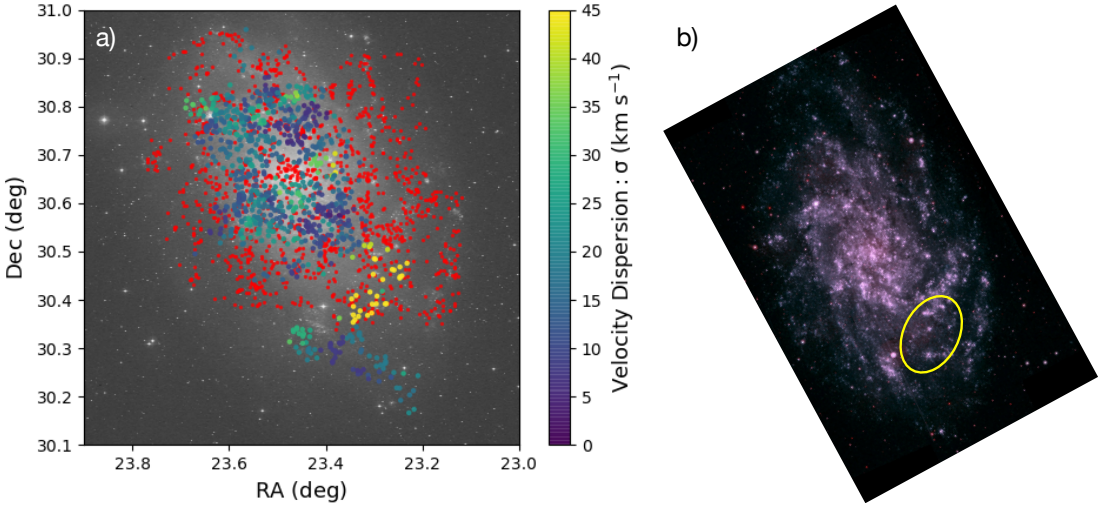

Figure 5.8: Velocity dispersion as a function of position for the young stars. Panel a) shows the young stars overplotted on an image of M33 from the DSS. The color of the points corresponds to velocity dispersion. The smaller red points mark H II regions (Hodge et al. 1999). Panel b) shows a UV image of M33 from the Swift Observatory (image credit: NASA/Swift/Stefan Immle) with a yellow ellipse showing the approximate location of the high velocity dispersion. (The DSS map is slightly enlarged compared to the image of M33 on the right.) These locations do not have higher concentrations of UV emission than other parts of the disk.

area is also coincident with high velocity dispersion for the old stars that do have well characterized velocity measurement errors.

We also compare the location of the high velocity dispersion region to a UV map of M33 in Figure 5.8. The yellow ellipse in the right panel shows the approximate location of the extended area of high velocity dispersion with respect to the UV emission. Because there is ongoing star formation across the disk, there does not appear to be anything notable about the specific high dispersion area and no correlation between stellar velocity dispersion and whether a location is UV dark or UV light. The left panel shows velocity dispersion as a function of position compared to H II regions from Hodge et al. (1999). There also does not seem to be anything coincident about the H II regions around the high stellar velocity dispersion.

Koch et al. (2018) examine the atomic ISM across the disk of M33 and find a filament of H I that extends to 8 kpc across the southern disk (see their Figure 18). While the filament overlaps the area of high velocity dispersion reported here, the young velocity dispersion is coincident with a void in the filament. It is further unlikely that the filament is related to the high stellar velocity dispersion because the line-of-sight velocities of the young stars would need to be blueshfited by > 30 km s^{-1}, which they are not. There are some localized bright areas of H I with broad line widths that are close to the area of high velocity dispersion shared by the young and old stars, but it is unclear if they are related to the high stellar dispersion.

It is possible that other phenomenon are causing the high velocity dispersion in the young stars and small number of old stars. For example, there could be unmarked

massive gas clouds or a significant number of stellar binaries. Additionally this area could contain substructure from a relatively recent minor merger that lies in front of the disk. If M31 and M33 did have an interaction in the past, perhaps the interaction could have increased the dispersion of the H I and young stellar disk.

5.4.3 Rotation Curves

We use the weighted average line-of-sight velocities to calculate the rotation velocities of the stars, which we compare to the rotation velocities of gas tracers such as H I, CO, and Hα. To calculate the rotation velocity, we convert the line-of-sight velocity to a circular velocity using the tilted ring model described in Kam et al. (2017). Kam et al. (2017) divide the H I disk of M33 into forty-nine annuli from $r = 0'$ to $r = 96'$ and measure the position angle (PA) and inclination (i) of each annulus, as tabulated in Table 4 of their paper. The rings in Kam et al. (2017) have a width of $0.2'$. We interpolate this table to create thinner rings. We then calculate a star's deprojected distance from M33's center using the PA and i of M33. With that distance, we match the star/gas measurement to a tilted ring from the interpolated table and assign it the corresponding ring's PA and i. We recalculate the deprojected distance, and reassign the star/gas measurement to another ring if needed. We repeat this process twice before adopting the final PA and i for the star/gas measurement.

$$v_{\rm rot} = \frac{v_{\rm LOS} - v_{\rm sys}}{\cos(\theta)\sin(i_{TR,\star})} \tag{5.3}$$

The above equation projects a star onto a circular orbit. We use $v_{sys} =$

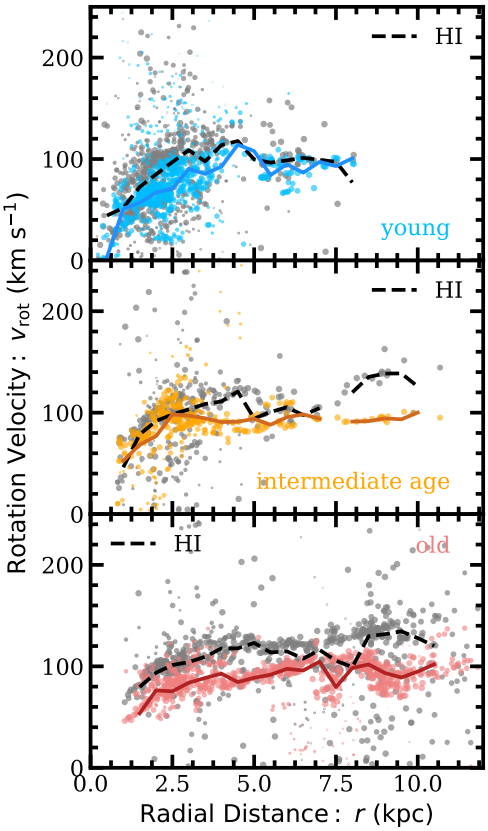

Figure 5.9: Rotation velocity as a function of deprojected radius. Rotation velocities are calculated with the tilted ring model in Kam et al. (2017) (Equation 5.3). The top panel shows the youngest age bin (light blue), the middle panel shows the intermediate age group (orange), and the bottom panel shows the old group (red). Each star has been paired with a H I velocity measurement along the same line-of-sight, and the gas is represented by the grey dots. The size of the points is proportional to the $\cos(\theta)$ factor in Equation 5.3 to illustrate the limitations of the equation around the minor axis. The solid (dotted) line shows the median rotation velocity for 0.5 kpc bins for the stars (H I). The deprojection effects around the minor axis cannot explain the full amount of scatter, especially for the gas.

-180kms^{-1} (Kam et al. 2017). Theta is the azimuthal angle in the plane of M33, and i is the inclination that comes directly from matching a star/gas measurement to a tilted ring. Theta is calculated with $\theta = \beta \times [\alpha \cos(i_{TR})]^{-1}$ where $\alpha = \eta \cos(\text{PA}_{TR}) + \xi \sin(\text{PA}_{TR})$ and $\beta = \xi \cos(\text{PA}_{TR}) - \eta \sin(\text{PA}_{TR})$. We use the assigned PA of the ring

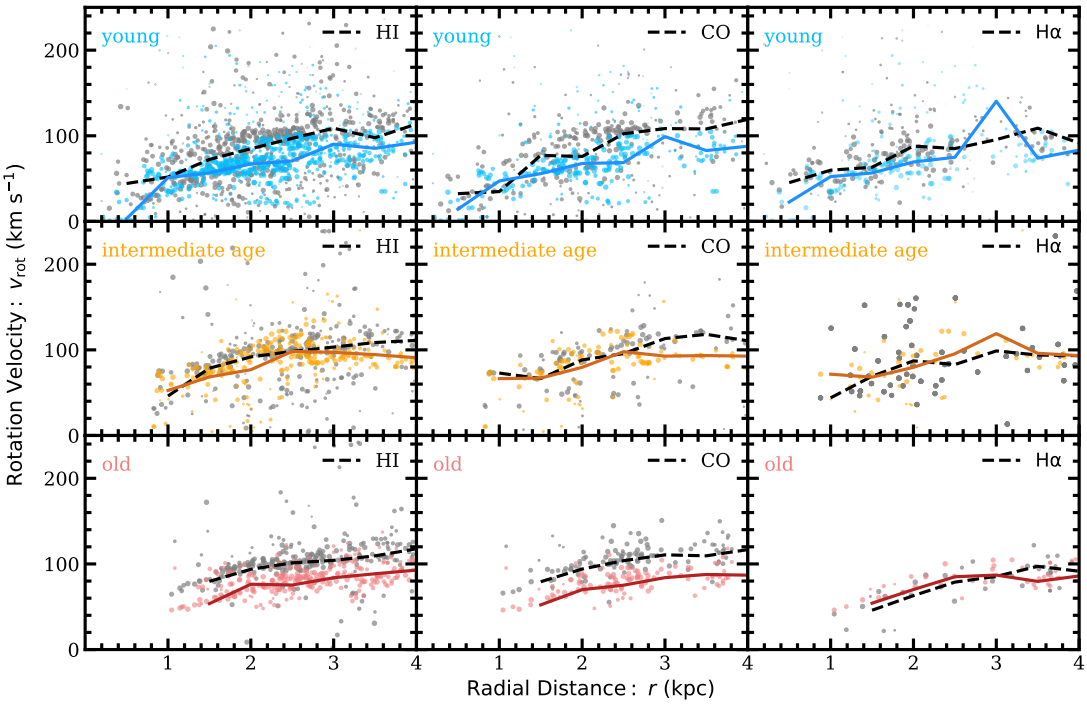

Figure 5.10: Rotation velocity as a function of deprojected radius for the inner 4 kpc of the disk. Rotation velocities are calculated with the tilted ring model in Kam et al. (2017) (Equation 5.3). The top row shows the youngest age bin (light blue), the middle row shows the intermediate age group (orange), and the bottom row shows the old group (red). Each star has been paired with a H I (first column), CO (second column), and Hα (third column) velocity measurement along the same line-of-sight, and the gas is represented by the grey dots. The size of the points is proportional to the cos(θ) factor in Equation 5.3 to illustrate the limitations of the equation around the minor axis. The solid (dotted) line shows the median rotation velocity for 0.5 kpc bins for the stars (gas). The deprojection effects around the minor axis cannot explain the full amount of scatter, especially for the gas. The bar is believed to extend to 0.5 kpc (Williams et al. 2021; Smercina & et al. in preparation; Lazzarini & et al. in preparation).

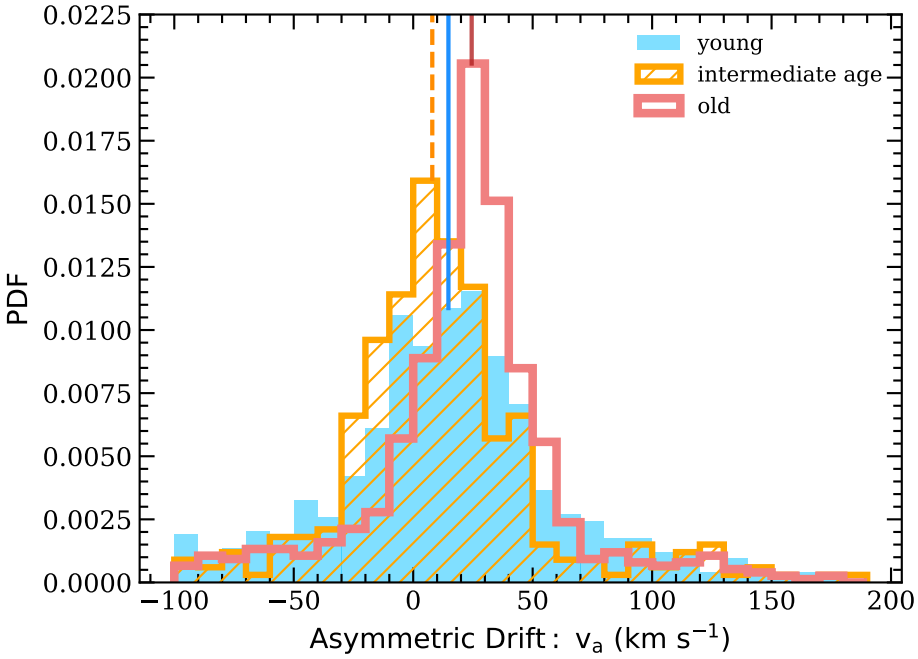

Figure 5.11: Asymmetric drift distributions for the young stars (blue solid), intermediate age (orange hatched), and old star (red outline). AD is calculated with respect to the H I using $v_a = v_{\rm rot,\ gas} - v_{\rm rot,\star}$. The medians are marked by the vertical lines that run from the peak of the corresponding distribution to the top of the plot. There is no clear trend between AD and stellar age, except that the width of the distribution decreases with stellar age.

that a star/gas measurement lies in and the deprojected coordinates of the star/gas measurement centered on M33. Since each star is paired with a gas measurement, the star and the gas measurement share the same deprojected geometric parameters but can have different values for rotation velocities, as they have different line-of-sight velocities.

With the above equations, we construct a rotation curve for each of our broad stellar age bins. The three rotation curves are shown in Figure 5.9. These rotation curves show the rotation velocity as a function of deprojected radius for the three stellar age bins and for the H I along the same line-of-sight of each star for the full extent of the TREX Survey. We also plot the inner rotation curves compared to the CO and Hα

datasets, which do not extend beyond 4 kpc so are not shown in the full rotation curve. These inner rotation curves are plotted in Figure 5.10 for the inner 4 kpc for the three age bins and H I, CO, and Hα.

In both Figures 5.9 and 5.10 it is clear that the rotation curves of both the stars and the gas show significant scatter. Quirk et al. (2019) demonstrate the deprojection factor of the tilted ring model, or the denominator, approaches zero along the minor axis, regardless of inclination because of the $cos(\theta)$ factor, which can explain some but not all of the scatter in the rotation curves. Other sources of scatter in the stellar rotation curves could be from poorly measured velocities, particularly in the young stars, or disturbances from M33's bar (Williams et al. 2021; Smercina & et al. in preparation; Lazzarini & et al. in preparation) and spiral arms. Scatter in the gas rotation curves could reflect the impact of star formation or turbulence in the ISM. The amount of scatter in the stellar rotation curves is largest for the youngest group and decreases with stellar age, which suggests M33's high star formation rate could be causing turbulence not only in the gas but also in the birth kinematics of stars born from that gas. This could also be causing some of the extreme velocities in the young stars.

To quantify the scatter, we have added median lines to each stellar and gas rotation curve and have made the marker size proportional to the $cos(\theta)$ factor. The scatter cannot entirely be attributed to deprojection effects along the minor axis, especially for the gas, which appears to have the most scatter away from the minor axis. We used binning of 0.5 kpc to remove likely outliers while preserving local discrepancies for the median lines. Any velocity difference between the stellar and gas rotation curves

is a visual representation of asymmetric drift and will be explored further in the next section.

5.4.4 Asymmetric Drift

We use the stellar and gas rotation curves in Figures 5.9 and 5.10 to calculate the asymmetric drift (AD or v_a) of the three broad age bins. Often, AD is defined as the difference between the circular velocity derived from the potential of a galaxy and the rotation velocity of the stars (Strömberg 1946). For the purpose of this study, we define AD to be the difference between the rotation velocity of the gas and that of the stars (Quirk et al. 2019; Quirk & Patel 2020). This choice allows us to make local and empirical AD measurements without relying on models of the potential of M33.

AD measurements can be used to measure dynamical heating (Quirk et al. 2019), as gas, which is collisional, can fairly easily dissipate energy and maintain a low energy orbit (Sellwood & Moore 1998), while stars retain a non-circular orbit if they have been perturbed onto an eccentric orbit (Leaman et al. 2017; Sellwood & Binney 2002). In M31, observed AD compared to that in simulated IllustrisTNG-100 M31-like analogs has provided evidence that M31 experienced a relatively recent major merger (Quirk & Patel 2020). In our own galaxy, AD is routinely used to correct the local standard of rest and to predict rotation curves outside the solar neighborhood before Gaia (Golubov 2014; Huang et al. 2016).

For every star and gas measurement pair, we calculate an AD value, v_a, from their respective rotation velocities, using $v_a = v_{\mathrm{rot,\ gas}} - v_{\mathrm{rot},\star}$. We make AD measurements with respect to H I, CO, and Hα. (This equation is in rotation velocity space,

Age Group	AD w.r.t H I (kms^{-1})	Width (kms^{-1})	Outliers %
Young	$15.1^{+1.6}_{-1.7}$	73.3	3.2
Intermediate Age	$8.0^{+1.7}_{-1.6}$	68.2	5.8
Old	$24.5^{+0.9}_{-1.1}$	51.1	3.7

Table 5.2: Stats for the distribution of AD for the three age bins with respect to H I for the full extent of the survey. Median values of AD, width (sigma) of the distribution, and the percentage of outliers in the distribution are shown. The errors on the median value represent the difference between the $16^{\text{th}}$and 84^{th} percentiles divided by $\sqrt{\text{N}}$, where N is the number of stars. The outliers are stars with a velocity dispersion that are at least 1.5 σ from the first or third quartile value.

whereas the offset used in Gilbert et al. (2022) for halo star identification is in line-of-sight space.) The CO and Hα measurements only exist for the inner $\sim$ 4 kpc so we calculated AD in the inner regions with respect to all three kinds of gas but only with respect to H I for the full survey extent (or out to $\sim$ 11 kpc). The distribution of these values are plotted in Figure 5.11 and 5.12, and the median values, width of the distributions, and percentage of outliers are listed in Table 5.2 and 5.3. The outliers are stars with a velocity dispersion that are at least 1.5 σ from the first or third quartile value.

Age Group	AD w.r.t H I (kms^{-1})	Width (kms^{-1})	Outliers %	AD w.r.t CO (kms^{-1})	Width (kms^{-1})	Outliers %	AD w.r.t Hα (kms^{-1})	Width (kms^{-1})	Outliers %
Young	$16.8^{+1.8}_{-1.9}$	72.0	2.7	$18.9^{+2.2}_{-3.0}$	70.6	3.2	$9.8^{+2.4}_{-2.6}$	64.0	3.9
Intermediate Age	$5.9^{+1.6}_{-1.7}$	65.7	8.3	$6.0^{+2.4}_{-2.7}$	49.0	3.6	$-10.0^{+8.5}_{-4.3}$	72.7	3.6
Old	$23.3^{+1.0}_{-1.4}$	38.1	6.4	$26.0^{+1.3}_{-1.3}$	17.4	0.9	$-3.4^{+3.5}_{-3.3}$	21.8	0.0

Table 5.3: Stats for the distribution of AD for the three age bins with respect to H I, Hα, and CO for the inner 4 kpc. Median values of AD, width (sigma) of the distribution, and the percentage of outliers in the distribution are shown. The errors on the median value represent the difference between the $16^{\text{th}}$and 84^{th} percentiles divided by $\sqrt{\text{N}}$, where N is the number of stars. The outliers are stars with a velocity dispersion that are at least 1.5 σ from the first or third quartile value.

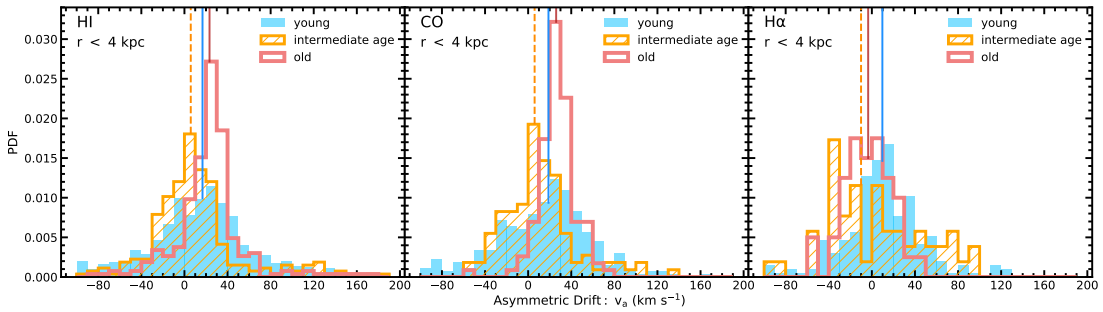

Figure 5.12: AD distributions for the young stars (blue solid), intermediate age (orange hatched), and old groups (red outline) for the inner 4 kpc. AD is calculated with respect to the H I (left panel), CO (middle panel), and Hα (right panel) using $v_a = v_{\mathrm{rot,\ gas}} - v_{\mathrm{rot},\star}$. The medians are marked by the vertical lines that run from the peak of the corresponding distribution to the top of the plot. On average, the young and old stars have similar median AD values, suggesting there is no trend between AD and stellar age. For the Hα, the gas is lagging the intermediate age and old stars, resulting in a negative AD, but both AD values are consistent with zero within 1σ.

For the H I and CO, the intermediate stars show the lowest AD values, so there is no monotonic trend with stellar age. When compared to Hα, the intermediate age stars have the greatest offset in the rotation velocity of the gas and stars; however, this difference is barely larger than 1σ so is not robust. Furthermore, the median AD values are negative for the intermediate age and old stars, which means that on average, the Hα is lagging behind the stars and therefore the stars could be more settled on a circular orbit than the Hα. However, both of these AD values are consistent with 0 within 1σ. We expect AD to increase with stellar age (e.g., Sellwood & Binney 2002; Westfall et al. 2007; Gaia Collaboration et al. 2021; Quirk et al. 2019), so seeing a high magnitude of AD in the young stars suggests there is something perturbing the young stars on short timescales, which resulted in their kinematics diverging from the gas.

Overall, the old stars tend to have the greatest magnitude of AD, but the distributions of AD values are narrower. In the inner 4 kpc, the young and intermediate

age stars have the largest widths, that are at times double that of the old stars for each of the three types of gas used in calculating AD, which is the opposite of what is expected for a canonical model of steady dynamical heating of stars. The old stars are thus more systematically offset from the nearby gas in terms of the kinematics, whereas the young and intermediate stars are more randomly offset from the kinematics of the nearby gas. Over the full radial range, even though the young stars still have the widest AD distribution, the three groups of stars have more similar widths. This suggests the stars in our sample are most similar between radii 4 an 11 kpc.

The percentage of outliers (stars with AD values that are 1.5σ or greater away from the 16^{th} or 84^{th} percentiles) in each distribution shows no clear pattern with median AD, width of the distribution, or stellar age. The intermediate age stars have the highest percentage of outliers in the distribution of AD values calculated with respect to H I in the inner 4 kpc.

It is important to note that the three gas datasets used come from different telescopes and were reduced using different methods. Subtle differences in the derivation of the gas velocity measurement could be causing variations in the AD median values, not just physical phenomena. However, subtle differences would systematically affect the three age bins equally, which means these potential differences cannot be obscuring a lack of trend between age and asymmetric drift.

In summary, M33 does not show the expected increase in AD with stellar age because of the low AD of the intermediate age stars and the high AD value for the young stars. The distributions of AD get narrower with stellar age, showing that the

younger stars are more randomly offset from the gas than the older stars.

5.5 Comparison to IllustrisTNG

We analyze M33-like analogs from the IllustrisTNG50-1 cosmological simulation to comment on the uniqueness of the results presented above. The IllustrisTNG Project is a suite of N-body and hydrodynamic simulations from redshift $z = 127$ to $z = 0$. It uses the `AREPO` moving-mesh code (Marinacci et al. 2018; Naiman et al. 2018; Springel et al. 2018; Pillepich et al. 2018; Nelson et al. 2018; Springel 2010). The simulations have a cosmological volume of $(51.7\ \mathrm{Mpc})^3$ and have the following initial cosmological parameters from Planck Collaboration et al. (2016): $\Omega_m = 0.3089$, $\Omega_\Lambda = 0.6911$, $\Omega_b = 0.0486$, $\sigma_8 = 0.8159$, $n_s = 0.9667$, and $h = 0.6774$. For our analysis, we adopt a value of $h = 0.704$ (WMAP-9; Hinshaw et al. 2013).

We use data from the IllustrisTNG50-1 simulation (hereafter IllustrisTNG), the smallest but highest resolution simulation in the project that includes both dark matter and baryons. IllustrisTNG follows the evolution of 2160^3 dark matter particles and 2160^3 hydrodynamical cells, resulting in a a baryonic mass resolution of $m_{\mathrm{bary}} = 8.1 \times 10^4\ M_\odot$ and a dark matter particle mass resolution of $m_{\mathrm{DM}} = 4.4 \times 10^5\ M_\odot$. Halos and subhalos are identified using `SUBFIND` (Springel et al. 2001; Dolag et al. 2009).

We identify general M33-like analogs as halos that fit the following criteria: the subhalo is the central/primary subhalo at $z = 0$ in Friend of Friend (FoF) group with a virial mass of $M_{\mathrm{vir}} = 1 - 2.5 \times 10^{11} M_\odot$ (Patel et al. 2018, and references within); the subhalo has a stellar mass of $M_\star = 2.8 - 5.6 \times 10^9 M_\odot$ (Guo et al. 2010), and the

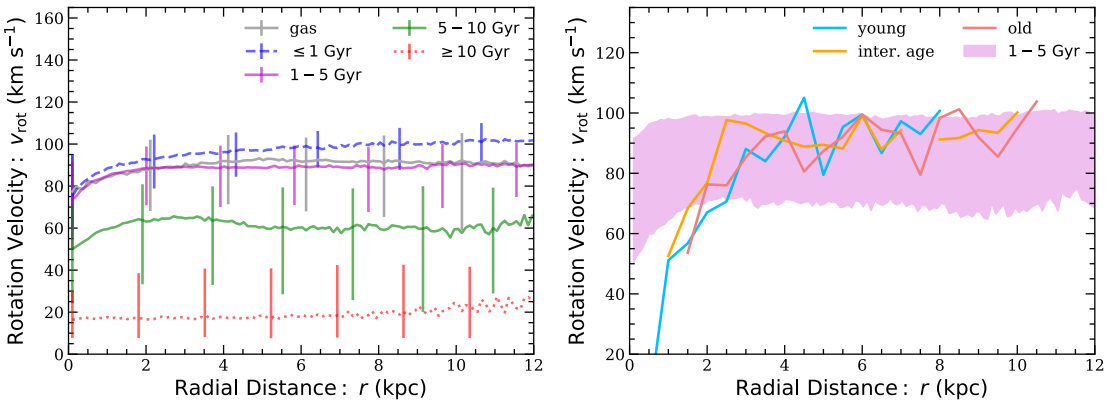

Figure 5.13: Cumulative stellar rotation curves for the 216 M33-like analogs from the IllustrisTNG50-1 simulation and the observations presented in this analysis. Left panel: The grey line represents the gas cells, the blue dashed line represent star particles with ages < 1 Gyr, the purple line represents star particles with ages 1-5 Gyr, the green line represents star particles with ages 5-10 Gyr, and the red dotted line represents star particles with ages > 10 Gyr. The vertical bars represent the width of the distribution ($16^{\text{th}} - 84^{\text{th}}$ percentile) of rotation velocities in a given radial bin. The median rotation velocities of the 0.1 kpc radial bins are shown. Right panel: The magenta filled region represents stellar particles with ages 1-5 Gyr. The width of the filled regions represent the width of the distribution ($16^{\text{th}} - 84^{\text{th}}$ percentile) of rotation velocities in a given radial bin. The observed M33 rotation curves for the three age bins are plotted on top. The observations are consistent with stellar particles ages 1-5 Gyr, which are a similar age to the observed sample.

subhalo's maximum dark matter particle circular velocity is $< 70\,\mathrm{km\,s^{-1}}$. These cuts produce a sample of 224 analog galaxies. We eliminated eight of these due to lack of baryon particles across the inner 10 kpc, leaving 216 M33-like galaxy analogs.

For each analog, we rotate the particles/gas cells to be face-on so that the "line-of-sight" direction is the z component for all analogs. We exclude particles with $|z| > 10$ kpc and with a galactic radius of > 20 kpc to target star particles that likely belong to the disk. We then locally average the velocities to mimic the resolution from observations, following Section 3 of Quirk & Patel (2020). We divide the stellar particles into four groups based on exact stellar age: < 1 Gyr, 1-5 Gyr, 5-10 Gyr, and > 10 Gyr.

Unlike the rough age division used for the observational part of the analysis, these age bins use a star particle's exact age and spans the full cosmological time. We use the gas cells to calculate AD for each age bin as well.

For each analog, we use the smoothed kinematics to construct an azimuthally averaged rotation curve using the equations below.

$$v_{rad} = \frac{x \cdot v_x + y \cdot v_y}{\sqrt{x^2 + y^2}} \tag{5.4}$$

$$v_{tot} = \sqrt{v_x^2 + v_y^2} \tag{5.5}$$

$$v_{rot} = v_{tan} = \sqrt{v_{tot}^2 - v_{rad}^2} \tag{5.6}$$

We limit the analysis to the 2D xy plane to mimic the observed line-of-sight velocities. We choose to azimuthally average the rotation curve for each. To azimuthally average the rotation curves, the particles/cells are placed into 0.1 kpc bins based on their distance from the center of the analog. We then take the median of the rotation velocities in each bin for the final rotation curve. This process creates a rotation curve similar to the median lines shown in Figures 5.9 and 5.10.

To calculate a single set of rotation curves and median AD values as a function of stellar age for the entire analog sample, we first calculate both the rotation curve and AD for each individual analog, as described above. Since the rotation curves are radially binned, the cumulative rotation curve for the entire sample of analogs is made by using

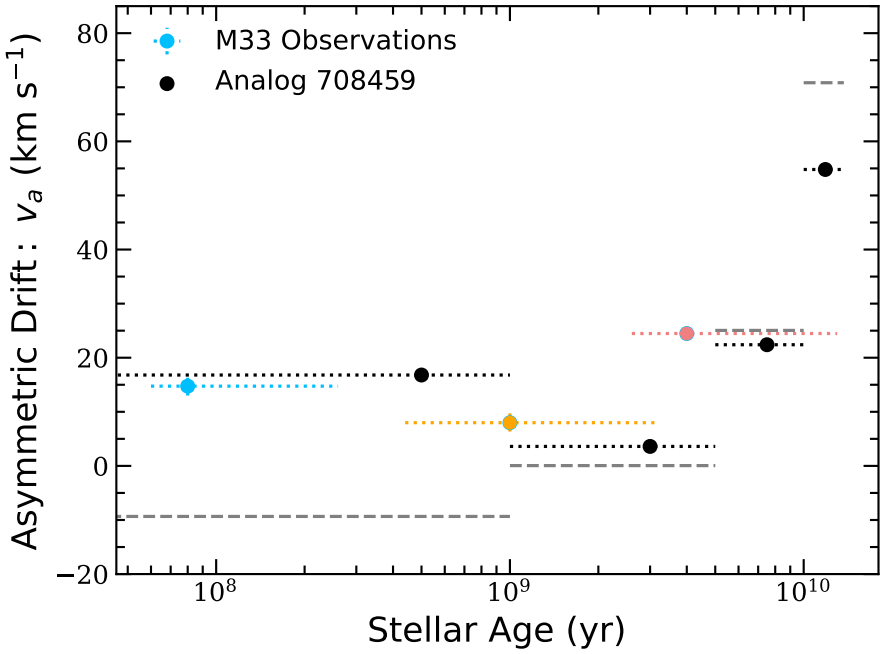

Figure 5.14: Cumulative median AD measurements for M33-like analogs and for observations of young, intermediate age, and old stars in the disk of M33. The shaded grey regions represent the median AD and the widths of the distribution ($16^{\text{th}} - 84^{\text{th}}$ percentile) of the AD for the analogs. The color points represent the median AD for the young (blue), intermediate age (orange), and old (red) stars. The black points represent the analog with AD values closest to what is observed. Compared to the whole sample of analogs, the AD from observations is significantly higher for the youngest stars, than that is seen in the simulated analogs.

the median rotation velocity for each stellar particle age group at each radial bin. We calculate AD values for the entire sample using this cumulative rotation curve. The set of cumulative rotation curves is shown in the left panel of Figure 5.13. Also shown in this figure are the median rotation curves for the observed M33 young stars, intermediate age stars, and old stars in the right panel.

The set of observed M33 rotation curves is consistent with the rotation curves for star particles with ages $1 - 5$ Gyr from the simulated analogs. However, these rotation curves are not a perfect comparison, as the observational one comes from a tilted ring model, and the simulated ones come from calculating the actual tangential velocity of the stellar particles.

The cumulative AD values for the simulated M33 analogs as a function of stellar particle age are shown in Figure 5.14 along with the observational median M33 AD measurements. For the simulated analogs, AD increases with stellar age. A gradient in AD with stellar age is also seen in M31-like simulated analogs in the same simulation (Quirk & Patel 2020). There is no such gradient in the observed AD in M33.

For the young and intermediate age stars, the observed AD is higher than what is seen in simulated M33-like analogs. The AD for the oldest stars is consistent within the observed age errors. While some of the differences in the observed M33 AD and the simulated analogs AD is most likely from the differences in the way AD is calculated for each, it is likely that this would affect all of the age bins equally. Thus, the difference in AD between the observed intermediate and the simulated analogs could be a nonphysical systematic offset. However, the observed young stars have an AD value

that is more offset from the AD of simulated analogs than the offset for the other two age groups. Thus even if there is a systematic offset, the young observed stars still break the gradient in age and AD that is seen in the simulated M33-like analogs.

The high AD observed in the young stars in M33 suggests that some phenomenon is dynamically heating the young stars. Of the M33-like analogs, seven have young stars with an AD greater than 10 $\mathrm{km\,s^{-1}}$. Six have young star AD values between 12 and 19 $\mathrm{km\,s^{-1}}$, and one has an AD value of 33 $\mathrm{km\,s^{-1}}$for the young stars. Of these seven, four have AD distributions that are similar for all stars 0-10 Gyr (the age bins that best represent the observed bins). For three analogs, the intermediate age stars (1-5 Gyr) have the lowest AD. Upon visual inspection of the star and gas particles used in these analogs, only one analog shows a slight disturbance in the disk, and only one has had any mergers (minor or major) in the past 4 Gyr. Thus, there is no immediate connection between these analogs that could point towards a cause of the high AD in the young stars. Figure 5.14 shows the AD values for the analog that is closest to the observed AD values. This analog has not had any mergers within the past 4 Gyr and does not show a disturbance or asymmetry in its disk. Closer inspection of the stellar assembly history of this analog is future work.

The observed sample of stars and the sample of simulated star particles are meant to exclude possible halo stars. However, halo cuts for each are different, and those for the simulated star particles were not based on a kinematic model. Including all halo stars roughly doubles the AD value for the intermediate age and old bins (see Section 5.6 and Table 5.6). It is possible that the gap between the AD in the observations and

the simulated M33-like analogs is larger for the intermediate age and old stars, but even if the simulated AD halved for the older bins, the largest gap would still be for the young stars.

5.6 Discussion: Contextualizing M33 in the Local Group

Resolved stellar spectroscopy of individual stars allows us to study a galaxy in detail. For example, one can examine dynamics as a function of age, spatial position, and metallicity, which puts narrow constraints on origin and evolution. Studies of this kind have already proved valuable for the comparative evolution of the LG's two massive spirals, M31 and the MW. In spite of having similar masses ($M_{\rm vir} \approx 10^{12}\ M_{\odot}$), the disk kinematics of the MW and M31 differ significantly. The MW has thin disk stars, while the majority of disk stars in M31 belong to a thick disk or kicked up disk (Dorman et al. 2013; Dalcanton et al. 2015), with all the analysis pointing towards M31 having a more violent merger history than the MW (e.g. Tanaka et al. 2009; Mackey et al. 2019; Ferguson & Mackey 2016).

Leaman et al. (2017) use data from the literature to compare the age-velocity dispersion relation of eight LG members, including the MW, M31, the LMC, and M33 to model the evolving interstellar medium (ISM) turbulence as a galaxy experiences heating from various sources. In this section, we focus on the observed velocity dispersion of the three most massive LG members and add measurements for M33 that include a robust sample of individually resolved stars across the inner and outer disk of M33. We also present the first comparison of AD as a function of stellar age of LG members.

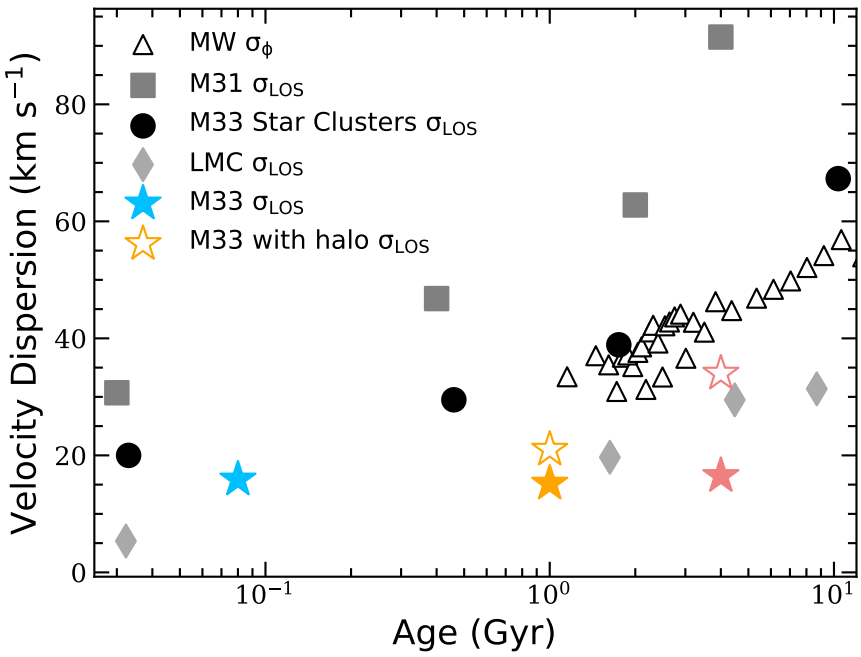

Figure 5.15: A comparison of velocity dispersion as a function of stellar age for the MW (Nordström, B. et al. 2004, black triangles), M31 (Dorman et al. 2015, black squares), M33 star clusters (Beasley et al. 2015, open circles; data later used by Leaman et al. (2017)), the LMC (Cole et al. 2005, grey diamonds), and M33 (this work, stars). The open stars show the velocity dispersion for intermediate age and old stars in M33 if halo candidates are not removed. For M31 and M33, the velocity dispersion is in the line-of-sight, whereas for the MW, the azimuthal component of velocity dispersion is shown. The MW measurements are also in the solar neighborhood, while the measurements of M31 come from across the northern disk, and those from M33 come from across the entire disk. The MW and M31 show a clear increase in velocity dispersion with stellar age. M33 star clusters also show this increase, but the data from this work does not. Additionally, the magnitude of velocity dispersion from this work is much lower than that seen in the M33 star clusters.

It is important to note that possible halo stars were not removed from the M31 velocity dispersion or AD analysis. Dorman et al. (2012) find that $\sim 15\%$ of stars in the M31 sample are part of a dynamically hot component. Dorman et al. (2013) characterize the bulge, disk, and halo of M31 using the luminosity function of stars from the PHAT survey, line-of-sight velocities of RGB stars from the SPLASH survey, and surface brightness profiles. Using these criteria, Dorman et al. (2013) find that the hot component in the M31 sample is best described by a disk-like surface brightness profile and luminosity function but spheroid-like kinematics, suggesting that $\sim 30\%$ of the dynamically hot stars belong to a kicked up disk and $\sim 10\%$ of the M31 sample is halo contamination. Since Dorman et al. (2013) did not fit for a both a disk and a kicked up disk along with a halo component, it is possible that the halo contamination is lower.

The MW data presented here consists of nearby F and G dwarf stars in the Solar Neighborhood that were targeted using Hipparcos parallaxes as part of the Geneva-Copenhagen Survey (Nordström, B. et al. 2004). Nordström, B. et al. (2004) use kinematics to identify thick disk stars and distances to target nearby stars but do not formally remove possible halo stars. The MW halo fraction in the Solar Neighborhood is very small (0.15% Du et al. 2018), so it is possible the sample contains few halo stars but unlikely that these bias the velocity dispersion measurements significantly. The LMC stars come from the optical bar, so there is unlikely to be significant halo contamination (Cole et al. 2005).

It was important for this work to remove possible M33 halo stars because M33's

halo is centrally concentrated and dense, so there is more overlap between the halo and disk stars' sightlines, giving a larger halo fraction in the RGB stars in M33. For the sake of comparison, though, we show the median velocity dispersion and AD values for M33 if halo stars are not removed. We also acknowledge there is not necessarily a clear distinction between a galaxy's halo and kicked up disk, even if they were formed from different mechanisms and that differentiating between a disk, kicked up disk, and a halo can be arbitrary.

Figure 5.15 shows velocity dispersion as a function of stellar age for the MW solar neighborhood (Nordström, B. et al. 2004; Holmberg, J. et al. 2009), the northern disk of M31 (Dorman et al. 2015), star clusters in M33 (Beasley et al. 2015), stars within the optical bar of the LMC (Cole et al. 2005), and stars in the disk of M33 (this work). M31 has both a greater velocity dispersion (Nordström, B. et al. 2004; Holmberg, J. et al. 2009; Sysoliatina, K. et al. 2018; Dorman et al. 2015; Budanova et al. 2017) and a steeper gradient in the age-velocity dispersion than the MW and M33 (Dorman et al. 2015; Bhattacharya et al. 2019). The median velocity dispersion values are significantly lower in M33, which is expected, as M33 is a less massive and therefore more fragile disk. The velocity dispersion of the LMC is most similar to that of M33, but for older stars, the LMC has a higher velocity dispersion than old stars in M33 do, which is unexpected just based on galaxy mass. However, the LMC is more obviously disturbed than the disk of M33, which could be the cause of the higer velocity dispersion.

The velocity dispersion reported in this work is not consistent with that measured using star clusters in M33 (Beasley et al. 2015). The star clusters show a higher

Age Group	AD w.r.t H I in M33 (kms^{-1})	AD in M33 inc. halo (kms^{-1})	AD w.r.t H I in M31 (kms^{-1})
Young	$15.1^{+1.6}_{-1.8}$	$15.1^{+1.6}_{-1.8}$	$-8.2^{+0.74}_{-0.72}$
Intermediate Age	$8.0^{+1.7}_{-1.6}$	$20.6^{+1.9}_{-1.8}$	$34.1^{+4.4}_{-4.0}$
Old	$24.5^{+0.9}_{-1.1}$	$42.0^{+1.1}_{-1.2}$	$63.0^{+0.59}_{-0.4}$

Table 5.4: Median values of AD for stars in M33 (this work) and in M31 (Quirk et al. 2019).

magnitude that is consistent with the MW Solar Neighborhood and a gradient in velocity dispersion and stellar age. One potential explanation for the difference is that we remove stars with line-of-sight velocities that are consistent with a dynamically hot component. If we do not remove these stars, we do recover a sloped age velocity dispersion relation and higher magnitudes, although not high enough to match the dispersion of the star clusters. It is possible that a larger fraction of the star clusters than individual stars belong to the hot component.

It is unexpected that this work does not see a trend between velocity dispersion and age, as it is predicted and seen in the MW and M31 (Leaman et al. 2017; Beasley et al. 2015; Nordström, B. et al. 2004; Dorman et al. 2015). This lack of trend is what Leaman et al. (2017) calculate for dwarf spheroids in the LG with masses ~ 1000 times less than M33, not for a more massive galaxy like M33. Their models, which do not distinguish between galactic components, predict M33 should have a velocity dispersion of $\sim$ 40 $\mathrm{km\,s^{-1}}$for stars with ages of several Gyr, which is also consistent with the observations of M33 star clusters (Beasley et al. 2015). If we do not remove likely halo stars, the oldest M33 stars in this work have a velocity dispersion that approaches 40 $\mathrm{km\,s^{-1}}$. This demonstrates the effect that contaminate halo stars can have in a measured age-velocity dispersion relation. The velocity dispersion of the individual stars and the

clusters were also measured in two different ways in two different samples, which results in different systematic uncertainties in the intrinsic dispersion calculation and could contribute to the discrepancy.

The existence of a substantial kinematically hot halo component in M33's inner disk (Gilbert et al. 2022) may suggest internal heating mechanisms, like gas flows from stellar feedback (El-Badry et al. 2016), could have caused enough disk heating to substantially contribute to a stellar halo, which could also cause stellar clusters and individual stars that were born in the disk to be heated or kicked up into the halo component.

Additionally, because of their respective inclinations, the observed line-of-sight velocity dispersion of M33 includes a larger z component than the observed line-of-sight velocity dispersion of M31. Martig et al. (2014) find that in more massive disks, the vertical component of velocity dispersion is largely dependent on merger history but these trends can be obscured when there are large uncertainties on age estimates. It is possible our wide age bins combined with the large influence of the vertical component in M33's line-of-sight velocity dispersion are obscuring a subtle trend in the age-velocity dispersion relation, but it is unlikely to fully explain the low magnitude of velocity dispersion for the intermediate age and old stars.

We also make the first comparisons of the AD as a function of stellar age observed in M31 and M33. There are no current measurements of AD as a function of stellar age in the MW or other galaxies in the LG. Table 5.4 compares the AD (with respect to H I) in M31 and M33. Like velocity dispersion, M31 has greater values of AD

and a steeper rise in AD as a function of age than observed in M33, suggesting that it has experienced several significant and ongoing heating events throughout its relatively recent history. If possible halo stars are not removed from the M33 dataset, there is a trend between velocity dispersion/AD and stellar age. However, this trend disappears if the likely halo stars are removed. Furthermore, the AD values roughly double when possible halo stars are not removed for the intermediate age and old stars.

There are other measurements of AD from Integral-field-units (IFUs): Martinsson et al. (2013) use IFUs to measure the AD with respect to ionized gas in face-on spiral galaxies and find stars lag behind the ionized gas by $\sim 11 \pm 8\%$, which is consistent with the young stars lagging on average by 20%, the intermediate age stars by 9%, and the old stars by 18%. This amount of lag is similar to studies of AD in other inclined local galaxies (Ciardullo et al. 2004; Herrmann & Ciardullo 2009; Westfall et al. 2007, 2011) and in the MW (Ratnatunga & Upgren 1997; Olling & Dehnen 2003).

5.7 Summary and Conclusions

In this work, we present the largest stellar spectroscopic survey of M33, the TREX Survey, and present initial analysis of the stellar disk kinematics as a function of stellar age using only individually resolved stars, which is the first of its kind in M33. Below we summarize our main findings and conclusions of the complex, yet low mass, galaxy.

- 1. The TREX survey consists of $\sim$ 4500 stars with good quality spectra across the entire disk of M33, ranging from several evolutionary stages: massive MS and

HeB stars, intermediate mass AGB stars, and low mass RGB stars. This work uses a subset (2561 spectra) of the full survey.

- 2. We find that M33's stellar disk has an average velocity dispersion of $\sim$ 16 $\mathrm{km\,s^{-1}}$, which is significantly lower than what is observed in the disk of MW and M31 (Holmberg, J. et al. 2009; Dorman et al. 2015) and lower than what is measured using star clusters (Beasley et al. 2015). The average magnitude of AD is on the order of $\sim$ 16, which is also lower than what is observed in M31.

- 3. Velocity dispersion and AD do not increase with stellar age in the disk, which is unexpected. We highlight the importance of removing potential halo stars when measuring the age-velocity dispersion and age-AD relation.

- 4. This analysis suggests that M33 has experienced a significantly different dynamical heating history than M31 and the MW, which may have been dominated by internal heating mechanisms rather than external ones.

- 5. The young stars are as dynamically hot as the older stars in the stellar disk component. These young stars also have a wider distribution of AD values than the old disk stars. They are more dynamically hot than simulated M33-like analogs predict. Possible mechanisms for the heating of the young stars could include turbulence from ongoing star formation or scattering from giant molecular clouds. It is also possible that these stars are remnants of a relatively recent minor merger or other type of galaxy interaction and lie in front of the disk.

5.8 Appendix

5.8.1 Special stars: weak CN and carbon Stars

As mentioned in Section 5.3 we identified two classes of rare M33 stars with unusual spectroscopic features, carbon stars and "weak CN" stars in our TREX survey dataset, using the same combination of visual inspection and machine classification of spectra that our team has used to identify such stars in M31 (Hamren et al. 2015, 2016; Guhathakurta et al. 2017; Kamath et al. 2017; Masegian et al. 2019; Kotha et al. 2020; Girardi et al. 2020; Chauhan et al. 2021; Rodriguez et al. 2021). The carbon stars are identified by their strong CN, CH, and C_2 molecular absorption bands, the strongest of which is the "W"-shaped CN band at 8000 Å. By contrast, the "weak CN" spectrum displays a much weaker 8000 Å CN absorption feature while the rest of the spectrum resembles that of a normal (i.e., O-rich) star of comparable color in that it displays the near-infrared Ca triplet and, for redder stars, a set of TiO bands.

We have compared the positions of these rare M33 stars in CMDs to theoretical stellar tracks from the PARSEC library (Bressan et al. 1993, 2012), for a variety of combinations of the PHATTER filters (all except F275W). As expected, this comparison indicates that carbon stars are intermediate mass/intermediate age AGB stars with masses of $M \sim 2$–$4\ M_{\odot}$ and ages of a few Gyr. In contrast, the "weak CN" stars are massive ($M \sim 4$–$M_{\odot}$) and short lived ($t < 100$ Myr) in the RGB/AGB evolutionary phase.

We identify 97 carbon stars and 363 weak CN stars that pass our quality and disk star cuts. For the bulk of this analysis, we have assigned the weak CN stars to the

young star group and the carbon stars to the intermediate age group. In this section, we examine the kinematics of these carbon and "weak CN" stars separately to see if they are unique beyond their spectral features.

Figure 5.16 shows the location and line-of-sight velocity of the weak CN and carbon stars. As there is a lack of young stars in the outer disk in our sample due to different target selection epochs, the weak CN stars are centrally concentrated while the carbon stars are present at extended radii. We have calculated the velocity dispersion for these two groups (Table 5.5). The weak CN stars have a lower velocity dispersion ($11.9\,\mathrm{km\,s^{-1}}$) than the young stars, intermediate stars, and old stars ($15.9\ \mathrm{km\,s^{-1}}$, $15.2\,\mathrm{km\,s^{-1}}$, and $16.5\,\mathrm{km\,s^{-1}}$, respectively; Table 5.1), and the carbon stars have a slightly higher velocity dispersion ($20.3\,\mathrm{km\,s^{-1}}$) than all the three age groups.

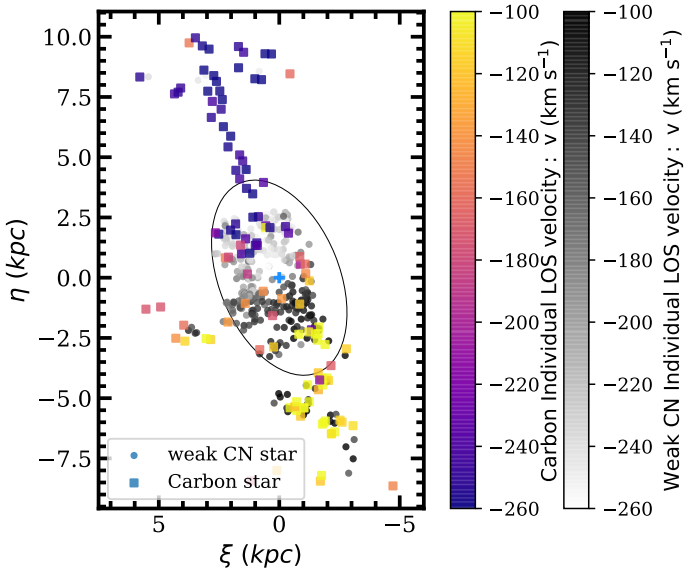

Figure 5.16: A spatial map showing the location of identified weak CN and carbon stars. The color represents the line-of-sight velocity. The weak CN stars have circular symbols and a grayscale colorbar, and the carbon stars have square symbols and a color colorbar.

Rare Star	σ_{LOS} (kms^{-1})	AD w.r.t H I (kms^{-1})	Width (kms^{-1})	Outliers (%)
weak CN	$11.9^{+0.4}_{-0.3}$	$8.0^{+2.2}_{-2.6}$	70.0	3.5
carbon	$20.3^{+1.2}_{-1.5}$	$22.4^{+23.5}_{-3.3}$	58.8	0.0

Table 5.5: Median values of velocity dispersion and AD for the weak CN and carbon stars with respect to H I. Also shown is the width (sigma) of the AD distributions and the percentage of outliers in the distributions. The errors on the median value represent the difference between the $16^{\text{th}}$and 84^{th} percentiles divided by $\sqrt{\text{N}}$, where N is the number of stars.

We also construct rotation curves and calculate AD for the weak CN and carbon stars. Because most of the carbon stars are located at large radii, we only calculate AD with respect to the H I. The median AD values, width of the distributions, and percentage of outliers in the distribution are shown in Table 5.5. The AD of the weak CN stars ($8.0\,\mathrm{km\,s^{-1}}$) most closely resembles that of the intermediate age stars ($8.0\,\mathrm{km\,s^{-1}}$). The carbon stars' median AD value ($22.4\,\mathrm{km\,s^{-1}}$) is more consistent with the old ($24.5\,\mathrm{km\,s^{-1}}$) than the intermediate age stars, even though they are believed to be intermediate age. The width of the distribution of AD for the weak CN and carbon stars are both closest to the width of the intermediate age stars ($67.7\,\mathrm{km\,s^{-1}}$), which is wider than the old stars. There does not appear to be anything kinematically unique about these rare spectral types.

Chapter 6

Summary and Future Directions

6.1 Summary

This thesis examines the stellar disk kinematics in M33 and M31. Chapter 3 analyzes asymmetric drift as a function of stellar age for stars in the northern disk of M31, using comparisons of the movements of individual stars and clouds of neutral and molecular gas. I find that the older stars are more offset from the gas than the younger and intermediate stars, showing that in M31, asymmetric drift increases monotonically with stellar age. This suggests that M31 has had violent and relatively constant dynamical heating events, like mergers. In Chapter 4, I compare these observed asymmetric drift measurements to simulated M31-like analogs in the large scale cosmological simulation IllustrisTNG. The observed measurements are most consistent with analogs that have had a major (4:1) merger within the past 4 Gyrs. This is another piece of evidence for the more recent major merger scenario for M31.

Chapter 5 presents the TREX Survey, which is the largest collection of stellar

spectroscopy in M33. It highlights some initial findings of the stellar disk kinematics; namely, the lack of kinematic age gradients. The young stars are as dynamically hot as the old stars, and thus velocity dispersion and asymmetric drift do not increase with stellar age. The velocity dispersion for M33 is also lower than that predicted by models of the interstellar medium and by observations of star clusters. We highlight the importance of removing stars that are likely to belong to a dynamically hot component, i.e., a stellar halo, when analyzing the kinematics of the disk.

I hope this thesis demonstrates the power of using resolved stellar spectroscopy to get local measurements of stellar disk kinematics and the importance of studying local galaxies in detail so that we can better understand the uniqueness of our own galaxy and galactic neighborhood while also helping inform us about higher redshift galaxies.

6.2 Future directions

6.2.1 M33 Outer Disk

There is still much to be explored in M33. The data presented in Chapter 5 does not represent the entirety of the TREX Survey. There are targets for which we have measured velocities but have not yet paired them to photometry, as they were serendipitous observations. It would increase our sample by 27%.

Additionally, we observed 17 masks in the fall of 2021, the layout of which can be seen in Figure 6.1. During these observations, we targeted older stars in the inner disk (to fill in the *belly of the beast*) and a variety of types of stars in the far outer disk. The outer masks were placed so as to overlap with the dramatic warps in the

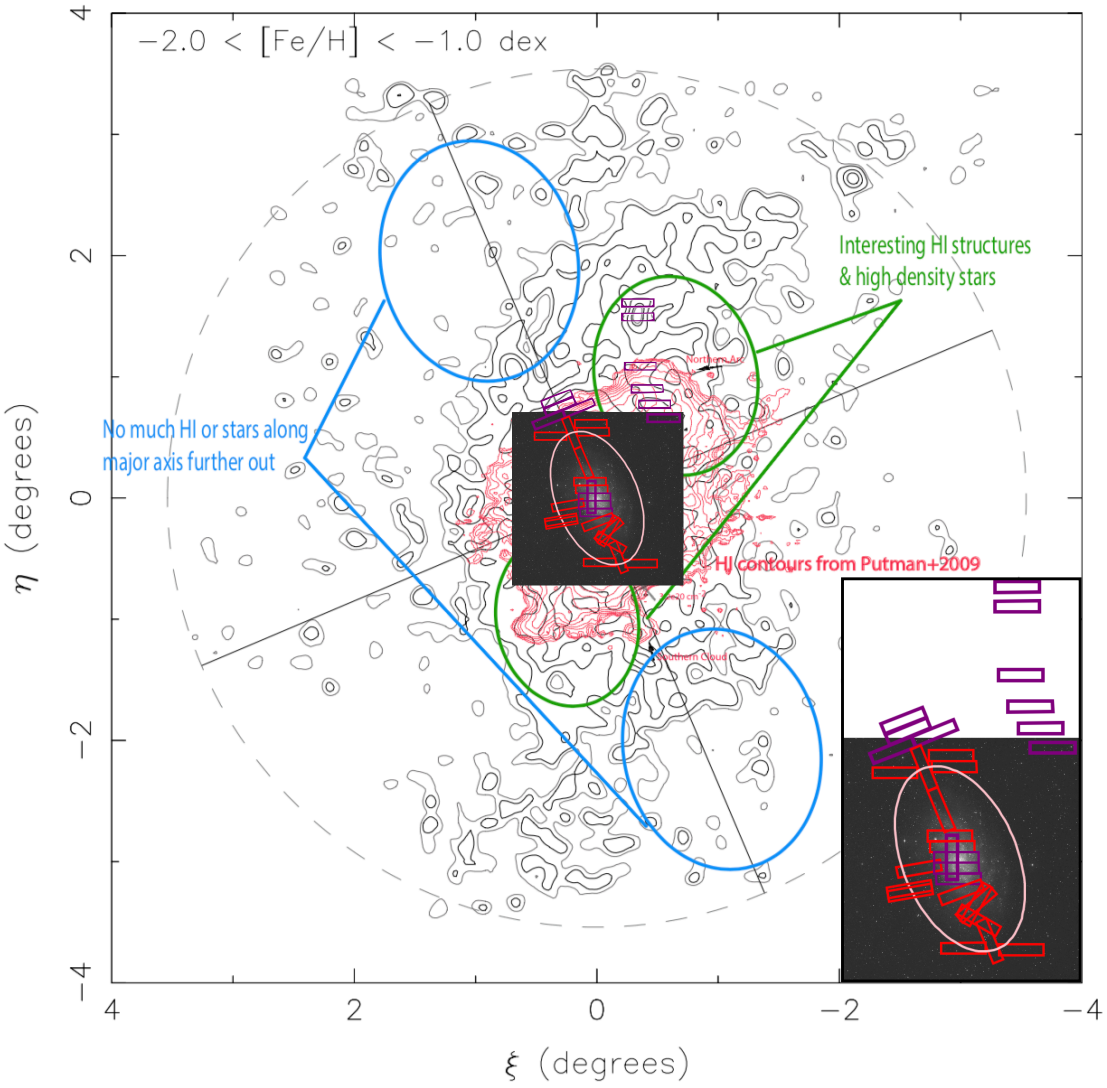

Figure 6.1: Image of the published (red) and unpublished 2021 (purple) TREX DEIMOS masks. An enlargement of the masks and inner portion is shown in the lower right corner. The image of M33 comes from DSS. The black contours and background figure come from McConnachie et al. (2009) who mapped the stellar warp using RGB stars. The red contours show the neutral gas warps from Putman et al. (2009). This figure was put together in part by Yong Zheng.

extended stellar and gas disks in M33. Getting stellar velocities in these regions will help determine the origin of the warps. This could shed light not only on the cause of the warps but also on what triggered a burst of star formation in M31 and M33 2-4 Gyrs ago (Lewis et al. 2015), which would help us understand the evolution of the M31/M33 system. We also aim to further examine the dynamically hot component described in Gilbert et al. (2022). This possible stellar halo component shows asymmetries in the outer vs inner disk and north vs south parts of the disk. We will be able to further constrain this discovery and the properties of the stellar halo with the 2021 masks. Constraining the halo further will help confirm its formation (in-situ vs accreted) and evolution. It might be that this "halo" more resembles a kicked-up disk population, and the data might allow us to more definitely differentiate between the kinematical proprieties of a heated disk vs halo, which is not trivial.

Additionally, there is evidence that AGB (intermediate age) stars exist in the dynamically hot component. We specifically targeted AGB stars in 2021 to increase our sample size and spatial expanse in order to determine if this evidence is substantial. If there is a significant fraction of intermediate stars in the halo, it is more likely that the halo is either a kicked-up disk or a halo that formed from a heated disk and not from an accretion event. Lastly, one of the 2021 masks targeted stars across the inner disks that had already been observed. This duplicate data will allow us to better characterize the velocity measurement errors for young stars, as this is currently not as well constrained as it is for older stars in the survey.

Another natural next project for the TREX Survey collaboration is to do a

detailed analysis of M33-like analogs in simulations. Particularly, it would be interesting to look at the stellar assembly histories for analogs that have kinematics similar to those observed in M33. As M33 is a low mass disk, the simulated analogs can also be used to study which internal heating phenomenon likely lead to the present day dynamics in the galaxy. This would provide insight into how low mass disks evolve, which is particularly important for understanding high redshift disk galaxies.

6.2.2 M31

Although the stellar populations in M31 have been studied in more detail than those in M33 have, there is still much left to discover in M31, particularly in its southern disk. Ben Williams successfully proposed a similar survey to PHAT (Williams et al. 2014) that would target the southern half of M31 with 4 filter (optical and near UV) photometry using the Hubble Space Telescope. This survey, The Panchromatic Hubble Andromeda Southern Treasury (PHAST), was the largest accepted proposal in Cycle 29. As a collaborator, I have access to the incoming astrometric and photometric catalogs and will help plan and conduct spectroscopic followup observations (Figure 6.2).

With stellar spectroscopy in the southern disk we can make local measurements of stellar kinematics as a function of age, compare the kinematics of the northern and southern disk, and have more data to model the galactic components of M31. Work done by me and Ekta Patel for the PHAST proposal shows that if one half of M31's disk contains the progenitor of the Giant Stellar Stream (GSS), there should be noticeable differences in the star formation histories and age-velocity dispersion gradients of the two halves. We will be able to do that comparison and determine which half of the

disk contains the merger remnant, which will allow for detailed followup and greater understanding of M31's merger history. Although the HST observations are still ongoing, there is enough data to have put in a Keck proposal for fall 2022 to target stars around the M32 region. In the 2023B cycle, we will ask for more time to cover the rest of the PHAST footprint and to observe young blue stars throughout the southern half.

Additionally, there are more opportunities to compare the kinematics of stars with the surrounding gas in both halves of the disk. Hα measurements can be picked up in the stellar spectroscopic slits. These measurements provide a direct comparison of the stellar kinematics and the kinematics of the Hα, allowing for a new set of AD calculations. The rotation velocities of the CO, Hα, and H I can all be compared to each other as well. This work is also possible in M33. Similarly, adding in the kinematics of H II regions and planetary nebulae (like those in Bhattacharya et al. 2019) would make for an interesting comparison to the measurements presented in this thesis. One could also compare the kinematics of the different kinds of gas.

6.2.3 M32 – Filling in the Messier Sequence

As mentioned in the previous section, we are going to target stars around M32 for stellar spectroscopy in the fall of 2022 (fingers crossed for a yes from the Keck TAC). Having more radial velocities of stars in the region of M32 will allow us to help determine a star's membership to M31, M32, or the GSS. These distinctions in turn allow us to better determine if M32 is the progenitor of the GSS, especially when paired with metallicities. Observations to get metallicities of stars in M32 is possible with deep exposures and high quality photometry, like the PHAST survey. The 2022B Keck

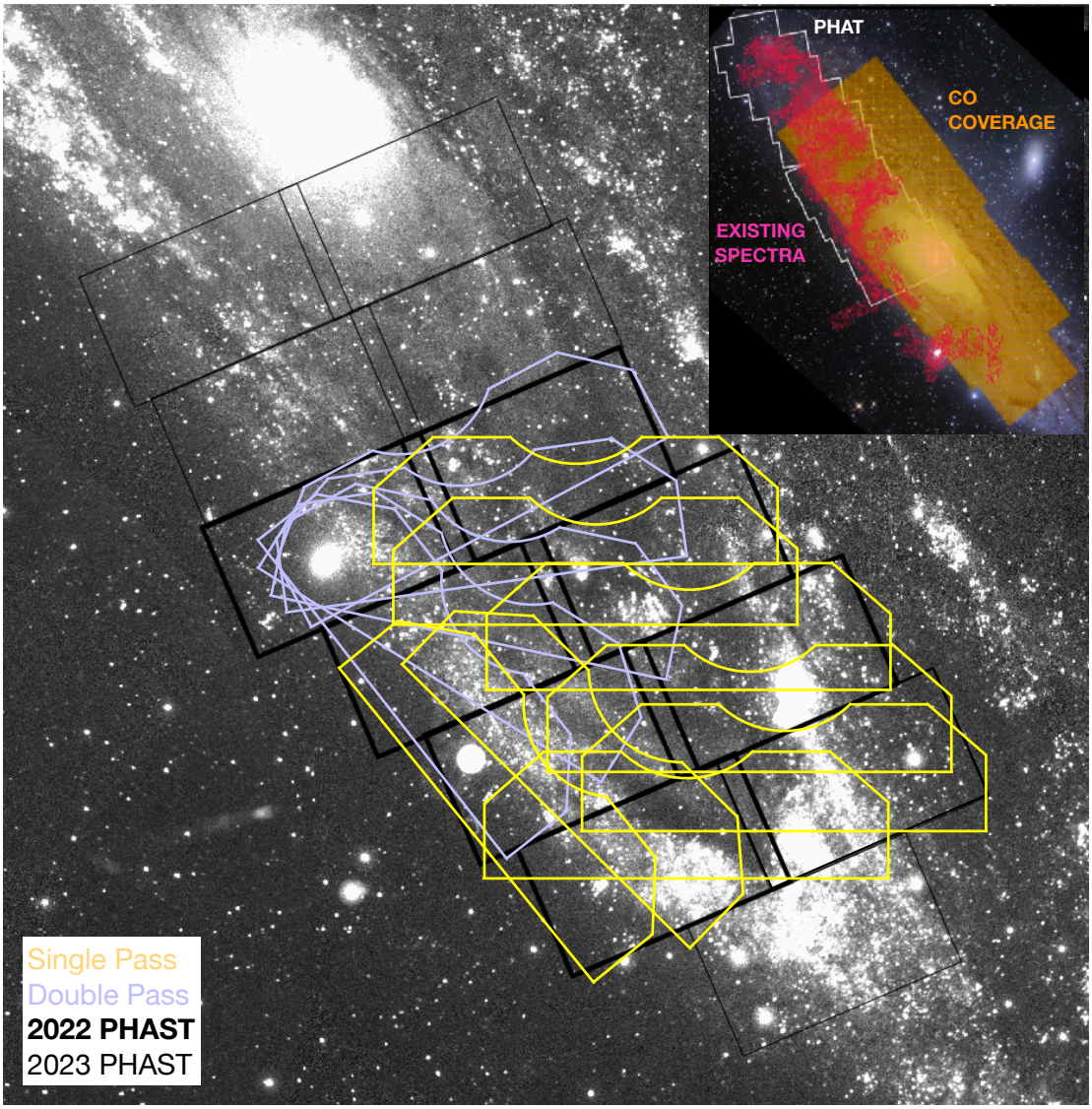

Figure 6.2: Image of the proposed observations of M31's southern half using the PHAST photometry. The purple DEIMOS shapes represent placements where we would put two masks with different targets, and the yellow shapes represent a single placement. The beautiful DEIMOS shape in this figure was created by Raja GuhaThakurta, who also designed this configuration. The bold black rectangles represent the PHAST bricks that will be observed by June 2022, and the unbolded black rectangles are the PHAST bricks that will be observed by June 2023. The inset in the upper right shows the PHAT footprint and the existing spectroscopy in the northern half.

proposal mentioned above will result in the metallicities of M32 stars in the pivot point of the fan. The combination of radial velocities and metallicities will lead to a powerful study of the origins of the GSS.

6.2.4 MW

Lastly, it would be amazing to have radial velocities for a variety of types of stars across the entire disk of the MW. This is becoming more possible with Gaia, especially with the upcoming full DR3 (sometime in the first half of 2022, Antoja et al. 2018), which will have more radial velocities. The MW galaxy shows evidence for having had fewer mergers than M31 (e.g., Leaman et al. 2017; Helmi et al. 2018). Gaia DR3 will allow a more global view of the MW disk and halo, which could reveal more signs of mergers than has previously been discovered. It would be interesting to see how steep of a gradient in the age velocity dispersion relation there is beyond what we see in the Solar Neighborhood (Nordström, B. et al. 2004; Holmberg, J. et al. 2009). This would allow for a more direct comparison to the stellar disk kinematics of M33 and M31. It would be especially useful to be able to compare this gradient for the thin and thick disk of the MW with halo stars removed from each sample.

Bibliography

Abadi, M. G., Navarro, J. F., Steinmetz, M., & Eke, V. R. 2003, The Astrophysical Journal, 597, 21

Amôres, E. B., Robin, A. C., & Reylé, C. 2017, A&A, 602, A67

Antoja, T., Helmi, A., Romero-Gómez, M., et al. 2018, Nature, 561, 360

Barker, M. K., Ferguson, A. M. N., Cole, A. A., et al. 2011, MNRAS, 410, 504

Beasley, M. A., San Roman, I., Gallart, C., Sarajedini, A., & Aparicio, A. 2015, Monthly Notices of the Royal Astronomical Society, 451, 3400

Bell, E. F., Monachesi, A., Harmsen, B., et al. 2017, GALAXIES GROW THEIR BULGES AND BLACK HOLES IN DIVERSE WAYS, arXiv:arXiv:1702.06116v1

Belokurov, V., Zucker, D. B., Evans, N. W., et al. 2006, ApJ, 642, L137

Bershady, M. A., Andersen, D. R., Verheijen, M. A. W., et al. 2004, The Astrophysical Journal Supplement Series, 156, 311

—. 2005, The Astrophysical Journal Supplement Series, 156, 311

Bershady, M. A., Verheijen, M. A., Swaters, R. A., et al. 2010, Astrophysical Journal, 716, 198

Bhattacharya, S., Arnaboldi, M., Caldwell, N., et al. 2019, Astronomy Astrophysics,

631, A56

Binney, J., & Tremaine, S. 2008, Galactic dynamics (Princeton University Press),

Bird, J. C., Kazantzidis, S., Weinberg, D. H., et al. 2013, The Astrophysical Journal, 773, 43

Bird, J. C., Loebman, S. R., Weinberg, D. H., et al. 2021, Monthly Notices of the Royal Astronomical Society, 503, 1815

Blitz, L., & Rosolowsky, E. 2006, The Astrophysical Journal, 650, 933

Bottema, R. 1993, Astronomy & Astrophysics, 275, 16

Bournaud, F., Elmegreen, B. G., & Martig, M. 2009, ApJ, 707, L1

Bovy, J., Hogg, D. W., & Rix, H.-W. 2009, The Astrophysical Journal, 704, 1704

Bovy, J., Prieto, C. A., Beers, T. C., et al. 2012, The Astrophysical Journal, 759, 131

Braun, R., & Thilker, D. A. 2004, A&A, 417, 421

Bressan, A., Bertelli, G., & Chiosi, C. 1993, in New Aspects of Magellanic Cloud Research, ed. B. Baschek, G. Klare, & J. Lequeux (Berlin, Heidelberg: Springer Berlin Heidelberg), 352–361

Bressan, A., Marigo, P., Girardi, L., et al. 2012, Monthly Notices of the Royal Astronomical Society, 427, 127

Brook, C. B., Kawata, D., Gibson, B. K., & Freeman, K. C. 2004, The Astrophysical Journal, 612, 894

Bryan, G. L., & Norman, M. L. 1998, The Astrophysical Journal, 495, 80

Budanova, N. O., Korchagin, V. I., & Gozha, M. L. 2017, Astronomy Reports, 61, 915

Bundy, K., Bershady, M. A., Law, D. R., et al. 2015, Overview of the SDSS-IV MaNGA

survey: Mapping Nearby Galaxies at Apache Point Observatory, arXiv:1412.1482

Carignan, C., Charbonneau, P., Boulanger, F., & Viallefond, F. 1990, Astronomy & Astrophysics, 234, 43

Chauhan, S. S., Rodriguez, C., Rose, T., et al. 2021, in American Astronomical Society meeting 237, id. 548.16, Vol. 53

Chemin, L., Braine, J., Combes, F., Kam, Z. S., & Carignan, C. 2020, A&A, 639, A145

Chemin, L., Carignan, C., & Foster, T. 2009, The Astrophysical Journal, 705, 1395

Chiba, M., & Beers, T. C. 2000, The Astronomical Journal, 119, 2843

Ciardullo, R., Durrell, P. R., Laychak, M. B., et al. 2004, The Astrophysical Journal, 614, 167

Cole, A. A., Tolstoy, E., III, J. S. G., & Smecker-Hane, T. A. 2005, The Astronomical Journal, 129, 1465

Collins, M. L. M., Chapman, S. C., Ibata, R. A., et al. 2011, Monthly Notices of the Royal Astronomical Society, 413, 1548

Cooper, M. C., Newman, J. A., Davis, M., Finkbeiner, D. P., & Gerke, B. F. 2012, Astrophysics Source Code Library, 3003

Corbelli, E., Lorenzoni, S., Walterbos, R., Braun, R., & Thilker, D. 2010, Astronomy Astrophysics, 511, A89

Corbelli, E., Thilker, D., Zibetti, S., Giovanardi, C., & Salucci, P. 2014, A&A, 572, A23

Courteau, S., Widrow, L. M., McDonald, M., et al. 2011, The Astrophysical Journal, 739, 20

Cunningham, E. C., Deason, A. J., Rockosi, C. M., et al. 2019a, The Astrophysical

Journal, 876, 124

Cunningham, E. C., Deason, A. J., Sanderson, R. E., et al. 2019b, The Astrophysical Journal, 879, 120

Dalcanton, J. J., & Stilp, A. M. 2010, The Astrophysical Journal, 721, 547

Dalcanton, J. J., Williams, B. F., Lang, D., et al. 2012, Astrophysical Journal, Supplement Series, 200, arXiv:1204.0010

Dalcanton, J. J., Fouesneau, M., Hogg, D. W., et al. 2015, Astrophysical Journal, 814

Daniel, K. J., Schaffner, D. A., McCluskey, F., Kawaguchi, C. F., & Loebman, S. 2019, The Astrophysical Journal, 882, 111

Daniel, K. J., & Wyse, R. F. G. 2015, Monthly Notices of the Royal Astronomical Society, 447, 3576

Dashyan, G., Choi, E., Somerville, R. S., et al. 2019, Monthly Notices of the Royal Astronomical Society, 487, 5889

de Grijs, R., & Bono, G. 2014, AJ, 148, 17

Dehnen, W. 1998, The Astronomical Journal, 115, 2384

Dehnen, W., & Binney, J. J. 1998, Monthly Notices of the Royal Astronomical Society, 298, 387

Dolag, K., Borgani, S., Murante, G., & Springel, V. 2009, Monthly Notices of the Royal Astronomical Society, 399, 497

Dorman, C. E. 2015, PhD thesis, University of California Santa Cruz

Dorman, C. E., Guhathakurta, P., Fardal, M. A., et al. 2012, Astrophysical Journal, 752

Dorman, C. E., Widrow, L. M., Guhathakurta, P., et al. 2013, The Astrophysical Journal, 779, 103

Dorman, C. E., Guhathakurta, P., Seth, A. C., et al. 2015, The Astrophysical Journal, 803, 24

Driver, S. P., Allen, P. D., Liske, J., & Graham, A. W. 2007, ApJ, 657, L85

Druard, C., Braine, J., Schuster, K. F., et al. 2014, A&A, 567, A118

D'Souza, R., & Bell, E. F. 2018, Nature Astronomy, 1

Du, C., Li, H., Liu, S., Donlon, T., & Newberg, H. J. 2018, 863, 87

El-Badry, K., Wetzel, A., Geha, M., et al. 2016, The Astrophysical Journal, 820, 131

El-Badry, K., Wetzel, A., Geha, M., et al. 2016, ApJ, 820, 131

Escala, I., Kirby, E. N., Gilbert, K. M., Cunningham, E. C., & Wojno, J. 2019, The Astrophysical Journal, 878, 42

Faber, S. M., Phillips, A. C., Kibrick, R. I., et al. 2003, in Presented at the Society of Photo-Optical Instrumentation Engineers (SPIE) Conference, Vol. 4841, Instrument Design and Performance for Optical/Infrared Ground-based Telescopes. Edited by Iye, Masanori; Moorwood, Alan F. M. Proceedings of the SPIE, Volume 4841, pp. 1657-1669 (2003)., ed. M. Iye & A. F. M. Moorwood, 1657–1669

Fardal, M. A., Babul, A., Guhathakurta, P., Gilbert, K. M., & Dodge, C. 2008, The Astrophysical Journal, 682, L33

Fardal, M. A., Guhathakurta, P., Babul, A., & McConnachie, A. W. 2007, Monthly Notices of the Royal Astronomical Society, 380, 15

Ferguson, A., Irwin, M., Chapman, S., et al. 2007, Astrophysics and Space Science

Proceedings, 3, 239

Ferguson, A. M. N., Irwin, M. J., Ibata, R. A., et al. 2002, The Astronomical Journal, 124, 1452

Ferguson, A. M. N., & Mackey, A. D. 2016, in Tidal Streams in the Local Group and Beyond, ed. H. Newberg & J. Carlin (Springer Link), 191

Fuhrmann, K. 2004, Astronomische Nachrichten, 325, 3

Gabor, J. M., Davé, R., Finlator, K., & Oppenheimer, B. D. 2010, Monthly Notices of the Royal Astronomical Society, 407, 749

Gaia Collaboration, Antoja, T., McMillan, P. J., et al. 2021, A&A, 649, A8

Gardan, E., Braine, J., Schuster, K. F., Brouillet, N., & Sievers, A. 2007, A&A, 473, 91

Gilbert, K. M., Guhathakurta, P., Kalirai, J. S., et al. 2006, The Astrophysical Journal, 652, 1188

Gilbert, K. M., Quirk, A. C. N., Guhathakurta, P., et al. 2022, The Astrophysical Journal, 924, 116

Girardi, L., Boyer, M. L., Johnson, L. C., et al. 2020, The Astrophysical Journal, 901, 19

Golubov, O. 2014, Odessa Astronomical, 27

Gratier, P., Braine, J., Rodriguez-Fernandez, N. J., et al. 2010, A&A, 522, A3

Guhathakurta, P., Kamath, A., Sales, A., Sarukkai, A., & Hays, J. 2017, in American Astronomical Society, AAS Meeting 229, id.232.06

Guhathakurta, P., Ostheimer, J. C., Gilbert, K. M., et al. 2005, astro-ph/0502366 preprint, 48

Guhathakurta, P., Rich, R. M., Reitzel, D. B., et al. 2006, The Astronomical Journal, 131, 2497

Guo, Q., White, S., Li, C., & Boylan-Kolchin, M. 2010, Monthly Notices of the Royal Astronomical Society, 404, 1111

Guo, Y., Rafelski, M., Faber, S. M., et al. 2016, The Astrophysical Journal, 833, 37

Gwyn, S. D. J. 2008, PASP, 120, 212

Hammer, F., Yang, Y. B., Wang, J. L., et al. 2018, MNRAS, 000, 1

Hamren, K., Beaton, R. L., Guhathakurta, P., et al. 2016, The Astrophysical Journal, 828, 15

Hamren, K. M., Rockosi, C. M., Guhathakurta, P., et al. 2015, The Astrophysical Journal, 810, 60

Helmi, A., Babusiaux, C., Koppelman, H. H., et al. 2018, Nature, 563, 85

Helmi, A., Sales, L. V., Starkenburg, E., et al. 2012, ApJ, 758, L5

Hernquist, L., & Quinn, P. J. 1988, ApJ, 342

—. 1989, ApJ, 331

Herrmann, K. A., & Ciardullo, R. 2009, Astrophysical Journal, 705, 1686

Hinshaw, G., Larson, D., Komatsu, E., et al. 2013, The Astrophysical Journal Supplement, 208, 19

Hodge, P. W., Balsley, J., Wyder, T. K., & Skelton, B. P. 1999, 111, 685

Holmberg, J., Nordström, B., & Andersen, J. 2009, A&A, 501, 941

Huang, Y., Liu, X.-W., Yuan, H.-B., et al. 2016, Monthly Notices of the Royal Astronomical Society, 463, 2623

Ibata, R., Chapman, S., Ferguson, A. M. N., et al. 2005, Astrophysical Journal, 634, 287

Ibata, R., Irwin, M., Lewis, G., Ferguson, A. M., & Tanvir, N. 2001, Nature, 412, 49

Ibata, R., Martin, N. F., Irwin, M., et al. 2007, The Astrophysical Journal, 671, 1591

Ibata, R. A., Lewis, G. F., McConnachie, A. W., et al. 2013, The Astrophysical Journal, 780, 128

Ida, S., Kokubo, E., & Makino, J. 1993, MNRAS, 263, 875

Jenkins, A., & Binney, J. 1990, Monthly Notices of the Royal Astronomical Society, 245, 13

Kado-Fong, E., Greene, J. E., Huang, S., et al. 2020, The Astrophysical Journal, 900, 163

Kado-Fong, E., Sanderson, R. E., Greene, J. E., et al. 2021, Arxiv e-prints

Kam, S. Z., Carignan, C., Chemin, L., et al. 2017, AJ, 154, 41

Kam, Z. S., Carignan, C., Chemin, L., Amram, P., & Epinat, B. 2015, Monthly Notices of the Royal Astronomical Society, 449, 4048

Kamath, A., Sales, A., Sarukkai, A., et al. 2017, in American Astronomical Society, AAS Meeting 229, id.154.03

Koch, E. W., Rosolowsky, E. W., Lockman, F. J., et al. 2018, Monthly Notices of the Royal Astronomical Society, 479, 2505

Kotha, S., Guhathakurta, P., Raikar, R., & Bhattacharya, A. 2020, in American Astronomical Society meeting 235, id. 110.10

Kregel, M., & van der Kruit, P. C. 2005, Monthly Notices of the Royal Astronomical

Society, 358, 481

Lazzarini, M., & et al. in preparation, To be submitted to AAS journals

Leaman, R., Mendel, J. T., Wisnioski, E., et al. 2017, Monthly Notices of the Royal Astronomical Society, 472, 1879

Lewis, A. R., Dolphin, A. E., Dalcanton, J. J., et al. 2015, ApJ, 805, 183

Lewis, G. F., Braun, R., McConnachie, A. W., et al. 2013, ApJ, 763, 4

Mackey, D., Lewis, G. F., Brewer, B. J., et al. 2019, Nature, 574, 69

Marigo, P., Girardi, L., Bressan, A., et al. 2017, ApJ, 835, 77

Marinacci, F., Vogelsberger, M., Pakmor, R., et al. 2018, Monthly Notices of the Royal Astronomical Society, 480, 5113

Martig, M., Bournaud, F., Teyssier, R., & Dekel, A. 2009, The Astrophysical Journal, 707, 250

Martig, M., Minchev, I., & Flynn, C. 2014, Monthly Notices of the Royal Astronomical Society, 443, 2452

Martinsson, T. P. K., Verheijen, M. A. W., Westfall, K. B., et al. 2013, Astronomy & Astrophysics, 557, A130

Masegian, A., Maheshwari, A., Guhathakurta, P., & Raikar, R. 2019, in American Astronomical Society, AAS Meeting 233, id.371.01

Maxwell, A. J., Wadsley, J., Couchman, H. M. P., & Mashchenko, S. 2012, ApJ, 755, L35

McConnachie, A. W., Ferguson, A. M. N., Irwin, M. J., et al. 2010, The Astrophysical Journal, 723, 1038

McConnachie, A. W., Irwin, M. J., Ferguson, A. M., et al. 2005, Monthly Notices of the Royal Astronomical Society, 356, 979

McConnachie, A. W., Irwin, M. J., Ibata, R. A., et al. 2009, Nature, 461, 66

McConnachie, A. W., Ibata, R., Martin, N., et al. 2018, The Astrophysical Journal, 868, 55

Mutch, S. J., Croton, D. J., & Poole, G. B. 2011, ApJ, 736, 84

Naiman, J. P., Pillepich, A., Springel, V., et al. 2018, Monthly Notices of the Royal Astronomical Society, 477, 1206

Nelson, D., Pillepich, A., Genel, S., et al. 2015, Astronomy and Computing, 13, 12

Nelson, D., Pillepich, A., Springel, V., et al. 2018, Monthly Notices of the Royal Astronomical Society, 475, 624

Newman, J. A., Cooper, M. C., Davis, M., et al. 2013, ApJS, 208, 5

Nieten, C., Neininger, N., Guélin, M., et al. 2006, Astronomy & Astrophysics, 453, 459

Nordström, B., Mayor, M., Andersen, J., et al. 2004, A&A, 418, 989

Olling, R. P., & Dehnen, W. 2003, The Astrophysical Journal, 599, 275

Oñorbe, J., Boylan-Kolchin, M., Bullock, J. S., et al. 2015, Monthly Notices of the Royal Astronomical Society, 454, 2092

Patel, E., Besla, G., & Mandel, K. 2017, Monthly Notices of the Royal Astronomical Society, 468, 3428

Patel, E., Besla, G., & Sohn, S. T. 2017, MNRAS, 464, 3825

Patel, E., Carlin, J. L., Tollerud, E. J., Collins, M. L. M., & Dooley, G. A. 2018, Monthly Notices of the Royal Astronomical Society, 480, 1883

Patra Nath, N. 2020, Monthly Notices of the Royal Astronomical Society, 499, 2063

Pillepich, A., Nelson, D., Hernquist, L., et al. 2018, Monthly Notices of the Royal Astronomical Society, 475, 648

Planck Collaboration, Ade, P. A. R., Aghanim, N., et al. 2016, Astronomy Astrophysics, 594, A13

Pontzen, A., Tremmel, M., Roth, N., et al. 2016, Monthly Notices of the Royal Astronomical Society, 465, 547

Purcell, C. W., Bullock, J. S., & Kazantzidis, S. 2010, Monthly Notices of the Royal Astronomical Society, 404, 1711

Putman, M. E., Peek, J. E. G., Muratov, A., et al. 2009, ApJ, 703, 1486

Quinn, P. J., & Goodman, J. 1986, The Astrophysical Journal, 309, 472

Quinn, P. J., Hernquist, L., & Fullagar, D. P. 1993, ApJ, 403, 74

Quirk, A., Guhathakurta, P., Chemin, L., et al. 2019, The Astrophysical Journal, 871, 11

Quirk, A. C. N., & Patel, E. 2020, Monthly Notices of the Royal Astronomical Society, 497, 2870

Quirk, A. C. N., Guhathakurta, P., Gilbert, K. M., et al. 2022, The Astronomical Journal, 163, 166

Ratnatunga, K. U., & Upgren, A. R. 1997, THE ASTROPHYSICAL JOURNAL, 476, 811

Robin, A. C., Bienaymé, O., Fernández-Trincado, J. G., & Reylé, C. 2017, A&A, 605, A1

Robin, A. C., Reylé, C., Derrière, S., & Picaud, S. 2003, Astron.Astrophys, 409

Robin, A. C., Reyle, C., Fliri, J., et al. 2014, A&A, 569

Rodriguez, C., Guhathakurta, P., Bhattacharya, A., et al. 2021, in

Rodriguez-Gomez, V. 2016, PhD thesis, Harvard University

Rodriguez-Gomez, V., Genel, S., Vogelsberger, M., et al. 2015, Monthly Notices of the Royal Astronomical Society, 449, 49

Rodriguez-Gomez, V., Pillepich, A., Sales, L. V., et al. 2016, Monthly Notices of the Royal Astronomical Society, 458, 2371

Rodriguez-Gomez, V., Snyder, G. F., Lotz, J. M., et al. 2019, Monthly Notices of the Royal Astronomical Society, 483, 4140

Roychowdhury, S., Chengalur, J. N., Karachentsev, I. D., & Kaisina, E. I. 2013, Monthly Notices of the Royal Astronomical Society: Letters, 436, L104

Sadoun, R., Mohayaee, R., & Colin, J. 2014, Monthly Notices of the Royal Astronomical Society, 442, 160

Saha, K., & Elmegreen, B. 2018, The Astrophysical Journal, 858, 24

Sellwood, J. A. 2014, Review of Modern Physics, 86, 1

Sellwood, J. A., & Binney, J. J. 2002, Monthly Notices of the Royal Astronomical Society, 336, 785

Sellwood, J. A., & Moore, E. M. 1998, The Astrophysical Journal, 510, 38

Semczuk, M., Łokas, E. L., Salomon, J.-B., Athanassoula, E., & D'Onghia, E. 2018, ApJ, 864, 34

Seth, A. C., Dalcanton, J. J., & de Jong, R. S. 2005, The Astronomical Journal, 130,

1574

Sick, J., Courteau, S., Cuillandre, J.-C., et al. 2014, The Astronomical Journal, 147, 109

Simon, J. D., & Geha, M. 2007, ApJ, 670, 313

Smercina, A., & et al. in preparation, To be submitted to AAS journals

Sohn, S. T., Majewski, S. R., Muñoz, R. R., et al. 2007, ApJ, 663, 960

Springel, V. 2010, Monthly Notices of the Royal Astronomical Society, 401, 791

Springel, V., White, S. D. M., Tormen, G., & Kauffmann, G. 2001, Monthly Notices of the Royal Astronomical Society, 328, 726

Springel, V., Pakmor, R., Pillepich, A., et al. 2018, Monthly Notices of the Royal Astronomical Society, 475, 676

Stinson, G. S., Dalcanton, J. J., Quinn, T., et al. 2009, MNRAS, 395, 1455

Strömberg, G. 1946, The Astrophysical Journal, 104, 12

Sysoliatina, K., Just, A., Golubov, O., et al. 2018, Astronomy Astrophysics, 614, A63

Tamm, A., Tempel, E., Tenjes, P., Tihhonova, O., & Tuvikene, T. 2012, Astronomy Astrophysics, 546, A4

Tanaka, M., Chiba, M., Komiyama, Y., et al. 2009, The Astrophysical Journal, 708, 1168

Terrazas, B. A., Bell, E. F., Pillepich, A., et al. 2020, Monthly Notices of the Royal Astronomical Society, 493, 1888

Ting, Y.-S., & Rix, H.-W. 2019, The Astrophysical Journal, 878, 21

Tissera, P. B., Scannapieco, C., Beers, T. C., & Carollo, D. 2013, MNRAS, 432, 3391

Torrey, P., Snyder, G. F., Vogelsberger, M., et al. 2015, Monthly Notices of the Royal Astronomical Society, 447, 2753

Toth, G., & Ostriker, J. P. 1992, ApJ, 389, 5

van der Kruit, P., & Freeman, K. 2011, Annual Review of Astronomy and Astrophysics, 49, 301

van der Marel, R. P., Fardal, M. A., Sohn, S. T., et al. 2019, The Astrophysical Journal, 872, 24

van der Marel, R. P., Fardal, M. A., Sohn, S. T., et al. 2018, ArXiv e-prints, arXiv:1805.04079

van der Wel, A., Chang, Y.-Y., Bell, E. F., et al. 2014, The Astrophysical Journal, 792, L6

Velazquez, H., & White, S. D. M. 1999, MNRAS, 304, 254

Vogelsberger, M., Genel, S., Springel, V., et al. 2014, Monthly Notices of the Royal Astronomical Society, 444, 1518

Walker, I. R., Mihos, J. C., & Hernquist, L. 1996, ApJ, 460, 121

Warner, P. J., Wright, M. C. H., & Baldwin, J. E. 1973, Monthly Notices of the Royal Astronomical Society, 163, 163

Weinberger, R., Springel, V., Pakmor, R., et al. 2018, Monthly Notices of the Royal Astronomical Society, 479, 4056

Weinberger, R., Springel, V., Pakmor, R., et al. 2018, Monthly Notices of the Royal Astronomical Society, 479, 4056

Westfall, K. B., Andersen, D. R., Bershady, M. A., et al. 2014, Astrophysical Journal,

785

Westfall, K. B., Bershady, M. A., Verheijen, M. A., et al. 2011, Astrophysical Journal, 742, arXiv:1108.2946

Westfall, K. B., Bershady, M. A., Verheijen, M. A., Andersen, D. R., & Swaters, R. A. 2007, in Astrophysics and Space Science Proceedings No. 202409, 157

Williams, B. F., Dalcanton, J. J., Dolphin, A. E., Holtzman, J., & Sarajedini, A. 2009, The Astrophysical Journal, 695, L15

Williams, B. F., Lang, D., Dalcanton, J. J., et al. 2014, Astrophysical Journal, Supplement Series, 215, 9

Williams, B. F., Dolphin, A. E., Dalcanton, J. J., et al. 2017, The Astrophysical Journal, 846, 145

—. 2018, eprint arXiv:1708.02617

Williams, B. F., Durbin, M. J., Dalcanton, J. J., et al. 2021, The Astrophysical Journal Supplement Series, 253, 53

Yoachim, P., & Dalcanton, J. J. 2008, The Astrophysical Journal, 682, 1004

Yu, S., Xu, D., Ho, L. C., Wang, J., & W., K. 2022, Astronomy and Astrophysics, arXiv:2202.06932